

# Molekulardynamische Untersuchungen heterogener Keimbildung

Inaugural - Dissertation

zur  
Erlangung des Doktorgrades  
der Mathematisch-Naturwissenschaftlichen Fakultät  
der Universität zu Köln

vorgelegt von

Roberto Rozas  
aus Chile

Köln  
2006

Berichterstatter: Priv.-Doz. Dr. Thomas Kraska  
Prof. Dr. Ulrich Deiters

Tag der letzten mündlichen Prüfung: 05.12.2006

*„Es wird sich zeigen, dass es gar schwierig ist,  
zu erkennen, welche Eigenschaften jedes Ding  
in Wirklichkeit hat“ Demokrit, 8 Jh. v. Chr.*





# Zusammenfassung

Heterogene Keimbildung, insbesondere die Kondensation von Dampf in Gegenwart eines Substrates werden mit der Methode der molekulardynamischen Simulation untersucht. Simulationen, die auf diesem Gebiet bislang durchgeführt wurden, haben sich nur wenig mit der detailgetreuen Beschreibung des Substrats beschäftigt. Hier werden die Dynamiken der Gasphase und der Oberfläche simultan behandelt. Es werden zwei Fälle untersucht: Die Kondensation von Argon und die Kondensation von Platin auf Polyethylen-Filmen. Der wesentliche Unterschied zwischen den beiden Systemen besteht in die relative Stärke der Wechselwirkung zwischen dem Adsorbat und dem Substrat.

Das United-Atom-Modell wird eingesetzt, um die Wechselwirkung zwischen den Methylgruppen des Polymers zu modellieren. Die Eigenschaften von Polyethylen in der Bulkphase wie die Temperatur des Glasübergangs, die Dichte und die Ausbildung von *gauche*-Defekten in der kristallinen Phase können mit diesem Modell für die betrachtete Untersuchung hinreichend genau beschrieben werden. Die Wechselwirkung zwischen den Argon-Atomen kann sehr gut mit dem Lennard Jones-Potential wiedergegeben werden. Die Embedded-Atom-Methode wird benutzt, um die Wechselwirkung zwischen den Platinatomen zu modellieren. Bei Metallen sind Mehrkörpereffekte wichtig, die mit der Embedded-Atom-Methode mit einem Berechnungsaufwand, der vergleichbar zu Paarpotentialen ist, implementiert werden können. Die Kreuzwechselwirkungen zwischen den Atomen und Gruppen werden hier mit dem Lennard Jones-Potential und den Lorentz-Berthelot-Kombinationsregeln beschrieben.

Das Ziel dieser Untersuchung ist es, die Dynamik der heterogenen Keimbildung zu beschreiben und untersuchen und die Variablen zu identifizieren, die das Wachstum und die Strukturbildung von Clustern auf Oberflächen bestimmen. Außerdem werden die Keimbildungsraten bestimmt und die mögliche Modifikationen des Substrates während der Kondensation untersucht. Zu diesem Zweck wurden verschiedene Systeme mit unterschiedlicher Übersättigung der Gasphase und unterschiedlichen Substrattemperaturen simuliert. Die Berechnungen der stationären Keimbildungsraten in der

Gasphase und auf der Oberfläche werden aus der Clustergrößenverteilung mit der Methode von Yasuoka and Matsumoto durchgeführt.

In den verschiedenen Simulationssystemen wurden unterschiedliche Wachstumsmechanismen beobachtet. Argon tendiert dazu auf der Oberfläche als zweidimensionale Inseln zu kondensieren, die koaleszieren und schließlich Lagen auf der Polymeroberfläche bilden. Konsistent mit dieser Art des Wachstums kann die Kondensation in diesem Bereich von relativ leicht übersättigten Systemen bis hin zu untersättigten Systemen mit einem zweidimensionalen Modell im Rahmen der klassischen Keimbildungstheorie beschrieben werden.

Platincluster kondensieren als dreidimensionale Inseln und benetzen die Polymeroberfläche nur partiell. Zum ersten Mal wurde die Einbettung von Metallatomen und im Inertgas gebildeten Clustern in einem Polymersubstrat, wie sie im Experiment beobachtet wurde, in molekulardynamischen Simulationen erhalten. In Abhängigkeit von der Größe der Platincluster diffundieren sie in die Polymermatrix. Dies geschieht sogar bei Temperaturen, die unterhalb des Glasübergangs des Polymers liegen.

Die Programme und Routinen, die für die Simulationen und für die Analyse der Simulationsergebnisse benötigt werden, wurden speziell für die hier durchgeführte Untersuchung neu entwickelt. Hierzu zählen Programme für molekulardynamische Simulationen im  $NpT$  und  $NVT$  Ensemble zur Vorbereitung der Polymerfilme sowie für die Kondensationssimulationen von Argon und von Platin auf den Polyethylenfilmen. Ausserdem wurden Programmroutinen für die Analyse der Simulationsergebnisse entwickelt. Hierzu zählen a) die Berechnung der radialen und der Winkelverteilungsfunktionen, der Dichteprofile zur Charakterisierung der Polymere, b) die Entwicklung von Algorithmen zur Erkennung von Clustern in der Gasphase und insbesondere an der Oberfläche und c) die Entwicklung von Routinen zur Visualisierung der durchgeführten Simulationen.

# Abstract

Heterogeneous nucleation phenomena, in particular the condensation of vapors in presence of a substrate, are studied by molecular dynamics simulations. The simulations reported to this date have paid little attention to the description on the substrate. Here the dynamics of the vapor phase and the surface are simultaneously treated. Two cases are studied: the condensation of argon and the condensation of platinum on polyethylene films. The fundamental difference between both systems is the relative strength of the adsorbate-substrate interactions.

The United Atom Method is used to represent the interactions of methyl groups within the polymer. The properties of polyethylene in the bulk phase such as the glass transition temperature, the density and the formation of *gauche* defects in the crystalline phase can be well described with this model. The interactions between argon atoms can be well represented by the Lennard Jones potential. The Embedded Atom Method is used to describe interactions between platinum atoms since many body effects, important in metals, can be incorporated with a computation requirement similar to pair potentials. Cross interactions between different types of atoms and groups are here approximated by the Lennard Jones potential with Lorentz-Berthelot combining parameters.

The aim of this investigation is to describe the dynamics of heterogeneous nucleation and to establish the variables which control the growth and structure formation of clusters on the surface, the nucleation rates, and possible modifications of the substrate during condensation. For this purpose, different conditions of the saturation of the vapor phase and temperature of the substrate were simulated in each of the systems studied. Stationary nucleation rates in vapor phase and on the surface are obtained from cluster size statistics using the method of Yasuoka and Matsumoto.

Different growth mechanisms were observed in for the simulated systems. Argon tends to condense on the surface as two-dimensional islands which finally coalesce as layers on the polymer surface. Consistent with this type of growth the condensation in the regime of low saturated and undersaturated vapors can be explained by a two-dimensional model within the frame of the classical nucleation theory.

Platinum clusters condense as three-dimensional islands and partially wet the polymer surface. For the first time the embedding of metal atoms and metal clusters growth into a polymer substrate, as observed in experiments, is attained by large-scale molecular simulations. Depending on their sizes, the platinum clusters can diffuse into the polymer matrix even at temperatures lower than the glass transition of the polymer.

The routines used for the simulation and analysis have been specially developed for the systems studied. Among them are  $NpT$  and  $NVT$  ensemble molecular dynamics simulations for the preparation and equilibration of thin polymer films, simulations of condensation of argon and platinum on polyethylene films. Furthermore routines developed for the analysis of simulation results include the calculation of a) radial distribution functions, torsion angle distributions and density profiles for the characterization of polymers, b) algorithms for the recognition of clusters in bulk and on a surface and c) routines for the visualization of the performed simulations.

# Table of Contents

<b>1. Introduction.....</b>	<b>1</b>
1.1 Nucleation Theory .....	3
1.1.1 Homogeneous Nucleation.....	5
1.1.2 Heterogeneous Nucleation.....	7
1.1.3 Nucleation Work.....	9
1.1.4 Nucleation Rate.....	11
1.2 Polymers .....	14
1.2.1 Molecular Modelling of Polymers.....	15
1.2.2 Crystalline Phases of Polyethylene.....	16
1.2.3 Glass Transition in Polymers.....	19
<b>2. Methods.....</b>	<b>25</b>
2.1 Molecular Dynamics.....	26
2.1.1 Integration Algorithm .....	28
2.1.2 Definition of Thermodynamic Properties.....	30
2.1.3 Cut-off Radius Approximation .....	31
2.1.4 Neighbor Lists.....	33
2.1.5 Periodic Boundaries and Minimum Image Convention .....	34
2.1.6 Control of Temperature and/or Pressure.....	35
2.1.6.1 Nosé-Hoover Thermostat, $NVT$ Ensemble.....	38
2.1.6.2 Simultaneous Control of Temperature and Pressure, $NpT$ Ensemble....	41
2.1.6.3 Simultaneous Control of Temperature and Pressure in Films .....	42
2.2 Force Fields.....	44
2.2.1 Potential Models of Noble Gases.....	45
2.2.2 Force Fields for Polymers.....	46
2.2.2.1 Potential LJ-FENE.....	46
2.2.2.2 United Atom Method (UAM).....	46
2.2.2.3 All-Atoms Models .....	47
2.2.3 Many Body Potentials for Metals, Embedded Atom Method (EAM).....	47
<b>3. Results.....</b>	<b>51</b>
3.1 Simulations of Polyethylene .....	51
3.1.1 UAM Models for Polyethylene.....	52
3.1.2 Crystalline Phases of Polyethylene (UAM).....	55
3.1.3 Glass Transition of Polyethylene (UAM).....	59
3.1.3.1 Glass Transition of Bulk PE (UAM) .....	60
3.1.3.2 Glass Transition of PE (UAM) Films .....	61
3.2 Condensation of Ar on PE Films .....	63
3.2.1 Characterization of Ar Clusters .....	63
3.2.1.1 Interfacial Tension and LV Equilibrium Densities.....	64
3.2.1.2 Contact Angle .....	67
3.3 Condensation of Pt on PE Films .....	82
3.3.1 Simulation Methodology .....	82
3.3.1.1 EAM Model for Platinum.....	84
3.3.1.2 Cross Interactions in the System PE-Pt-Ar.....	85
3.3.2 Results.....	86

<b>4. Summary and Outlook</b> .....	<b>97</b>
<b>Appendix</b> .....	<b>99</b>
A.1 Neighbor Lists .....	99
A.2 Expressions for the Calculation of the Forces.....	103
A.2.1 Useful Formulas .....	103
A.2.2 Valence Terms.....	104
A.2.2.1 Valence Bond .....	104
A.2.2.2 Bending .....	106
A.2.2.3 Torsion.....	108
A.2.3 Non-Bonded Interactions .....	112
A.2.3.1 Lennard Jones Potential.....	112
A.2.3.2 Embedded Atom Method (EAM).....	113
A.3 Virial Contributions to the Pressure .....	116
A.3.1 Valence Contributions .....	117
A.3.1.1 Valence Bond .....	117
A.3.1.2 Bending .....	119
A.3.1.3 Torsion.....	120
A.3.2 Non-bonded Interactions .....	121
A.4 Clusters Recognition Algorithm.....	122
<b>References</b> .....	<b>126</b>
<b>Acknowledgments</b> .....	<b>132</b>
<b>Erklärung</b> .....	<b>133</b>
<b>Curriculum Vitae</b> .....	<b>134</b>

# Symbols and Abbreviations

## Latin Characters

$a$	lattice parameter
$a^*$	deviation of the lattice parameter $a$ from its equilibrium value $a_0$
$a_0$	equilibrium value of lattice parameter $a$
$a_{\text{ef}}$	effective molecular area
$b$	lattice parameter
$c$	lattice parameter
$b_n$	shape factor of a two-dimensional island
$c_n$	shape factor of a three-dimensional cluster
$d$	dimension of the system
$f_n$	frequency of monomer attachment to a cluster of size $n$
$f_n^*$	frequency of monomer attachment to nucleus
$g_n$	frequency of monomer detachment from a cluster of size $n$
$g$	degrees of freedom
$g(r)$	radial distribution function
$h$	height of a two-dimensional island
$k_B$	Boltzmann constant
$l$	film thickness
$m_i$	molecular/atomic mass of a particle $i$
$m$	number of groups in a polymer chain
$n$	cluster size
$n^*$	nucleus size
$n_t$	threshold cluster size
$n_d$	number of outer $d$ -electrons
$n_s$	number of outer $s$ -electrons
$n_v$	valence number
$p$	pressure
$p_N$	normal component of the pressure tensor
$p_T$	tangential component of the pressure tensor
$p_B$	pressure of the barostat
$p_{\text{eq}}$	equilibrium pressure
$p_c$	critical pressure
$p_i$	generalized momentum of a particle $i$
$q_i$	generalized coordinate of a particle $i$
$r$	Distance
$\mathbf{r}_i$	position vector of a particle $i$
$r_c$	cut-off radius
$r_l$	Verlet radius
$r_{ij}$	distance of a pair
$s$	additional variable of the Nosé-Hoover thermostat

$t$	time
$\Delta t$	integration step
$w$	characteristic frequency
$w_T$	frequency of the thermal response of a system coupled to a thermostat
$z_c$	coordination index
$z_i$	number of particles in the $i$ -th shell of neighbors
$A_i$	area of the interface cluster-substrate
$A_s$	area of the interface substrate-vapor
$B$	bulk modulus
$C_0$	concentration of nucleation sites
$C_n$	concentration of clusters of size $n$
$C_n^*$	equilibrium concentration of nucleus
$C_{\alpha\beta}$	elastic constants expressed in Voigt notation
$E_0$	sublimation energy at zero temperature
$E_{\text{sub}}$	sublimation energy
$F$	force vector
$F(\rho)$	embedding energy function
$G$	Gibbs energy of the system
$G_{\text{ex}}$	excess energy of a cluster
$\Delta G_n$	formation work of a cluster of size $n$
$\Delta G^*$	formation work of a nucleus
$I$	impingement rate
$J$	nucleation rate
$J_n$	net flux through the bin $n$ of the cluster size distribution
$L^\alpha$	length of the simulation box in the direction $\alpha$
$M$	molecular weight
$M_\eta$	mass parameter of the Nosé-Andersen barostat
$N$	number of particles
$N_a$	number of nucleation active centers
$Q$	mass parameter of the Nosé-Hoover thermostat
$S$	supersaturation ratio
$S'$	entropy of the system
$T$	temperature
$T_B$	temperature of the heat bath
$T_c$	critical temperature
$T_g$	glass transition temperature (film)
$T_{g\infty}$	bulk glass transition temperature
$T_m$	melting temperature
$U$	potential energy function
$V$	volume
$V_1$	volume of a cluster in condensed phase
$W$	virial contribution
$Z(r)$	effective charge function



## Greek Symbols

$\alpha$	direction: $x$ , $y$ or $z$
$\alpha_s$	sticking coefficient
$\gamma$	specific surface energy of the interface cluster-vapor
$\gamma_i$	specific surface energy of the interface cluster-substrate
$\gamma_s$	specific surface energy of the interface substrate-vapor
$\Delta\gamma$	effective specific surface energy
$\delta(r)$	Dirac delta function
$\delta_{ij}$	Kronecker delta operator
$\varepsilon$	Lennard Jones energy parameter (energy minimum of the potential)
$\varepsilon_{ijk}$	permutation operator
$\phi$	torsion angle between four consecutive groups in a chain
$\phi(r)$	Coulomb pair potential
$\zeta$	friction coefficient of the Nosé-Hoover thermostat
$\Theta(r)$	Heaviside function
$\theta_w$	contact angle
$\theta$	bending angle between three consecutive groups in a chain
$\lambda$	scaling factor in the velocity-scaling method
$\kappa$	specific edge-energy of a two dimensional cluster
$\mu$	chemical potential
$\Delta\mu$	supersaturation
$\rho$	density
$\rho_l$	number density of particles in condensed phase
$\rho^{\text{at}}$	atomic electron density
$\rho_h$	host electron density
$\rho_{\text{eq}}$	equilibrium vapor density
$\sigma$	Lennard Jones parameter (zero of the potential)
$\tau$	characteristic time
$\tau_B$	relaxation parameter of the Berendsen thermostat
$\nu$	cooling rate
$\varphi$	setting angle
$\Psi(\theta_w)$	Volmer function of the wetting angle
$\Psi(r)$	double- $\zeta$ -wave functions of the Hartree-Fock approximation
$\Omega$	equilibrium volume per atom
$\Phi$	surface energy of a cluster
$\Delta$	difference
$\nabla$	gradient
$\partial$	differential

## Others

$\mathcal{H}$	Hamiltonian of the system
$\mathcal{K}$	kinetic energy of the system

$\mathcal{L}$	Lagrangian of the system
$\mathcal{U}$	potential energy of the system
$\chi$	thermodynamic variable
$z$	Zeldovich factor

### Abbreviations

HEN 2D	heterogeneous two-dimensional nucleation
HEN 3D	heterogeneous three-dimensional nucleation
HON	homogeneous nucleation
EAM	embedded atom method
MC	Monte Carlo
MD	molecular dynamics
LJ	Lennard Jones
LRC	long range corrections
RDF	radial distribution function
UAM	united atom method





# Chapter 1

## Introduction

The nucleation of a vapor in presence of a substrate has been a topic of current interest in experiments<sup>1-8</sup>, theory<sup>10-12</sup> and simulations<sup>13-19</sup>. A detailed understanding of the growth phenomena on surfaces requires the study of the microscopic processes such as the nucleation in vapor phase, adsorption on the surface, diffusion and coalescence of clusters in/on the substrate.

Experimental studies based on Electron Transmission and Scanning Tunnelling Microscopy determinations<sup>7,8</sup> have been mainly focussed on the epitaxial growth of metal atoms on flat crystalline surfaces at low deposition rates. These experiments have served as a guide for the development of the nucleation theory.

From a technological point of view there is an increasing interest in polymer-metal systems such as metalized plastics, metal nanostructures (nanowires) on polymer templates and nanocomposites formed by finely distributed metal particles in polymers<sup>20,22</sup>. Additionally, the use of organic polymers as templates in the production of metal nanoparticles has been shown to be an effective method to control their sizes and prevent their oxidation by encapsulation. Concerning the preparation of polymer-metal nanocomposites there are any straightforward synthesis route to obtain nanoclusters of an appropriate narrow size distribution with high concentration. Several methods as colloidal syntheses, solvent-based techniques and sputtering have been used to produce nanocomposite materials containing magnetic nanoclusters embedded in different types of matrices. The limitations of these methods arise from the difficulty to control the nanoparticle size independently of the metal volume fraction. The vapor

deposition of metals on polymers templates is a promising solvent-free alternative, since it provides an easy control over the nanocluster growth<sup>1</sup>.

Experiments of condensation of low-reactive metals on polymeric substrates have revealed that their clusters deposit on the surface and tend to build crystallites<sup>23,24</sup>. Larger clusters remain near the polymer surface while small clusters diffuse into the polymer matrix, even below the glass transition temperature of the polymer  $T_g$  (Fig. 1.1). This result has been attributed to the existence of a liquid-liquid layer near the surface of the film<sup>25</sup> and also interpreted as a change of the glass temperature near the surface<sup>26</sup>. The temperature at which the metal clusters can embed in the polymer film is lower than its glass transition temperature, and strongly as the average size of the clusters decreases<sup>27</sup>. Experiments<sup>24</sup> also show that the extent of the metallization is sensible to the previous thermal treatment of the polymer substrate since of its effect on the morphology and free volume of the polymer. The temperature of the substrate controls the diffusion of the metals clusters in the polymer matrix and determines their size distribution.

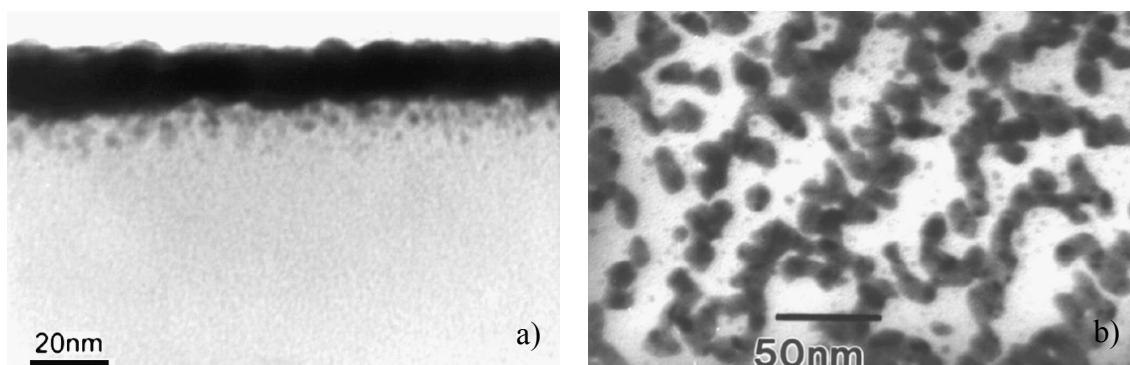


Figure 1.1. Diffusion of small metal clusters on polymer films and deposition pattern of non-reactive metal clusters on polymer substrates<sup>24</sup>. a) TEM micrograph of the interface gold-trimethylcyclohexane-polycarbonate (TMC-PC) at 80 °C, under the glass transition temperature of the polymer substrate  $T_g=235$  °C. Au is shown in dark. b) Lateral view of the Figure a).

Molecular simulations of condensation of vapors in presence of an active surface have been focussed on the study of confinement effects in phase separation<sup>17-19</sup> and also on the effect of strength of the adsorbate-substrate interactions on the growth mechanism. Simulation results of metastable vapors between walls exhibit two differentiated regimes; at small distances between walls the vapor behaves as a capillary system confined in a slit pore, where the vapor experiences a crossover to bulk behavior upon increasing the distance between the walls. Depending on the strength of the attraction between the substrate and the condensing particles, the surface can be

partially or complete wetted. Weak attractive interactions can even inhibit the condensation on the surface because of the formation of a depletion zone where the vapor density is lower than the bulk one. These studies have served as proof of the nucleation models<sup>14-16</sup>.

In the simulations reported to this date little attention has been paid to the description of the substrate. In some cases it has been represented as a semi-infinite plane which interacts with the vapor according to an effective potential. Usually a Lennard Jones 9-3 potential is used, since it nearly represents the effective interaction of a particle with a wall of uniform distributed particles<sup>13</sup>. In these simulations the substrate is modelled as a continuous static medium. In other cases the surface is represented as isothermal flat monolayer of atoms. The control of the substrate temperature is attained by a strong coupling with phantom particles<sup>15</sup>.

As an extension of these investigations, the heterogeneous nucleation of vapors is simulated here using a more realistic model of the substrate. Polymer substrates are represented as arrangements of linear flexible chains. The dynamics of nucleation, condensation and changes in the substrate are simultaneously treated.

## 1.1 Nucleation Theory

The direct observation of natural phenomena as rain and snowfalls indicate that the formation of a new phase takes place in a progressive and not in a simultaneous way. Theoretically, the simultaneous and spatial uniform condensation has a higher energetic barrier. Nanoscopic embryos of the new phase produced by local density fluctuations appear in the old phase. The kinetics and the path which describe a phase transformation are called nucleation. Clusters of condensate are randomly formed in the vapor phase, whose sizes can be measured equivalently in terms of their volume or number of atoms. For this purpose a definition of the dividing surface between the phases is required<sup>9</sup>. The clusters of size  $n = n^*$  in unstable balance with the vapor are named nuclei. Only the clusters bigger than the nuclei, supernuclei, are able to grow spontaneously until reaching a macroscopic size. The stationary rate of supernuclei generation  $J$  is a measure of the dynamics of the nucleation. It is expressed as the number of clusters generated per time unit and volume unit, in the case of homogeneous nucleation, and per surface unit for heterogeneous nucleation.

The early investigations of Farkas, Volmer and Weber, Becker and Döring, Stranski and Kaischew, Frenkel and Zeldovich among others on the search of a kinetic description of the aggregation phenomena and phase transitions led during the last century to the foundations of the classical nucleation theory<sup>28</sup>. The value of this analytical approach is that it provides a direct interpretation of experimental and simulation results since it establishes a link between the relevant variables of the transition; nucleation rate, formation energy and size of the nucleus, with the macroscopic properties of the system<sup>29</sup>. In the following sections some models for the description of the condensation of a vapor phase are briefly presented.

### 1.1.1 Thermodynamics of Phase Transitions

First order phase transitions, for example the condensation of a vapor phase, can be well described by classical thermodynamics arguments; an open system tends spontaneously to a state of minimum free energy. The free Gibbs energy  $G$  of a pure substance is a function of the temperature  $T$ , pressure  $p$  and number of particles of the system  $N$ ,  $G = G(T, p, N)$ . As an extensive thermodynamic quantity it can be written as  $G = N\mu(T, p)$  and its total differential is given by

$$dG = -S'dT + Vdp + \mu dN \quad (1.1)$$

where  $S'$ ,  $V$  and  $\mu$  are respectively the entropy, volume and chemical potential of the thermodynamic system.

The Gibbs energy of a fluid along a subcritical isobar shows two local minima (see Fig 1.2); one of them corresponds to the gas phase, the other to the liquid. At low pressure the gas phase is stable since its energy minimum is lower than the liquid one. The Gibbs free energy of the system reaches a global minimum at a given pressure  $p_{eq}$  as the energy of both phases converges to the same value. At this point both liquid and vapor phases coexist in a stable equilibrium. Above the pressure  $p_{eq}$  the vapor is metastable because of the positive the energy difference between the vapor and the liquid phase. In other words, the system can spontaneously condense in order to reduce its Gibbs energy.

The difference of molar Gibbs energy between the two phases, given by Equation (1.2), is called supersaturation



$$\Delta\mu = \mu_v - \mu_l = k_B T \ln S + V_0(p - p_{\text{eq}}) \approx k_B T \ln S. \quad (1.2)$$

$V_0$  denotes the molar volume of the condensed phase. The supersaturation is the driving force for the condensation. Here  $S$ , the supersaturation ratio, is defined as the ratio between the pressure of the system and the equilibrium pressure at the temperature of the system  $S = p / p_{\text{eq}}(T)$ .

The region of mechanically stable,  $(\partial p / \partial V)_T < 0$ , supersaturated states,  $S > 1$ , defines a metastable region in the phase diagram. The metastability in a one-component system is a necessary condition in order that vapor-condensate transition occurs, but it says nothing concerning the dynamics and path of the transition; this condition only establishes the feasibility of the phase change.

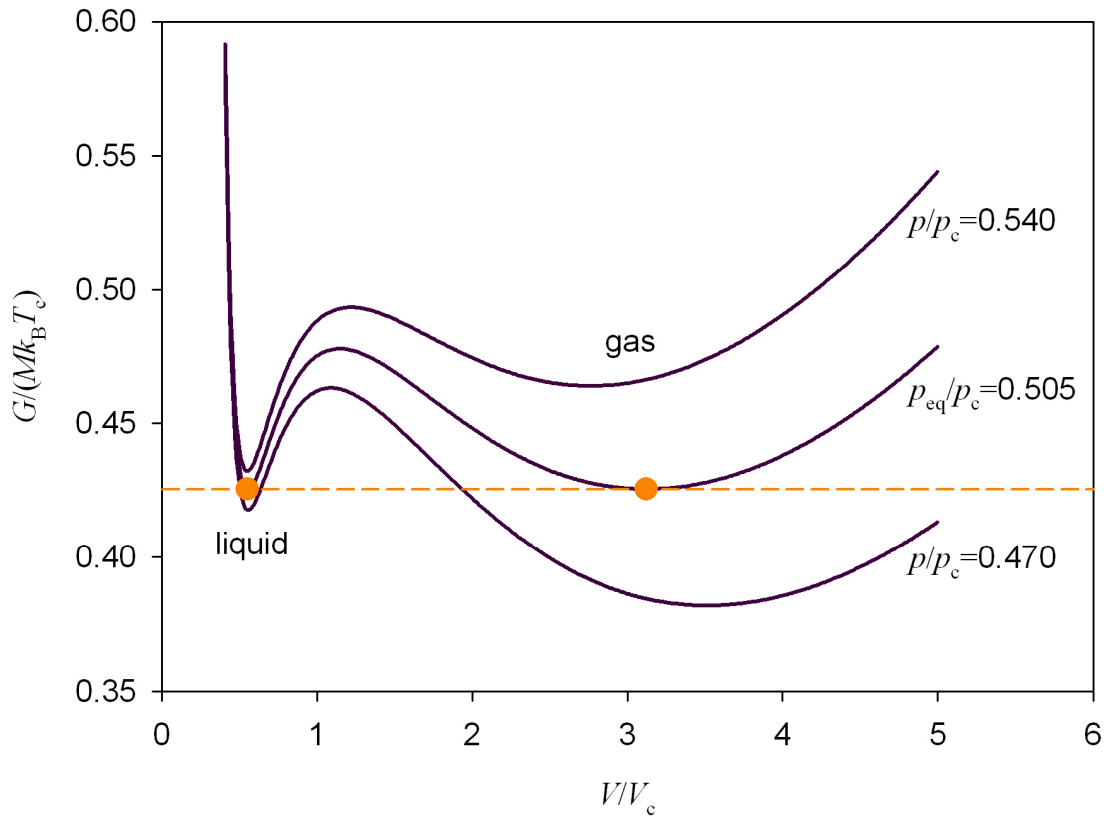


Figure 1.2. Gibbs energy curves of a Van der Waals fluid along subcritical isobars<sup>9</sup> at  $T/T_c=0.85$ . Both liquid and gas phase are related to a minimum of the energy. A stable phase equilibrium is reached at  $p_{\text{eq}}/p_c=0.505$ .

### 1.1.2 Homogeneous Nucleation

The formation work of an  $n$ -sized cluster is equal to the difference of the system free energy between its final and initial state; before and after the formation of the

cluster. This difference would be simply equal to  $-n\Delta\mu$  if the atoms formed simultaneously a sufficiently large bulk condensed phase, but this is not the case: The nucleation takes place in the time interval where the clusters have nanoscopic sizes. The difference between the properties of a cluster and the properties of the corresponding condensed bulk phase introduces an additional contribution to the work  $\Delta G$  necessary to build a cluster

$$\Delta G_n = -n\Delta\mu + G_{\text{ex}}. \quad (1.3)$$

The excess free energy term  $G_{\text{ex}}$  takes in to account this additional contribution. Its definition requires approximations and can be expressed as<sup>9</sup>

$$G_{\text{ex}} = \Phi - (p_n - p)V_1 + \int_p^{p_n} V_1(p)dp. \quad (1.4)$$

Here  $V_1$  denotes the volume of the cluster and  $p_n$  the pressure inside the cluster. The first term  $\Phi$  in Equation (1.4) is the cluster surface energy, the next one is the energy change related to the variation of pressure experienced by the control volume  $V_1$  after the formation of a cluster and the last term is the difference between the potential energy of the particles in the cluster and in the corresponding bulk phase. The excess energy reduces to surface energy of the cluster  $G_{\text{ex}} = \Phi$ . A reasonable good approximation for a cluster in liquid and solid phase is to assume that its volume depends on the temperature only  $V_1 = V_1(T)$ . The cluster surface energy is assumed proportional to the area of the cluster surface  $\Phi = \gamma A$ , where  $\gamma$  is the specific surface energy of the interface between the cluster and the vapor. Furthermore, the surface of regular shaped bodies is related to the volume by  $A = c_n V_1^{2/3}$ , where  $c_n$  is the cluster shape parameter, for example  $c_n = (36\pi)^{1/3}$  for a sphere and  $c_n = 6$  for a cube. Upon considering a uniform density inside the cluster the amount of atoms in a cluster can be approximated as  $n = \rho_1 V_1$ , where  $\rho_1$  is the number density of the condensed phase at the temperature of the cluster. Under these assumptions the formation work of a cluster of size  $n$  is

$$\Delta G_n = -n\Delta\mu + a\gamma_n n^{2/3}, \text{ where } a = c_n \rho_1^{-2/3}. \quad (1.5)$$

### 1.1.3 Heterogeneous Nucleation

Heterogeneous nucleation takes place when the old and forming phases are in contact with a third phase or molecular species. According to the shape and dimension of the clusters different kinds of heterogeneous nucleation can be defined. Two idealizations for the vapor condensation on a substrate are perused here; clusters grow as droplets forming a contact angle with the surface (HEN 3D) and clusters grow as disks of fixed thickness along their periphery (HEN 2D).

The denominations 2D and 3D refer to the growth directions of the clusters. Equation (1.5) can be formulated in more general terms to describe the homogeneous HON and heterogeneous HEN cases of nucleation in three dimensions 3D, for this purpose the surface contribution of the Equation (1.4) is replaced by the energy change of the system after the adhesion of a cluster<sup>9</sup>

$$\Phi = -\gamma_s A_i + \gamma_i A_i + \gamma A \quad (1.6)$$

$A_i$  denotes here the contacting surface between the cluster and the substrate,  $A$  the area between the cluster and the vapor and  $A_s$  the area between the substrate and the vapor (see Fig. 1.4).

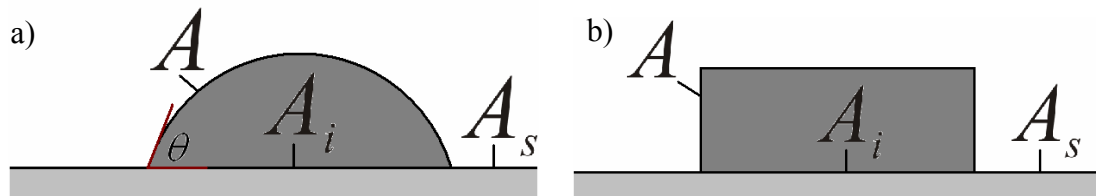


Figure 1.4. Geometrical quantities involved in the classical nucleation theory for a) cap-shaped clusters and b) cylindrical clusters, they growth in this case on the face adjacent to the substrate.

For cap-shaped clusters the difference  $\gamma_s - \gamma_i$  is written in terms of the contact angle by means of the Young's relation

$$\gamma_s - \gamma_i = \gamma \cos \theta_w \quad (1.7)$$

The contact angle  $\theta_w$  is defined as the internal angle between the surface and the tangent plane on the cluster basis (Fig. 1.4a). The formation work of a cluster on a surface is<sup>9,29,30</sup>

$$\Delta G_n = -n\Delta\mu + a\gamma_{\text{ef}}n^{2/3}. \quad (1.8)$$

Where  $\gamma_{\text{ef}} = \psi^{1/3}(\theta_w)\gamma$  is an effective value of the specific surface energy,  $a = c_n\rho_1^{-2/3}$  with  $c_n$  the shape factor of a sphere and  $\psi$  the Volmer factor (Fig. 1.5)

$$\psi(\theta_w) = (1/4)(2 + \cos\theta_w)(1 - \cos\theta_w)^2, \quad \theta_w \in [0^\circ, 180^\circ], \quad \psi \in [0, 1]. \quad (1.9)$$

Homogeneous nucleation can be treated as a particular case of heterogeneous three-dimensional nucleation (1.8). The non-wetting case  $\theta_w = 180^\circ$  physically corresponds to an inert surface or strong interactions between ad-atoms. As the relative interaction between the surface and the ad-atoms increases, the ratio height/surface of the cap decreases as the contact angle. In the extreme  $\theta_w = 0^\circ$ , the shape of the cluster converges to a flat layer on the surface.

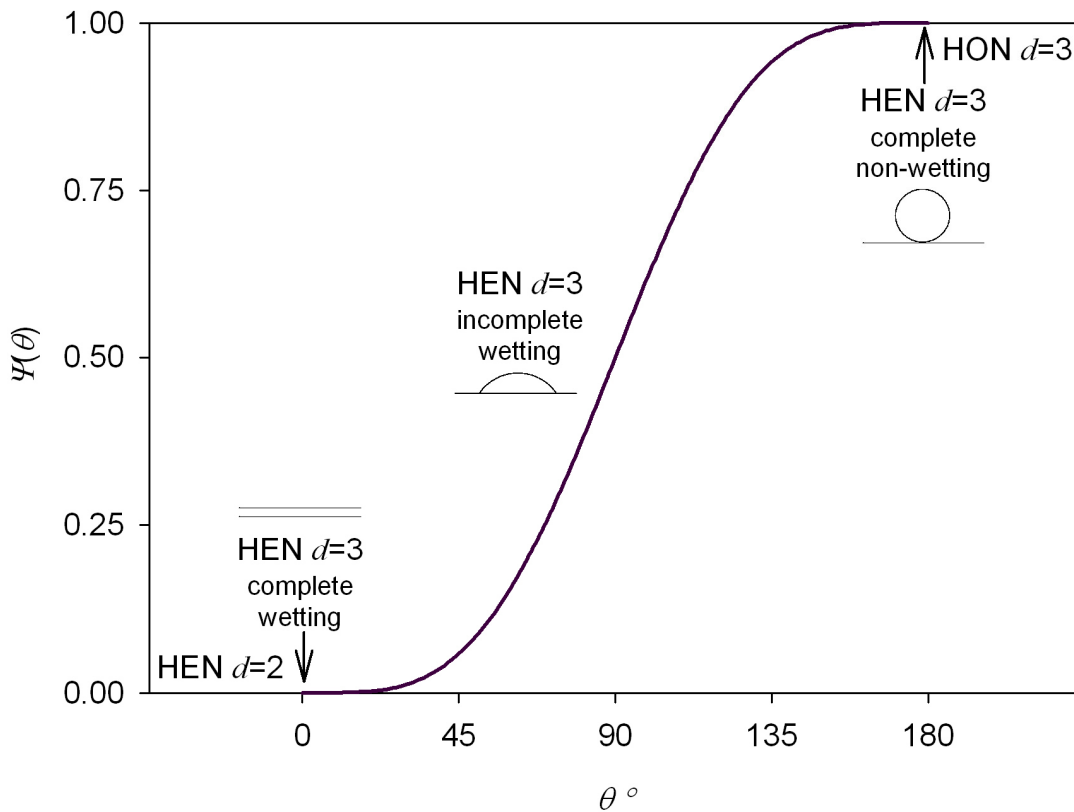


Figure 1.5. Dependence of the activity factor on the contact angle according to the Equation (1.9). The heterogeneous two-dimensional growth mechanism continuously evolves to the three-dimensional homogeneous nucleation as the contact angle increases.

When  $\gamma_s - \gamma_i > \gamma$ , the definition of the contact angle loses its usual meaning; the clusters completely or partially cover the surface with islands. These clusters of very

low contact angle grow in two dimensions a through their peripheral surface (see Fig 1.4b). This growth mechanism is called heterogeneous two-dimensional nucleation (HEN 2D). Therefore, the formation work of a island of size  $n$  is<sup>9,30</sup>

$$\Delta G_n = -n(\Delta\mu - a_{\text{ef}}\Delta\gamma) + b_n\kappa n^{1/2} \quad (1.10)$$

$a_{\text{ef}} \approx V_{10}/h$  is an effective molecular area,  $h$  is the height of the cluster and  $b_n$  is a shape factor of the island, for example for a cylinder  $b_n = 2(\pi a_{\text{ef}})^{1/2}$ ,  $\kappa \approx \gamma h$  is the specific edge energy of the cluster.  $\Delta\gamma$  is an effective specific surface energy defined by

$$\Delta\gamma = \gamma + \gamma_i - \gamma_s. \quad (1.11)$$

$\Delta\gamma < 0$ ,  $\Delta\gamma = 0$  and  $\Delta\gamma > 0$  correspond to incomplete, complete and ‘better-than-complete’ wetting respectively. According to the Equations (1.8) and (1.10), the driving force for the HEN 2D condensation is given by  $\Delta\mu - a_{\text{ef}}\Delta\gamma$ . Thus, the condensation of an undersaturated vapor in presence of an active surface is even possible if the term  $\Delta\mu - a_{\text{ef}}\Delta\gamma$  is positive.

#### 1.1.4 Nucleation Work

A thermodynamic law common to natural transformations is that the most favourable path for a change is the minimum energy one. The condensation of a vapor is not an exception to this rule.

The competition between the negative bulk and the positive surface energy contributions to the work of formation of a cluster, Equations (1.5), (1.8) and (1.10), leads to a maximum energy  $\Delta G^*$  (Fig. 1.3a). It represents the energetic barrier of nucleation. Energy must be invested to build a cluster smaller than the nucleus; when a cluster reaches a supercritical size it grows spontaneously to observable sizes.

The size of the nucleus  $n^*$  and the formation work of a nucleus  $\Delta G^* = \Delta G(n^*)$  are defined by the maximization conditions  $d\Delta G_n / dn = 0$  and  $d^2\Delta G_n / dn^2 < 0$ . For the HEN and HON 3D models results

$$n^* = \frac{8}{27} \left( \frac{a\gamma_{\text{ef}}}{\Delta\mu} \right)^3 \quad \text{and} \quad \Delta G^* = \frac{4}{27} \frac{a^3 \gamma_{\text{ef}}^3}{\Delta\mu^2} = \frac{1}{2} n^* \Delta\mu \quad (1.12)$$

while for the HEN 2D model this condition leads to

$$n^* = \frac{1}{4} \left( \frac{b_n \kappa}{\Delta\mu - a_{\text{ef}} \Delta\gamma} \right)^2 \quad \text{and} \quad \Delta G^* = \frac{b_n^2 \kappa^2}{\Delta\mu - a_{\text{ef}} \Delta\gamma} = n^* (\Delta\mu - a_{\text{ef}} \Delta\gamma). \quad (1.13)$$

The Gibbs-Thompson Equation (1.12) shows the dependence of the nucleus size on the supersaturation ratio<sup>30</sup>. The nucleus size and formation work of the nucleus are monotonously decreasing functions of the saturation.

The change in the Gibbs energy associated to the spatially uniform condensation of  $N$  particles in unstable gas phase, for example the gas phase at  $T/T_c=0.85$  for the isobar  $p/p_c=0.540$  (Fig. 1.2) is  $\Delta G = N\Delta\mu$ . The Equations (1.12) and (1.13) indicate that the energy barrier for the local condensation of clusters is about  $n^* \Delta\mu$ , much lower than the barrier for the spatially uniform condensation; since  $n^* < N$ . The nucleus size and the nucleation barrier decrease in presence of an active surface because of the reduction of the specific energy of a cluster (Fig. 1.3b).

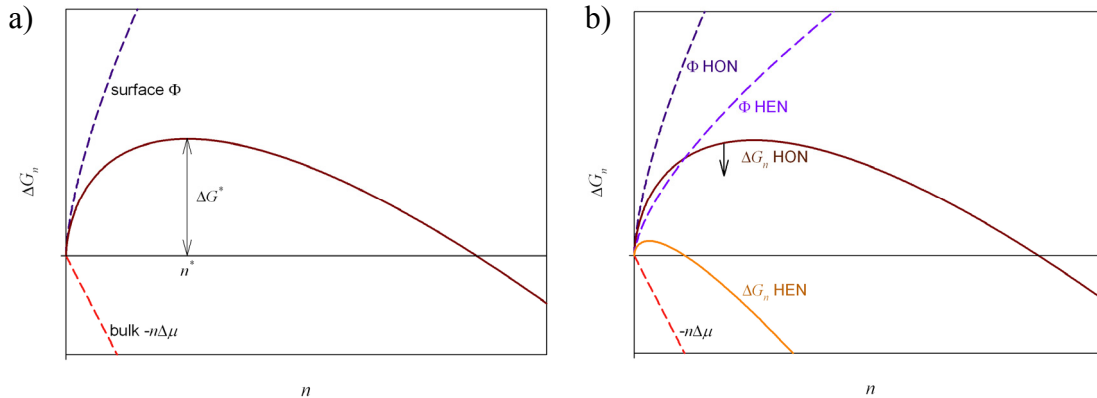


Figure 1.3. Energy of formation of cluster  $\Delta G_n$  versus the cluster size  $n$ . a) At low cluster sizes the positive surface contribution dominates over the bulk one. The maximum of represents the formation work of a nucleus  $n^*$ . Clusters larger than the critical size  $n^*$  spontaneously growth b) The nucleus size and the nucleation barrier decrease when a cluster contacts a surface because of the reduction of the surface energy contribution.

The presented models of nucleation lead to different functions  $\Delta G^*$  of  $\Delta\mu$ , Equations (1.12) and (1.13). Nevertheless, all of them satisfy the relation

$$\left( \frac{\partial \Delta G^*}{\partial \Delta \mu} \right)_T \approx -n^*. \quad (1.14)$$

The Equation (1.14), called nucleation theorem<sup>31</sup>, finds important applications in the interpretation of experimental information. One of them is the direct evaluation of the nucleus size from isothermal  $J$ - $S$  data.

### 1.1.5 Nucleation Rate

The basic kinetic model of cluster growth of the classic nucleation theory was proposed by Szilard<sup>28</sup>. In his model the clusters grow according to a reversible bimolecular mechanism, the monomers attach to clusters of size  $j$  to build another of size  $j+1$



Coalescence reactions of the type  $[j] + [i] \Leftrightarrow [j+i]$ , for  $i > 1$ , are ignored. This mechanism is reasonable for the description of the condensation of a vapor phase, since the amount of monomers notably exceeds the population of larger clusters. Furthermore, the monomers have a higher mobility.

The Szilard's mechanism can be illustrated as a system of monomers contained in a semipermeable chamber at fixed saturation. The density of monomers is constant since the supercritical clusters once formed are extracted, through a membrane, whereas an identical quantity of monomers enters the system. The evolution of the cluster size distribution is governed by a detailed population balance where all the possible disintegration and generation of an  $n$ -sized cluster are accounted for by means of reactions of the type (1.15)

$$\frac{dC_n}{dt} = J_{n-1} - J_n. \quad (1.16)$$

The bin  $n$  exchanges clusters with the bins  $n-1$  and  $n+1$ ,  $C_n$  is the population of clusters of size  $n$  expressed as concentration, per volume and surface for HON and HEN respectively,  $J_n$  is the net flux through a bin  $n$  of the discrete cluster size distribution, given by

$$J_n = f_n C_n - g_{n+1} C_{n+1} \quad (1.17)$$

$f_n$  and  $g_n$  are respectively the attachment and detachment frequencies of monomers of a cluster of size  $n$ . The solution of the Equation (1.16) conduces to a Boltzmann cluster size distribution<sup>9,28</sup>

$$C_n = C_0 \exp\left(-\frac{\Delta G_n}{k_B T}\right) \quad (1.18)$$

The nucleation rate, the stationary rate at which the supernuclei are generated, is according to (1.16) equal to the aggregation ratio of monomers to the nuclei minus the rate of disintegration rate of supernuclei. The definition of the monomer detachment frequency is complex, since it depends on the properties of a cluster in its first stages of formation. For this reason the detachment contribution is normally expressed in terms of the attachment by means of the introduction of a correction factor  $z$  in the Equation (1.17) defined as

$$z = \left( -\frac{1}{2\pi k_B T} \frac{\partial^2 \Delta G_n}{\partial n^2} \Big|_{n=n^*} \right)^{1/2} \quad (1.19)$$

Then, a general expression for the stationary nucleation rate can be expressed as<sup>9,30</sup>

$$J = z f_{n^*} C_{n^*}. \quad (1.20)$$

Both the Zeldovich's factor  $z$  and the nuclei concentration in stationary regime  $C_{n^*}$  depend on the formation work  $\Delta G^*$  and size of the nucleus  $n^*$ . They are thermodynamic quantities which are defined by the Equations (1.12) and (1.13) for the different kinds of nucleation. The attachment frequency is a kinetic term which depends on the transport mechanism of monomers to the growing cluster surface. In a condensing vapor the direct impingement transport mechanism of monomers dominates, the impingement flux is given by the Herz-Knudsen<sup>9</sup> relation

$$I = \frac{P}{(2\pi m k_B T)^{1/2}}. \quad (1.21)$$



$I$  does not depend on the growth mode of the clusters; it only depends on the temperature and pressure of the vapor phase. The attachment frequency  $f_{n^*}$  is the product of the impingement flux  $I$ , the surface of the cluster in contact with the vapor where the monomers attach  $A$  and the fraction of impinging monomers which effectively attach to the cluster surface  $\alpha_s$ , called sticking coefficient

$$f_{n^*} = \alpha_s I A, \quad \alpha_s \in [0, 1]. \quad (1.22)$$

In the HON model monomers impinge over all the cluster surface in contact with the vapor  $A = an^{*2/3}$ . In HEN only a fraction of the cluster surface is in contact with the vapor, in particular for cap-shaped clusters the area of this surface is equal to

$$A = \frac{(1 - \cos \theta_w)}{2\psi^{2/3}} an^{*2/3} \quad (1.23)$$

Using the Equations (1.18) to (1.23) in (1.20) the following expression for the nucleation rate for cap-shaped clusters HEN 3D is obtained

$$J = \alpha_s \frac{C_0}{\rho_l} \frac{(1 - \cos \theta_w)}{2} \left( \frac{2\gamma}{\pi n \psi} \right)^{1/2} \left( \frac{p}{k_B T} \right) \exp\left( - \frac{\Delta G^*}{k_B T} \right). \quad (1.24)$$

This equation reduces to the HON case for the non-wetting condition  $\theta_w = 180^\circ$ .

In the HEN 2D case the monomers attach to the cluster periphery, then

$$A = b_n h n^{1/2}, \quad (1.25)$$

where  $b_n$  is a shape factor of the island. Using (1.18) to (1.22) and (1.25) the expression for the heterogeneous two-dimensional nucleation rate, HEN 2D, is

$$J = \alpha_s C_0 b_n h \left( \frac{\Delta\mu - a_{ef} \Delta\gamma}{8\pi m} \right)^{1/2} \left( \frac{p}{k_B T} \right) \exp\left( - \frac{\Delta G^*}{k_B T} \right). \quad (1.26)$$

$C_0$  is the concentration of nucleation sites, a constant in the Szilard's experiment, equal to the monomer density for the homogenous nucleation  $C_0 = \rho$ . For HEN  $C_0$  is the

concentration of active sites on the substrate surface  $N_a / A'$ , it is equal to the inverse of the substrate surface density  $1/a_{ef}$  when all the sites are active and in some cases approximated as the projection of the monomer density on a plane<sup>15</sup>  $C_0 = \rho^{2/3}$ .

Using the Boltzmann equilibrium cluster size distribution (1.18) and the general expression of the nucleation rate (1.20) the following relation is obtained:

$$-\frac{\Delta G^*}{kT} = \ln J - \ln(z f_{n^*} C_0) \quad (1.27)$$

Differentiation with respect to  $\ln S$  and combination with the nucleation theorem (1.14) provides a useful expression for the direct calculation of the nucleus size from  $J$ - $S$  data along an isotherm<sup>30</sup>

$$n^* = \left( \frac{\partial \ln J}{\partial \ln S} \right)_T - \left( \frac{\partial \ln(z C_0)}{\partial \ln S} \right)_T - 1 \quad (1.28)$$

Usually the term  $z C_0$  is supposed to be independent of the saturation. However, upon considering the vapor phase as a ideal gas,  $p = \rho k_B T$ , and taking into account the dependence of the concentration of active sites  $C_0$  on the vapor density the relation given by (1.28) is not strictly satisfied.

## 1.2 Polymers

Polymers are materials composed of macromolecules consisting of a large group of bonded repeating units, the monomers. The simplest polymers, homopolymers, are composed by identical monomers. Some examples of homopolymers are polyethylene (PE), polystyrene (PS), polyethylene oxide (PEO) and the bisphenyl-A-polycarbonate (BPA-PC). Heteropolymers are composed of more than a type of monomer. They can be very complex as the DNA, where different monomers (deoxy-ribonucleotides) are present in a large molecule<sup>32</sup>.

The applications of polymeric materials include the manufacture of food packages, plastic bags, compact discs, covers, tires and microelectronics. Of particular interest here are polymer-metal composites<sup>23</sup> and the role of polymers as substrates to support nanoscopic structures as metal nanowires<sup>20-22</sup>. One of the reasons for the

abundance of applications of polymers is the diversity in their chemical structure, ranging from simple linear homopolymers to branched polymers, hyperbranched polymers, stars, H-shaped polymers and copolymers with random or block sequences. Furthermore, polymers are versatile molecules: Their physical properties can be tailored to satisfy the requirements of specific applications; for example the viscosity and the transition from the elastic to the viscous behavior can be tailored by varying the molecular weight or the functional groups which compose the chains. They can also be used as additives to modify the viscosity of a solution. The interplay between variables such as the connectivity, length and stiffness of the chains determine the properties of a polymeric material<sup>33</sup>.

Polymers can be found in different states; crystalline, amorphous (glass, melts, rubber, gel) or in solution. In gel and rubber states they are found as interlinked chains in disordered liquid-like structures. In the crystalline state, however, the units are ordered and oscillate around defined positions of a primitive cell that is repeated along the crystal.

### 1.2.1 Molecular Modelling of Polymers

Molecular simulations have been demonstrated to be adequate methods for the determination of the structure and the statistical properties of polymers. The first step of the molecular modelling is the choice of the simulation method and the model of interaction between atoms/molecules. The available methods range from classic simulations using simple representations as the bead-spring model<sup>33-40</sup> to the use of techniques based on density functional approaches as Car-Parinello simulations<sup>41-43</sup> and Path Integral Monte Carlo<sup>44</sup>, which can account for quantum effects.

Polymers can be characterised at different levels of detail. At microscopic level the properties are determined by local vibrations of bonds and valence angles. The properties are uniquely determined by the chemical structure of the involved molecules. At coarse-grained level the atomic details of the chains lose importance and the chains can be understood as segments characterized by their flexibility. At this level the morphology is determined by the possible arrangements and different ways to pack the chains.

Chain connectivity in polymers introduces length scales which range from the length of a chemical bond to the gyration radius of a chain, covering 2 to 4 orders of

magnitude. This wide range of length scales translates into an even large relaxation time scales of amorphous polymers ranging from  $10^{-13}$  to  $10^{-3}$  s or even  $10^3$  s when glass dynamics is concerned. There is currently no single simulation technique able to efficiently describe all these length and time scales<sup>33</sup>.

Chemically realistic models are necessary for a description of polymers at short length scales. Studies of detailed interaction models highlight the importance of torsion dynamics in all relaxation process in polymeric materials. In some cases classic mechanics does not apply and quantum effects must be considered, for example, to describe the low temperature thermal behavior of macromolecular systems where light atoms are present<sup>44</sup>. However, *ab initio* methods are still restricted to the study of phenomena that occur in time and length scales considerably smaller than those that can be treated by means of force field based simulations.

The general behavior of amorphous polymer phases; glass, melt, rubber and polymers close to the glass transition, in bulk and confined geometries, have been qualitatively described using classic molecular dynamics simulations with simple coarse-grained models<sup>33-40, 45-47</sup>. On the other hand, the use of simple models makes it possible to extend the size and time scale of simulations of macromolecular systems.

## 1.2.2 Crystalline Phases of Polyethylene

Polymer crystals constitute a particular class of systems whose technological applications quickly increase due to their use in the manufacture of composite materials. In general, polymer crystals of macroscopic size are difficult to produce; therefore the characterization of the properties of the crystalline phases of these systems is complicated in laboratory.

Numerous X-ray scattering experiments, Raman spectroscopy, nuclear magnetic resonance NMR, dielectric relaxation, differential scanning calorimetry DSC and quasielastic neutron scattering experiments<sup>48-56</sup> have been made on PE to determine the unit cell parameters of these crystalline structures and to elucidate the nature of the stable phases before melting. From those investigations it has been concluded that PE, as odd paraffins, shows an orthorhombic structure at low temperature (Fig. 1.6), while at higher temperature the stable crystalline structure is hexagonal.

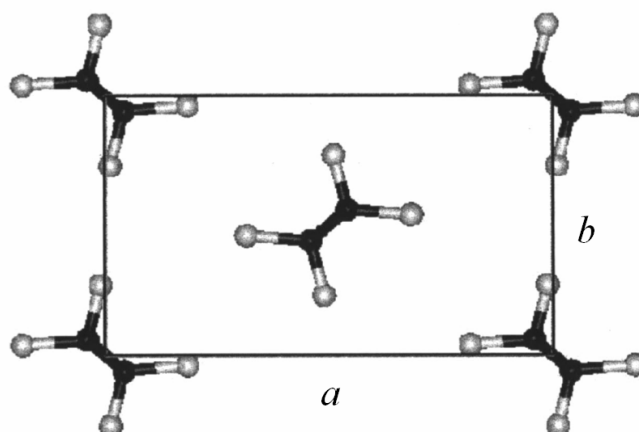


Figure 1.6.  $xy$  projection of the unit cell of the crystalline structure of polyethylene<sup>57</sup>.

Structure	$a$ [Å]	$b$ [Å]	$c$ [Å]	$a/b$
orthorhombic <sup>53</sup>	7.417	4.945	2.547	1.500
orthorhombic <sup>54</sup>	7.400	4.930	2.534	1.501
orthorhombic <sup>55</sup>	7.410	4.940	2.555	1.500
hexagonal <sup>53</sup>	8.420	4.560	—	1.846
hexagonal <sup>56</sup>	8.400	4.800	2.400	1.750

<sup>§</sup>Setting angle<sup>57</sup>  $\varphi=43^\circ$

Table 1.1. Unit cell parameters of the orthorhombic and hexagonal phases of PE

Molecular modelling is an alternative method to study the relation between microscopic characteristics like the chemical composition and the macroscopic properties of these systems. By molecular simulations it is also possible to determine the temperature dependence of mechanical and structural properties such as elastic constants, thermal expansion coefficients, lattice parameters, etc.

Martoňák *et al.*<sup>58</sup> studied the nature of the crystalline phases of PE in the temperature range from 10 to 450 K at zero pressure by means of a series of Monte Carlo simulations of the crystalline phases of PE. They used a full atomistic force field with flexible valence bonds and angles where the hydrogen atoms are explicitly treated. The simulations were carried out in the  $NpT$  ensemble, the pressure components in each direction  $x$ ,  $y$  and  $z$  of the system were controlled by scaling the box lengths and particle positions. Additionally, the use of infinite chains was introduced; the ends of each chain were artificially eliminated by connecting the chain ends through the periodic boundary conditions of the simulation box. The length of the chains of the studied systems was 12 and 96 for the smallest and largest system, respectively. In all cases the “herringbone”

<sup>§</sup> Angle between the  $xy$  projection of a C-C bond and the  $a$ -axis.

arrangement of the chains was stable, even at 450 K, which is higher than the experimental melting temperature of crystalline PE  $T_m=414$  K. The stabilization of crystalline phases of polyethylene above its melting temperature was attributed to the use of periodic boundaries and semi-infinite chains in the simulation

Martoňák *et al.* observed that at temperatures above 250 K, the lattice parameters  $a$  and  $b$  experience a linear increase with temperature, and that the quotient  $a/b$  increases from 1.44 slowly at first at low temperature and then, near 350 K, abruptly increases until it reaches a value of 1.73. The increase of the ratio  $a/b$  is due to the fast increase of  $a$ , whereas  $b$  grows slowly until reaching a maximum at 350 K and then decreases at higher temperatures. Around 500 K the crystal showed a hexagonal structure, where each chain was surrounded by six chains and the quotient  $a/b$  was close to the theoretical value 1.73.

In a more recent study the MC simulation results of Martoňák *et al.* of the structural and elastic properties of crystalline PE were compared against the predictions of a self-consistent quasi-harmonic lattice dynamics approach<sup>59</sup>. Both approaches were compared in their classic and quantum version. At temperatures below 2/3 of the melting temperature of polyethylene  $T_m \sim 250$  K, both approaches yield results consistent with the empirical force model used. The model was hybrid, with valence terms similar to the ones used by Karasawa *et al.*<sup>60</sup>, but parameterized to emulate the model of Sorensen *et al.*<sup>61</sup>. Quantum effects were important for temperatures lower than 300 K. Above this temperature anharmonic effects become important.

Ryckaert and Klein<sup>62</sup> performed molecular dynamics simulations with a full atoms model for temperatures between 100 and 400 K to study the effect of the temperature on the inter-chain packing of  $n$ -alkanes in solid phase. Systems of semi-infinite chains, composed by 16 carbon atoms each, initially centered on an orthorhombic structure, were simulated in  $NpT$  and  $NpH$  ensembles. The orthorhombic structure was stable up to about 325 K. Nevertheless, at 375 K the character of the solid changed; liquid-like diffusion occurred along the orientation of the chains. No transition from the orthorhombic to the hexagonal phase was observed even at 400 K.

Later Ryckaert *et al.*<sup>63,64</sup> performed molecular dynamics simulations in order to characterize the structure and dynamics of the solid phases of bi-layers of  $n$ -alkane tricosane ( $C_{23}H_{48}$ ). The simulations were made in the  $NpT$  ensemble at zero pressure using the Parrinello-Rahman method<sup>65</sup>. The intramolecular component of the used model consists of three terms a bond term, bending and torsion terms. Intermolecular

interactions between methyl groups were represented with by an exp-6 function. In the crystalline orthorhombic phase at 311 K translational, rotational and torsion motions of chains were detected, but all chains remained in a *trans* configuration in a herringbone arrangement. In contrast to the orthorhombic phase, a notable increase of longitudinal motions and *gauche* defects was detected in the pseudo-hexagonal rotator phase at 315 K, where each chain exhibits four well-defined orientations. The *gauche* defects concentrate mainly at the end groups of the chains.

Mavrantza *et al.*<sup>57</sup> performed molecular dynamics simulations in  $NpT$  ensemble to investigate the configurational and structural properties of the orthorhombic phase of PE and odd-numbered paraffins in the temperature range from 100 K to 298 K. The results corroborated previous experimental and simulation information about the herringbone arrangement of the chains and the crystalline phases of PE in the range of temperature studied. Below 273 K a little amount of *gauche* defects (< 0.01 %) was detected in the crystal of finite chains  $C_{23}H_{48}$ , while at higher temperature the concentration of defects experimented a notably increase. Any *gauche* defects were observed below 300 K for the PE crystal of semi-infinite chains.

### 1.2.3 Glass Transition in Polymers

The glass state is characteristic of systems that contain long chains or systems that form temporary or permanent networks, metallic alloys and polymer melts are some examples of them. When such a system, glass-former, is cooled down enough fast below its melting temperature,  $T_m$ , its dynamics becomes so slow that the system cannot reach the lower energy crystalline structure. Thus, the system conserves the disordered structure of the liquid when solidifies and forms a glass<sup>66</sup>.

The glass phase is sometimes considered a permanent non-equilibrium state of higher volume and enthalpy with respect to the crystalline structure at the same temperature.

In contrast to systems which crystallize, the density of glass-formers evolves continuously at the melting temperature. This behavior is related to the similarity of the glass structure and the structure of the liquid. The Figure 1.7 shows the typical thermal behavior of the density of a glass-former and of a system that crystallises. When a system is slowly cooled down from the liquid state its density continuously increases. Near the melting temperature the density experiences a sharp increase, because the

atoms/molecules of the system are reordered in a crystalline structure, the latter evolution of the system corresponds to the cooling of a crystal. Glass-formers exhibit a different thermal behavior under cooling: Below the melting temperature they tend to remain in liquid state. The undercooled liquid solidifies when the glass transition temperature is reached. At this point the thermal expansion coefficient changes, but the density continuously increases.

A simple method to detect the glass transition is through the change of the thermal expansion coefficient<sup>67-70</sup>. The point where the density lines of the glass and liquid states intersect determines  $T_g$  (Fig. 1.7).

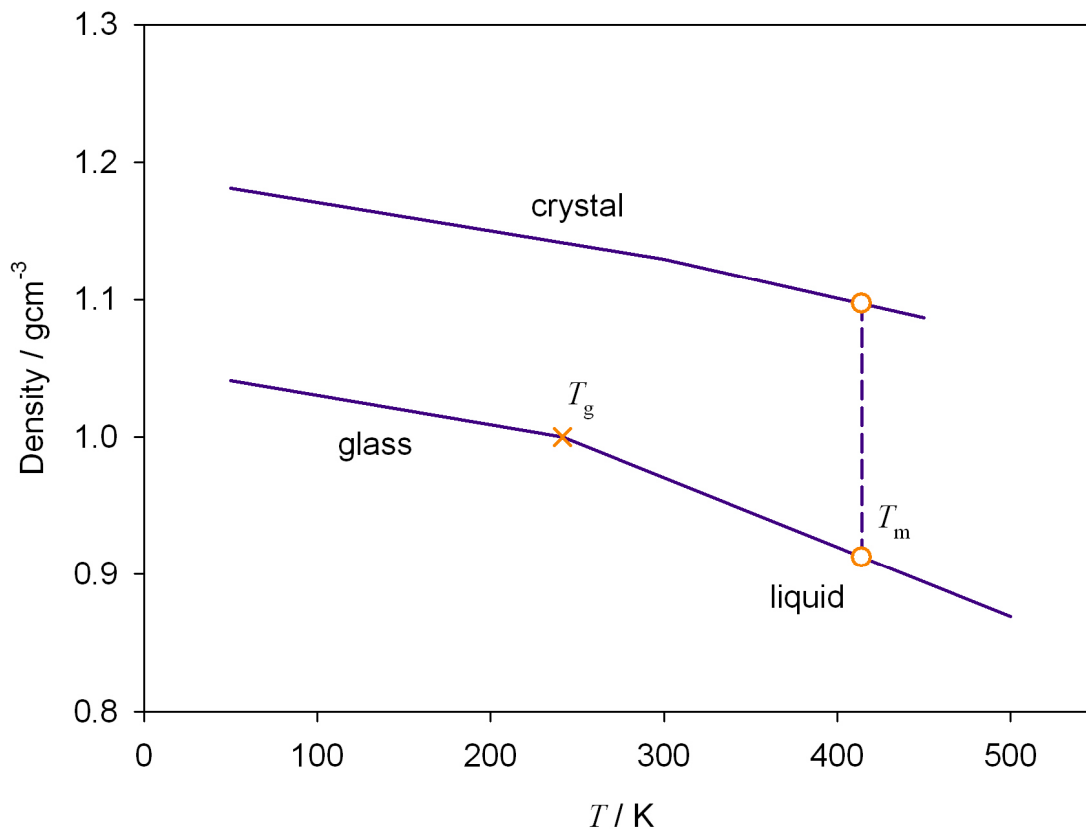


Figure 1.7. Density-temperature phase diagram of UAM model for polyethylene. The liquid glass line was calculated here by  $NpT$  simulations of  $C_{70}$  linear chains at  $p=0$  starting from a disordered initial configuration at  $T=450$  K, the system is equilibrated at each temperature and cooled down at relative high cooling rate. The line correspondent to the crystalline state was obtained by simulations of semi-infinite chains starting from an ordered state. The melting temperature indicated by dashed line corresponds to an experimental value of polyethylene.

The changes in self-diffusion coefficient and in the heat capacity are also good indicators of the glass transition<sup>33</sup>. The frequency of *trans-gauche* conformational transitions is another property of the system which sensible changes at the glass transition. Conformation changes in linear polymers can be monitored in a simulation



through the calculation of the averaged end-to-end distance of the chains; as the liquid is cooled down it increases until reaching a plateau in the vitreous zone<sup>71</sup>.

An interesting characteristic of the vitreous state is the dependence of the properties of the system to the production history, for example, to the cooling rate and/or the compression rate. The history-dependence of the properties of glass-formers can be qualitatively explained as follows; when a system is cooled at constant rate  $\nu$  along the cooling curve  $T = T_0 - \nu t$  it will take a time  $\Delta t = \Delta T \nu^{-1}$  in visiting each temperature. Above the glass transition temperature this time interval is enough so that the system reaches the equilibrium at each visited temperature due to the short relaxation time of a liquid;  $\tau(T) < \Delta T \nu^{-1}$ . However, near the glass transition temperature the dynamics of the system slows down and then the relaxation time increases  $\tau(T_g) \approx \Delta T \nu^{-1}$ . At a given temperature the time of relaxation of the system and the interval of simulation are comparable, further cooling takes the system to non-equilibrium states<sup>72</sup>. This fact leads to another of the definitions of the glass transition temperature<sup>33</sup>: as the temperature where the relaxation times of the system are of the order of  $10^2$  to  $10^3$  s.

Microscopically, polymers tend to form glasses. The structural nature of polymer glasses, their entangled chain arrangement and packing, hinder an adequate sampling of the phase space. They show a non-ergodic behavior. Their relaxation on longer time intervals is possible due thermal motions in regions of lower packing and higher mobility.

The dependence of the vitreous transition temperature on the cooling rate can be deduced from the empirical Vogel-Fulcher-Tammann<sup>68</sup> (VFT) equation

$$\tau(T) = A \exp\left(\frac{B}{T - T_0}\right). \quad (1.29)$$

It relates the relaxation time of a system to the temperature. From this equation an expression for the glass transition temperature is obtained upon considering that the relaxation time of the system and the simulation time interval become comparable at this point  $\tau(T_g) = \Delta T \nu^{-1}$

$$T_g = T_0 - \frac{B}{\ln(C\nu)}. \quad (1.30)$$

This equation relates the glass transition temperature  $T_g$  to the cooling rate  $\nu$  and indicates that the vitreous transition temperature is not a constant property for a given system; it depends on the cooling rate at which the transition is reached. Then, it is fundamental to associate the glass transition of a system with the time scale of the experiment. The ability of molecular simulations to predict this transition is debatable because of the difference between the time scales involved in experiments and simulations.

The glass transition in polymers is also sensible to the confinement. Experiments and simulations in polymer films indicate a reduction of the vitreous transition temperature with respect to the value in the bulk phase. Simulations of films between walls using different interaction models have demonstrated the dependence of the transition temperature on the interactions with the substrate. Böhme and de Pablo<sup>47</sup> simulated polymer films composed of 16 unit-chains using a square-well model to describe the interaction between units in a same chain and between units on different chains. Three different conditions were studied; self-supported films, films between repulsive walls and films between attractive walls. In the study they detected that the properties of a film can be different to the properties in bulk phase depending on the interactions between the polymer film and the substrate.  $T_g$  is lower for self-supported films and for films between repulsive walls, while an opposite behavior is obtained for the films between attractive walls. Similar conclusions were obtained with the hard-sphere model proposed by Rapaport<sup>45</sup>. Varnik *et al.*<sup>37,72</sup> repeated this study using a LJ-FENE potential and concluded that the reduction of  $T_g$  in confined geometries is due to an acceleration of the dynamics of the system.

De Gennes<sup>73</sup> proposed a tentative explanation for the drop of the glass transition temperature of thin polymer films. The model is based on the competition of two melting mechanisms. Each mechanism is associated to a type of motion a) standard motions, controlled by the free volume and b) collective motions along a chain, which require a smaller free volume (except for the end groups). For bulk systems, the standard motion wins, but for thin films the dominant process is the collective motion of a loop which not involves the chain ends. Within this model the glass transition temperature  $T_g$  depends linearly on the thickness of the film  $l$ . The proportionality constant,  $m_l$ , is a function of the molecular weight of the polymer  $M$ .

$$T_g = T_{g\infty} + m_l(l - l_0). \quad (1.31)$$

When the film thickness is lower than a certain value  $l_0$  the vitreous transition temperature decreases linearly with the film thickness. The parameters  $l_0$  and  $m_l$  increases as  $M^{1/2}$  when  $M < 2 \cdot 10^6$  and tends to saturate when  $M > M^*$ .



# Chapter 2

## Methods

The development of high performance computing has motivated in last years the use of molecular simulations methods as a straightforward and reliable way to study the properties of materials and complex phenomena at nano and micro scale<sup>74-79</sup>. Of particular interest in this work is the dynamics of condensation of a vapor phase in presence of a substrate.

Molecular simulation plays a valuable role in providing essentially exact results for problems in statistical mechanics<sup>80,81</sup>. The basic inputs of any molecular simulation are the interaction between particles and mass of particles. Statistical mechanics provide the link between microscopic information and the macroscopic quantities such as; transport coefficients, structure, equations of state, etc.

Experiments and theory are complemented by molecular simulations. Simulations are a useful tool to test the validity of an interaction model, to provide an interpretation of experimental information and can also be used to extrapolate the behavior of a system at extreme thermodynamics conditions<sup>75</sup>.

In the following sections the theoretical fundaments of molecular simulations here used are summarized, the implementation of molecular dynamics method in different ensembles is detailed and the techniques used in this work to optimize the code are briefly described.

## 2.1 Molecular Dynamics

Molecular dynamics (MD) and Monte Carlo (MC) simulations are the most widely used methods for the prediction of the properties of materials. The Monte Carlo method is based on the generation of random configurations which are accepted or rejected according to a given criterion. In the original version of the MC method developed by Metropolis (1959) a new configuration  $k'$  is accepted if the change in potential energy of the transition between the configurations  $k$  and  $k'$ ,  $\Delta\mathcal{U}_{kk'}$ , is negative. If the energy change is positive a new configuration is accepted only if the transition probability is higher than a random number between 0 and 1, in other case a new configuration  $k'$  is generated and the process is repeated. The expression of the transition probability is given by the choice of a particular ensemble, for example, in the canonical ensemble is  $w_{kk'} = \exp(-\Delta\mathcal{U}_{kk'}/k_B T)$ . The trial configurations are usually obtained by displacing, exchanging, removing or adding particles. The MC method produces a set of configurations which belongs to the phase space of a particular thermodynamic ensemble This sequence does not strictly follows the time evolution of a system and therefore the MC method cannot be directly applied used to study its dynamics.

The method of molecular dynamics describes the evolution of a system of particles, atoms and/or molecules, by means of the solution of the equations of motion derived from the Lagrangian, or the corresponding Hamiltonian, functions<sup>74,75,81</sup>

$$\frac{d}{dt} \left( \frac{\partial \mathcal{L}}{\partial \dot{\mathbf{q}}_i} \right) - \frac{\partial \mathcal{L}}{\partial \mathbf{q}_i} = 0. \quad (2.1)$$

$\mathcal{L}$  denotes the Lagrange function and  $\mathbf{q}_i$  generalized coordinates.

When any kind of temperature or pressure control is applied, the Lagrange function is equal to the difference between the kinetic and the potential energy of the system

$$\mathcal{L} = \mathcal{K} - \mathcal{U}. \quad (2.2)$$

The kinetic energy of a system of particles can be expressed in Cartesian coordinates,  $\mathbf{q}_i = \mathbf{r}_i$ , in terms of their momentum  $\mathbf{p}_i$

$$\mathcal{K} = \sum_{i=1}^N \frac{\mathbf{p}_i^2}{2m_i}. \quad (2.3)$$

$m_i$  is the mass of the particle  $i$ . The potential energy can be expressed as an infinite sum of functions of the relative positions of the particles  $\mathbf{r}_i$ ; external fields  $U_i$ , pair potentials  $U_{ij}$ , three-body potentials  $U_{ijk}$ , etc.

$$\mathcal{U} = \sum_i^N U_i(\mathbf{r}_i) + \sum_i^N \sum_{j>i}^N U_{ij}(\mathbf{r}_i, \mathbf{r}_j) + \sum_i^N \sum_{j>i}^N \sum_{k>j>i}^N U_{ijk}(\mathbf{r}_i, \mathbf{r}_j, \mathbf{r}_k) + \dots \quad (2.4)$$

Pairwise interactions are the most important contribution to the potential energy. Many systems, such as inert gases and gases at low pressure, are usually well described by a truncation of this expansion after the second term. A common compromise is to use an effective pair potential where all effects of spherically averaged many-body interactions are included. For other systems such as metals and covalent systems as carbon and silicon the use of pair potentials is not satisfactory because the cohesive energy of a pair strongly depends on the configuration of its surrounding atoms<sup>76</sup>.

The equations of motion are obtained by inserting the expressions for the kinetic and potential energy, Equations (2.3) and (2.4), in the Lagrange equations. Since the kinetic energy does not explicitly depend on the positions of the particles

$$\dot{\mathbf{p}}_i = -\nabla_{\mathbf{r}_i} \mathcal{U}. \quad (2.5)$$

Within the Lagrange formalism the momentum is defined by the relation

$$\mathbf{p}_i = \frac{\partial \mathcal{L}}{\partial \mathbf{q}_i} = m_i \dot{\mathbf{r}}_i. \quad (2.6)$$

The equations of motion associated to the Lagrange functions, obtained by differentiating both sides of the Equation (2.5), are equivalent to the Newton's second law; the acceleration of a particle is proportional to the total external force applied on it. The force, time derivative of the momentum, is calculated in the method from a potential model; it is equal to minus the gradient of the potential energy of the system at the position of the particle  $i$ .

$$m_i \ddot{\mathbf{r}}_i = \mathbf{F}_i \equiv -\nabla_{\mathbf{r}_i} \mathcal{U}. \quad (2.7)$$

The Hamiltonian of the system, defined by (2.8), is another interesting characteristic of the system since it is a conserved quantity, *i.e.* it remains constant while the system evolves (2.9)

$$\mathcal{H} = \sum_i \dot{\mathbf{q}}_i \mathbf{p}_i - \mathcal{L} \quad (2.8)$$

$$\frac{\partial \mathcal{H}}{\partial t} = \sum_i \left( \nabla_{\mathbf{q}_i} \mathcal{H} \right) \dot{\mathbf{q}}_i + \left( \nabla_{\mathbf{p}_i} \mathcal{H} \right) \dot{\mathbf{p}}_i = \sum_i \nabla_{\mathbf{q}_i} \mathcal{H} \nabla_{\mathbf{p}_i} \mathcal{H} - \nabla_{\mathbf{p}_i} \mathcal{H} \nabla_{\mathbf{q}_i} \mathcal{H}_i = 0. \quad (2.9)$$

The Hamiltonian associated to the Lagrangian (2.2) is equal to the sum of the kinetic and the potential energy of the system

$$\mathcal{H} = \mathcal{K} + \mathcal{U}. \quad (2.10)$$

Equations (2.7) can be equivalently deduced from Hamiltonian function as

$$\dot{\mathbf{q}}_i = \nabla_{\mathbf{p}_i} \mathcal{H} \quad \text{and} \quad \dot{\mathbf{p}}_i = -\nabla_{\mathbf{q}_i} \mathcal{H}. \quad (2.11)$$

From Equations (2.9) and (2.10) can be concluded that the sequence of configurations generated by the solution of the Equations (2.7) have the same total energy; they belong to the microcanonical ensemble *NVE*.

The classical equations of motion, Equation (2.7), are known to be good approximations to the Schrödinger equation for many systems. However, their application should be questioned in systems where the thermal wavelength and the characteristic length of interaction are comparable. Quantum effects are important in light atoms, such as hydrogen and helium, at low and moderate temperatures<sup>78</sup>.

### 2.1.1 Integration Algorithm

In molecular dynamics the temporal evolution of a system of interacting particles is followed by the integration of a system of coupled non-linear second order ordinary differential equations. The problem is numerically solved by a discretization of the temporal derivatives which appear in the equations of motion.



In the Störmer-Verlet method<sup>76</sup> velocity and the acceleration are approximated with central difference operators

$$\dot{\mathbf{r}}_i^n = \frac{\mathbf{r}_i^{n+1} - \mathbf{r}_i^{n-1}}{2\Delta t} \quad (2.12)$$

$$\mathbf{r}_i^n = \frac{\mathbf{r}_i^{n+1} - 2\mathbf{r}_i^n + \mathbf{r}_i^{n-1}}{\Delta t^2}. \quad (2.13)$$

The notation  $\mathbf{x}(n\Delta t) = \mathbf{x}(t_n) = \mathbf{x}^n$  is used. A formula for the calculation of the new positions is obtained by replacing the expression of the acceleration (2.13) into the motion Equation (2.7) and using (2.12) to eliminate  $\mathbf{r}_i^{n-1}$

$$\mathbf{r}_i^{n+1} = \mathbf{r}_i^n + \dot{\mathbf{r}}_i^n \Delta t + \frac{\mathbf{F}_i^n \Delta t^2}{2m_i}. \quad (2.14)$$

To calculate the velocity at  $t_n$ , (2.14) is replaced in the difference operator (2.12)

$$\dot{\mathbf{r}}_i^n = \frac{\mathbf{r}_i^n - \mathbf{r}_i^{n-1}}{2\Delta t} + \frac{\mathbf{F}_i^n}{2m_i} \Delta t. \quad (2.15)$$

In order to obtain an expression for the new velocities, the index  $n$  is replaced by  $n+1$  in (2.15) and the resulting expression is added to (2.15)

$$\mathbf{r}_i^{n+1} = \dot{\mathbf{r}}_i^n + \frac{(\mathbf{F}_i^n + \mathbf{F}_i^{n+1})}{2m_i} \Delta t. \quad (2.16)$$

This simple version of the Störmer-Verlet algorithm shows advantages with respect to other direct integration methods as Leapfrog, since it increases the integration order with a computational effort comparable to simple methods. For the integration step a value of about  $0.005\tau$  is recommended<sup>74,75</sup>, where  $\tau$  is the shortest characteristic time of the system<sup>77</sup>. Here an integration step  $\Delta t = 1$  fs is used.

Equations of motion (2.7), or the corresponding equations to the chosen ensemble, are propagated starting from an initial configuration; particle positions and velocities are usually specified as initial values.

## 2.1.2 Definition of Thermodynamic Properties

Molecular dynamics provide detailed information about a system; positions and velocities of each particle at different times. This large amount of data is then translated to macroscopic observable quantities, as temperature and pressure, through statistical mechanics expressions.

A total number of  $6N$  coordinates, for example, the set of particle positions and velocities, represents a point of the phase space  $\Gamma = \{\mathbf{p}, \mathbf{q}\}$ <sup>74,75</sup>. The phase space is sampled, as in Monte Carlo methods, from the density of states of the ensemble or equivalently, as in molecular dynamics, from the solution of the corresponding equations of motion. In the latter case, the system evolves from an initial non-equilibrium state to a stationary one.

Particle velocities and positions, specified at the beginning of a simulation, define a value of the total energy and how far a system is away from equilibrium. As common practice, particles are placed on a lattice to prevent overlapping configurations of high repulsive energy while velocities are assigned according to a Boltzmann distribution at a specified temperature.

Macroscopic observable properties  $\langle \mathcal{X} \rangle$  are defined as averages of their instantaneous values made over different samples of a particular ensemble

$$\langle \mathcal{X} \rangle = \sum_{\Gamma} \mathcal{X}(\Gamma) \rho(\Gamma) = \frac{1}{t'} \sum_{i=1}^{t'} \mathcal{X}_i . \quad (2.17)$$

According to the virial theorem, written in its equipartition principle form, temperature and pressure are given by the averages<sup>77</sup>

$$\text{a) } \langle \mathbf{p}_j \nabla_{\mathbf{p}_k} \mathcal{H} \rangle = \delta_{jk} k_B T \quad \text{and} \quad \text{b) } \langle \mathbf{q}_j \nabla_{\mathbf{q}_k} \mathcal{H} \rangle = \delta_{jk} k_B T . \quad (2.18)$$

The following expression for the temperature is obtained by writing the expression (2.18a) for  $j = k$  in Cartesian coordinates

$$T = \frac{1}{dNk_B} \left\langle \sum_i \frac{\mathbf{p}_i^2}{m_i} \right\rangle . \quad (2.19)$$

Where  $d$  is the dimension of the system, for example,  $d = 3$  for a three-dimensional system. The brackets denote a temporal average performed in the production stage of a simulation, which is time interval where the properties reach a stationary behavior. From (2.18) the following expression for the pressure is deduced

$$p = \frac{1}{dV} \left\langle \sum_i \frac{\mathbf{p}_i^2}{m_i} + \sum_i \sum_{j>i} \mathbf{r}_{ij} \cdot \mathbf{F}_{ij} \right\rangle. \quad (2.20)$$

Kinetic and configurational contributions can be recognized in this expression.  $\mathbf{r}_{ij}$  and  $\mathbf{F}_{ij}$  are the distance and force, respectively, between a pair  $ij$ .

According to the ergodic hypothesis, long simulation time intervals assure the convergence to equilibrium. The equilibrium properties of a large system do not depend on the initial conditions when the phase space is effectively explored. According to the Gibbs phase rule it means for a one-component system that identical values of the properties are reached in stationary state when simulations start from different configurations of equal total energy and global density. Some systems as condensed phases in practice represent an exception to the ergodic assumption, because they are often being ‘trapped’ in metastable states. Some sample preparation techniques, as annealing at high temperature, can remediate those situations. Other cases, as glass-formers, show an inherently history-dependent behavior.

### 2.1.3 Cut-off Radius Approximation

The amount of valence terms grows in proportion to the number of bonded pairs and sequences of three and four atoms/groups. Its calculation requirement is of order  $N$ . However, the calculation of non-bonded interactions grows in proportion to the total number of pairs  $N^2$  and represents the bottle-neck of a simulation.

The repulsive and attractive contributions of the Lennard Jones potential rapidly decrease at larger distances. The interactions between neighboring particles which are closer than some cut-off distance  $r_c$  dominate in the whole potential energy of the system. As an approximation the potential is truncated

$$U_{ij} \begin{cases} U_{ij}(r), & r \leq r_c \\ 0 & , r > r_c. \end{cases} \quad (2.21)$$

Interactions between particles separated by a distance larger than a given cut-off are neglected. Values of  $r_c$  in the range from  $2.5\sigma$  to  $5.0\sigma$  are typically used. In homogeneous systems the amount of pair interactions to be calculated are proportional to the volume of the sphere defined by the used cut-off radius

$$N^{\text{nb}} \approx \frac{N(N-1)}{2} \frac{V(r_c)}{V}. \quad (2.22)$$

This amount of pairs is remarkably lower in comparison to  $N(N-1)/2$  in large systems, where  $V(r_c) < V$ .

Tail corrections on quantities such as the pressure, interfacial and potential energies can be applied after the simulation to take into account the mean effect of pair interactions beyond the cut-off distance. The radial distribution function  $g(r)$  is a useful quantity for this purpose, because it defines for a particle the probability density to find another one at a given distance  $r$

$$\rho g(r) = \frac{1}{N} \sum_i \sum_{j \neq i} \delta(r - r_{ij}). \quad (2.23)$$

For pair potential the expressions of tail corrections can be obtained by integrating the virial contribution of the pairs separated by a distance higher than the cut-off radius, over the volume outside the cut-off sphere, using the radial distribution function as weight factor. In particular, the tail correction for the pressure is given by<sup>75</sup>

$$p_c = 2\pi\rho^2 \int_{r_c}^{\infty} dr g(r) r^2 \mathbf{r} \cdot \mathbf{F}^{\text{nb}}(r). \quad (2.24)$$

$\mathbf{F}^{\text{nb}}$  denotes the non-bonded forces. For potentials with spherical symmetry the integral (2.24) can be explicitly solved assuming that the probability to find a particle beyond the cut-off radius is constant,  $g(r)=1$ . For the 12-6 Lennard Jones potential the integrated expression is

$$p_c(r_c) = \frac{16\pi}{3} \rho^2 \varepsilon \sigma^3 \left[ \frac{2}{3} \left( \frac{\sigma}{r_c} \right)^9 - \left( \frac{\sigma}{r_c} \right)^3 \right]. \quad (2.25)$$

This assumption is valid for enough large values of  $r_c$ .  $\rho=N/V$  is in (2.25) the number density. The integral (2.24) converges for potentials which decrease faster than  $r^{-d}$ , such as dispersion interactions, where  $d$  is the dimensionality of the system.

#### 2.1.4 Neighbor lists

The recognition of the neighbors of a particle, defined by the cut-off radius, requires the calculation of the distances between all possible pairs at each integration step; this calculation is, as the calculation of non-bonded forces, also of order  $N^2$ . In order to avoid this step neighbor lists are used<sup>74-78</sup>. The method involves the construction of a list of neighbors for each particle within a distance smaller than a given threshold  $r_1$ , called Verlet radius, which is chosen larger than the cut-off distance and smaller than the half of the smaller box length. In each integration step only distances between neighboring particles and forces between neighbors which are at a distance minor than the cut-off radius are calculated. The positions of particles are stored in a vector  $r_0$  whenever the list is updated. If the displacement of a particle respect to its old position, stored in  $r_0$ , exceeds a given value  $r_{\max}$ , the list is updated. The value of the threshold  $r_{\max}$  corresponds to the minimum displacement that could cause that a particle, which does not belong to the actual Verlet list, enters into the cut-off sphere of another particle (see Appendix A.1). Verlet lists reduce the amount of distance computations approximately to a fraction  $4\pi r_1^3 \rho / (3N)$ .

The calculation of displacements is of order  $N$ , while updating the list is a step of order  $N^2$ . Upon increasing the Verlet radius the amount of particles inside the Verlet sphere as the amount of pair distances to be calculated increase, however, the update frequency of the list decreases. The size of the Verlet radius can be optimized for particular cases. For example, in solids the neighborhood of a particle does not change over long intervals of time, thus smaller values of the Verlet radius are preferred. In the simulations here a value  $r_1 = r_c + \sigma$  is used for gas phases and  $r_1 = r_c + 0.6\sigma$  for solid phases.

### 2.1.5 Periodic Boundaries and Minimum Image Convention

Many simulations deal with a small number of particles, in comparison to the number of atoms/molecules in a little macroscopic volume. As result the surface effects dominate when a simulation is made in a confined region of space, *i.e.* by the use of hard reflecting walls, since many of the particles in the system are found near the boundaries of the sample. Under these conditions the system size would have to be extremely large to ensure that the surface has only a small influence on the bulk properties, but such system would be too large to simulate.

In simulations surface effects can be avoided by the use of periodic boundary conditions. The simulation box is replicated throughout space in an infinite lattice; when a particle moves in the central box its displacement is replicated in the copies. The central box constitutes a convenient reference system for measuring locations of the  $N$  molecules. When a molecule leaves the central box one of its images enters through the opposite face, the boundaries are permeable but the number of particles remains constant. The implementation of periodic boundaries is simple; a transformation of coordinates is applied on all particles in each direction where periodic boundaries are imposed after an integration step

$$\mathbf{r}_i^\alpha \leftarrow \mathbf{r}_i^\alpha - L^\alpha \text{anint}(\mathbf{r}_i^\alpha / L^\alpha). \quad (2.26)$$

In planar systems, such as the films here studied, periodic boundaries are used on the transversal directions of the film to emulate an infinite slab. The resulting system represents a film of finite thickness and infinite area.

The interaction of a particle  $i$  is calculated beyond the periodic boundaries with the nearest periodic images of any other particles  $j$ . A special definition of the distances denominated Minimum Image Convention<sup>74-78</sup> is used; the distances between particles are calculated as the minimum among them considering the original box and its copies

$$\mathbf{r}_{ij}^\alpha \leftarrow \mathbf{r}_{ij}^\alpha - L^\alpha \text{anint}(\mathbf{r}_{ij}^\alpha / L^\alpha). \quad (2.27)$$

The potential is normally truncated at a distance smaller than half of the shortest box length and thus the calculation of the interaction between a molecule and its own image is avoided. The simple cut-off is always applicable to short-range interactions as

Lennard Jones potential, whose attractive term decays as  $r^{-6}$ . For long range interactions, as the Coulomb potential, other methods as the Ewald sum are usually employed<sup>75-77</sup>.

### 2.1.6 Control of Temperature and/or Pressure

Newton's equations describe the evolution of an isolated system, a sequence of states which conserve the total energy, the particle number and the global density of the initial configuration. Quantities as the kinetic energy, potential energy, temperature and pressure as well as all other variables change during the simulation, while the system converges to equilibrium. It is difficult to establish the final value of the temperature and/or pressure from a simulation in a microcanonical  $NVE$  ensemble. For this reason some methods to control these variables are introduced.

Phase transitions and the evolution of a system to a stationary state are in general accompanied by heat exchange. In the case of the condensation of a vapor phase, when two or more particles approximate to build a cluster of the new phase, the temperature locally increases because of the conversion of potential energy into kinetic energy. The simulation of phase transitions phenomena in microcanonical ensemble  $NVE$  is not adequate, the reversible transformation of the kinetic and potential energy promote a continuous phase change in both directions. The heat produced by the condensation must be removed from the system by an external agent; a heat bath is coupled to the system for this purpose. The heat flow exchanged by the system and the thermostat in one integration step is given by  $J_T = \Delta Q / \Delta t$ , where  $\Delta Q$  is the heat exchange in a time interval  $\Delta t$ . Heat is incorporated into the system through the modification of the kinetic energy,  $\Delta Q = \Delta K$ , then

$$J_T = \frac{1}{2\Delta t} \sum_i m_i \mathbf{r}_i^2 (\lambda^2 - 1) = \frac{3Nk_B T_B (\lambda^2 - 1)}{2\Delta t}. \quad (2.28)$$

$T_B$  is here the reference temperature of the thermostat. The simplest method to perform a simulation at constant temperature involves the scaling of the velocities<sup>74-78</sup> of all particles at each integration step by a factor equal to

$$\lambda = \sqrt{T_B / T}. \quad (2.29)$$

The kinetic energy is increased by the thermostat when the temperature of the system is lower than the reference temperature and vice versa. The instantaneous resulting temperature is equal to the reference temperature during the simulation, in other words, the temperature fluctuations produced by this method are zero. On the other hand, the method does not assure the conservation of momentum. Therefore the simple scaling of velocities does not reproduce the canonical ensemble  $NVT$ , but another one, called isokinetic.

The Berendsen thermostat<sup>82</sup> is an extension of the homogeneous scaling of velocities; the coupling strength can be regulated by a relaxation parameter. Velocities are multiplied in each step by the scaling factor

$$\lambda = \sqrt{1 + \frac{\Delta t}{\tau_T} \left( \frac{T_B}{T} - 1 \right)}. \quad (2.30)$$

The parameter  $\tau$  can be specified in the range  $[\Delta t, \infty[$ ;  $\tau_T = \Delta t$  corresponds to the strongest coupling and is equivalent to the simple scaling method, the other extreme  $\tau_T \rightarrow \infty$  corresponds to a simulation without control of temperature, so that Newton's equations are recovered.

In contrast to the simple scaling, where the temperature remains constant during the simulation, the temperature in the Berendsen method exhibits a negative exponential response to external perturbations

$$\delta T = \delta T_0 \exp(-t / \tau_T). \quad (2.31)$$

The scaling methods are simple to implement but produce some undesired effects. One of them is the transformation of the kinetic energy of high frequency modes as bond stretching and angle bending into low frequency ones. The equipartition of energy is violated. However, because of their fast response they can be employed to produce an initial configuration.

Nosé-Hoover<sup>83,84</sup> proposed another method to control the temperature in a simulation; it is based on the modification of the Lagrangian of the system to incorporate a heat bath. The fundamental difference between the Nosé-Hoover thermostat and velocity scaling methods is that the velocities are not directly modified



but the balance of momentum. An additional contribution appears in the equations of motion

$$\dot{\mathbf{p}}_i = \mathbf{F}_i - \zeta \mathbf{p}_i \quad (2.32)$$

$$\dot{\zeta} = g k_B Q^{-1} (T - T_B). \quad (2.33)$$

The new term  $-\zeta \mathbf{p}_i$  in (2.32) can be interpreted as a friction force, with  $\zeta$  a friction factor. The mass parameter  $Q$  regulates the coupling to the thermostat. The Nosé-Hoover equations, derived from the modified Lagrangian, reproduce the canonical ensemble.

An alternative to the deterministic thermostats previously described are the stochastic methods, one of which is the Andersen thermostat<sup>85</sup>. The temperature is controlled by stochastic collisions. The velocity of a randomly chosen particle is reassigned according to a Maxwell-Boltzmann distribution at the temperature of the heat bath. As in a natural system the time intervals between two collisions are distributed by a Poisson function, the coupling to the thermostat is adjusted by the frequency parameter of the distribution.

The direct application of a thermostat to control the temperature of a metastable vapor in a simulation of condensation phenomena is not recommendable. A condensing vapor has high local temperature gradients because of the heat generated by the clustering process, in some systems when the global temperature is controlled by the coupling of a thermostat the temperature of the monomers experiences an unphysical decrease. As consequence, the dynamics of the transition is artificially affected by the thermostat. This undesired effect becomes more important as the cohesive energy of the simulated system increases. As example, during the simulation of condensation of vapors of noble gases this effect is not important, but in condensing metals it can lead to the immobilization of the monomers in the gas phase.

A natural way to simulate the condensation of vapors at a controlled temperature is by means of the addition of a carrier gas to the system<sup>87-90</sup>. The heat produced in the vapor phase by the nucleation is extracted by the carrier gas by collisions. Simple methods, as the scaling of velocities, are usually applied to control the temperature of the carrier gas.

For the simulations of heterogeneous nucleation phenomena, here performed, the temperature of the condensing phase was indirectly controlled by applying a thermostat to the substrate. In particular, for the simulation of the condensation of Ar on polyethylene films a Nosé-Hoover thermostat was applied to the film, the heat produced by the condensation of Ar is removed by the film. The vapor phase is indirectly cooled down by the Ar atoms which reach the surface and reevaporate.

For the simulation of condensation of metals on polymer substrates the described method results inefficient to cool down the vapor phase, because many of the metal atoms deposited on the polymer substrate remain adsorbed on the surface or diffuse into the polymer matrix. Ar is incorporated to the system as carrier gas. The heat produced by the condensation of Pt is removed from the surface and from the vapor phase through the exchange of Ar atoms on the surface.

In the next sections the methods to control temperature and pressure implemented in the present simulations are described.

### 2.1.6.1 Nosé-Hoover Thermostat, $NVT$ Ensemble

Nosé<sup>83,84</sup> demonstrated that it is possible to perform a simulation in a canonical ensemble by means of the use of an extended Lagrangian function

$$\mathcal{L} = s^2 \sum_i \frac{m_i \dot{\mathbf{r}}_i^2}{2} - \mathcal{U}(\mathbf{r}^N) + \frac{Q}{2} \dot{s}^2 - g k_B T_B \ln(s). \quad (2.34)$$

$g$  is the number of degrees of freedom of the system,  $g = dN$ , where  $d$  is the dimension of the system,  $Q$  the mass parameter of the thermostat and  $s$  is the additional variable of the thermostat, the mechanism of the thermostat can be interpreted as a scaling of the time by a factor  $s$ . Within the Lagrange formalism the conjugate momenta are

$$\boldsymbol{\pi}_i = \frac{\partial \mathcal{L}}{\partial \dot{\mathbf{r}}_i} = m_i s^2 \dot{\mathbf{r}}_i \quad (2.35)$$

$$\pi_s = \frac{\partial \mathcal{L}}{\partial \dot{s}} = Q \dot{s}. \quad (2.36)$$

Then, the corresponding Hamiltonian for the Nosé Equation is

$$\mathcal{H} = \frac{1}{s^2} \sum_i \frac{\boldsymbol{\pi}_i^2}{2m_i} + \mathcal{U}(\mathbf{r}^N) + \frac{\pi_s^2}{2Q} + gk_B T_B \ln(s) \quad (2.37)$$

and the equations of motion derived from this function are

$$\dot{\mathbf{r}}_i = \frac{\boldsymbol{\pi}_i}{m_i s^2} \quad (2.38)$$

$$\boldsymbol{\pi}_i = \mathbf{F}_i \quad (2.39)$$

$$\pi_s = \frac{1}{s} \left( \sum_i \frac{\boldsymbol{\pi}_i^2}{m_i s^2} - gk_B T_B \right) \quad (2.40)$$

$$\dot{s} = \frac{\pi_s}{Q}. \quad (2.41)$$

Introducing the simplification of Hoover<sup>85</sup>,  $\xi = s^{-1}(\partial s / \partial t)$ , and writing the Equations (2.38) to (2.41) in real space, the following equations of motion are obtained:

$$\dot{\mathbf{r}}_i = \frac{\mathbf{p}_i}{m_i} \quad (2.42)$$

$$\dot{\mathbf{p}}_i = -\frac{\partial \mathcal{U}(\mathbf{r}^N)}{\partial \mathbf{r}_i} - \xi m_i \dot{\mathbf{r}}_i \quad (2.43)$$

$$\dot{\xi} = \frac{1}{Q} \left( \sum_i \frac{\mathbf{p}_i^2}{m_i} - gk_B T_B \right) \quad (2.44)$$

$$\dot{s} = \xi s. \quad (2.45)$$

The Equation (2.45) for  $s$  is not necessary for the computation of the trajectories of the particles, but it can be solved to check the energy conservation by means of the calculation of the temporal evolution of the Hamilton function (2.37).

The extended Lagrange function can be interpreted as the coupling of a heat bath to the original system. The last two contributions of the new Lagrangian introduce a friction term  $-\xi m_i \dot{\mathbf{r}}_i$  in the Equation (2.43).  $Q$  is the inertia of the heat bath, it fixes the

rate of energy transfer. Low values of this parameter lead to a fast response to perturbations and higher temperature fluctuations. The other extreme, high values of  $Q$ , decrease the amplitude of the fluctuations and slow the response of the thermostat, so that the heat transfer is not effective. The limiting condition  $Q \rightarrow \infty$  resembles the microcanonical ensemble  $NVE$ .

The parameter  $Q$  is chosen according to a condition of resonance between the oscillations of temperature introduced by the thermostat and some intrinsic frequency of the system. The following differential equation describes the harmonic behavior of the temperature near the thermal equilibrium<sup>77</sup>

$$\frac{d^2 \ln T}{dt^2} = \frac{2dNk_B}{Q}(T_B - T). \quad (2.46)$$

For small perturbations of the temperature of the system around the temperature of the heat bath,  $T=T_B+\delta T$ , the Equation (2.46) can be analytically solved by means of the linearization  $\ln(T_B + \delta T) \approx \ln(T_B) + \delta T / T_B$

$$\frac{d^2 \delta T}{dt^2} = -\frac{2dNk_B T_B}{Q} \delta T. \quad (2.47)$$

The solution of (2.47) describes the response of temperature for small perturbations

$$\delta T = \delta T_0 \sin\left[\left(2dNk_B T_B Q^{-1}\right)^{1/2} t + \chi_T\right]. \quad (2.48)$$

It is a periodic function of frequency given by  $w_T^2 = 2dNk_B T_B Q^{-1}$ . A criterion based on the resonance between the system and the coupled thermostat is used to establish the mass parameter  $Q$ . The frequency is equated to some intrinsic frequency  $w$  of the system  $w_T = w$ , thus  $Q = 2dNk_B T_B w^{-2}$ . For example, the frequency of a set of Lennard Jones centers in a lattice is approximately  $w = \tau_{LJ}^{-1} \approx (k_B T_B / m)^{1/2} \sigma^{-1}$ .

The velocity Verlet-Störmer method leads to the following recursive formulas to integrate the Nosé-Hoover equations<sup>76</sup>

$$\mathbf{r}_i^{n+1} = \mathbf{r}_i^n + \dot{\mathbf{r}}_i^n \left(1 - \xi^n \Delta t / 2\right) \Delta t + \frac{\mathbf{F}_i^n \Delta t^2}{2m_i} \quad (2.49)$$

$$\mathbf{r}_i^{n+1} = \frac{1}{1 + \xi^{n+1} \Delta t / 2} \left( \mathbf{r}_i^n \left( 1 - \xi^n \Delta t / 2 \right) + \frac{(\mathbf{F}_i^n + \mathbf{F}_i^{n+1}) \Delta t}{2m_i} \right). \quad (2.50)$$

The friction coefficient at  $t^{n+1}$  depends on the velocities at  $t^{n+1}$ , which are unknown. In order to avoid iterative calculations at this point the following first order approximation is recommended<sup>77</sup>

$$\xi^{n+1} \approx \xi^n + \dot{\xi}^n \Delta t = \xi^n + \frac{\Delta t}{Q} \left( \sum_i m_i (\dot{\mathbf{r}}_i^n)^2 - g k_B T_B \right). \quad (2.51)$$

### 2.1.6.2 Simultaneous Control of Temperature and Pressure, $NpT$ Ensemble

As an extension of Nosé-Hoover ideas, Andersen and Nosé showed that the  $NpT$  ensemble can be reproduced by a modification of the Lagrange of the system. The system is coupled simultaneously to a barostat and a thermostat by introducing the variables  $\xi = s^{-1}(\partial s / \partial t)$  and  $\eta = V^{-1}(\partial V / \partial t)$ . The Andersen-Nosé Hamiltonian is given by<sup>72,91</sup>

$$\mathcal{H} = \sum_i \frac{\mathbf{p}_i^2}{2m_i} + \mathcal{U}(\mathbf{r}^N) + \frac{1}{2} Q \xi^2 + \frac{1}{2} d M_\eta \eta^2 + p_{\text{ext}} V. \quad (2.52)$$

Here  $\eta$  is the strain rate and  $M_\eta$  is the mass parameter of the barostat. The corresponding equations of motion are

$$\dot{\mathbf{r}}_i = \frac{\mathbf{p}_i}{m_i} + \eta \mathbf{r}_i \quad (2.53)$$

$$\dot{\mathbf{p}}_i = \mathbf{F}_i - (\eta + \xi) \mathbf{p}_i \quad (2.54)$$

$$\dot{\xi} = \frac{1}{Q} \left( \sum_i \frac{\mathbf{p}_i^2}{m_i} - g k_B T_B \right) \quad (2.55)$$

$$\dot{\eta} = \frac{1}{M_\eta} (p - p_B) \quad (2.56)$$

$$\dot{V} = V \eta d. \quad (2.57)$$

The rate of change of  $\eta$  depends on the instantaneous pressure, which is governed by the virial expression (2.20). Hoover's equations of motion do not exactly reproduce the  $NpT$  ensemble. Melchionna<sup>92</sup> introduced an improvement of the Hoover's equations by the translation  $\mathbf{r}_i \leftarrow \mathbf{r}_i - \mathbf{r}_m$  in (2.53), where  $\mathbf{r}_m$  is the center of mass of the set of particles. The modified Equations (2.53) to (2.57) generate exactly the  $NpT$  probability distribution. The pressure is controlled by isotropic fluctuations of the volume. This method can be applied to isotropic homogeneous systems where the pressure is a scalar constant over the system.

### 2.1.6.3 Simultaneous Control of Temperature and Pressure in Films

The Nosé-Andersen iso-stress equations are only applicable to homogeneous systems. For inhomogeneous systems, the components of the pressure tensor depend on the position  $\mathbf{p} = \mathbf{p}(\mathbf{r})$ . In planar systems, such as films, the pressure tensor is diagonal in thermal equilibrium and has two independent components: tangential and normal. The conjugate variables of these components are the thickness  $l$  and the area  $A'$ , respectively. When a system is expanded in the transversal direction  $z$  at constant area  $A'$ , its energy change is given by

$$dE_N = -F_N \int_{-l/2}^{l/2} dz = -p_N A' dl. \quad (2.58)$$

The normal pressure is constant along the system. Tangential forces, however, change along the  $z$ -axis. Therefore, the change of energy of the system due to variations in the area at constant thickness is defined as

$$dE_T = - \int_{-l/2}^{l/2} F_T(z) dz = -dA' \int_{-l/2}^{l/2} p_T(z) dz = -\langle p_T \rangle l dA'. \quad (2.59)$$

Here the mean value of the tangential component of the pressure is defined by

$$\langle p_T \rangle = \frac{1}{l} \int_{-l/2}^{l/2} p_T(z) dz. \quad (2.60)$$

The total change of energy that the system experiences due to an arbitrary deformation is the sum of both terms

$$dE = dE_N + dE_T = \left( \frac{\partial E}{\partial l} \right)_{S,A'} dl + \left( \frac{\partial E}{\partial l} \right)_{S,l} dA' = -p_N A dl - \langle p_T \rangle l dA' \quad (2.61)$$

and the external thermodynamic forces are

$$\tilde{p}_N = - \left( \frac{\partial E}{\partial l} \right)_{S,A'} = p_N A', \quad \tilde{p}_{N,E} = p_{N,E} A' \quad (2.62)$$

and

$$\tilde{p}_T = - \left( \frac{\partial E}{\partial A'} \right)_{S,L} = \langle p_T \rangle l, \quad \tilde{p}_{T,E} = p_{T,E} l. \quad (2.63)$$

Therefore, to perform a simulation at constant normal external pressure, the area must be constant while the thickness changes. In the same way, a simulation at constant tangential pressure should be performed at constant thickness while the area of the system varies.

Varnik<sup>72</sup> developed an extension of the Nosé-Andersen equations for inhomogeneous cases by means of a generalization of the Hamiltonian (2.52)

$$\mathcal{H} = \sum_{\alpha} \left( \sum_i \frac{\mathbf{p}_{i,\alpha}^2}{2m_i} + \frac{1}{2} Q_{\alpha} \xi_{\alpha}^2 + \frac{1}{2} d_{\alpha} M_{\eta,\alpha} \eta_{\alpha}^2 + \tilde{p}_{\alpha} V_{\alpha} \right) + \mathcal{U}(\mathbf{r}^N) \quad (2.64)$$

The derivation of the equations of motion from this Hamiltonian function is, in analogy to the Hoover equations,

$$\dot{\mathbf{r}}_i^{\alpha} = \frac{\mathbf{p}_i^{\alpha}}{m_i} + \eta^{\alpha} (\mathbf{r}_i^{\alpha} - \mathbf{r}_m^{\alpha}) \quad (2.65)$$

$$\dot{\mathbf{p}}_i^{\alpha} = \mathbf{F}_i^{\alpha} - (\eta^{\alpha} + \xi^{\alpha}) \mathbf{p}_i^{\alpha} \quad (2.66)$$

$$\dot{\xi}^{\alpha} = \frac{1}{Q^{\alpha}} \left( \sum_i \frac{\mathbf{p}_i^{\alpha 2}}{m_i} - d^{\alpha} N k_B T_B \right) \quad (2.67)$$

$$\dot{\eta}^\alpha = \frac{1}{M_\eta^\alpha} (\tilde{p}^\alpha - \tilde{p}_B^\alpha) \quad (2.68)$$

$$V^\alpha = V^\alpha \eta^\alpha d^\alpha. \quad (2.69)$$

$\tilde{p}^\alpha$  is related to the instantaneous value of the pressure in the direction  $\alpha$ , defined as

$$\tilde{p}^\alpha = \frac{1}{d^\alpha V^\alpha} \left( \sum_i \frac{\mathbf{p}_i^{\alpha 2}}{m_i} + \sum_i \sum_{j>i} \mathbf{r}_{ij}^\alpha \cdot \mathbf{F}_{ij}^\alpha \right). \quad (2.70)$$

A planar system, like a film, with a surface oriented in the  $z$ -axis, has two independent directions; tangential and normal,  $d_T=2$  and  $d_N=1$ ,  $V_T=A'$  and  $V_N=l$ , where  $A'$  and  $l$  are respectively the area and the thickness of the film. Due to the use of periodic boundary conditions, distances and forces are calculated according the Minimum Image Convention.

## 2.2 Force Fields

Newton's equations of motion, or their isotherm/isobaric modifications, of a system of particles which interacts according to an empirical force field constitutes the basic machinery of the molecular dynamics.

Force fields are functions of the particle relative positions. Their parameters are determined for a set of training molecules by a minimization of the difference between calculated macroscopic properties and experimental data/quantum mechanic calculations, for example, evaporation and sublimation heats, crystallographic data and the energy difference between two conformations in a molecule<sup>77</sup>.

The parameterization of an interaction model is essentially a non-linear optimization problem which has multiple minima. It is difficult, or maybe impossible, to optimize simultaneously all the properties to the same degree of accuracy because of the empiric nature of the existent force fields. Usually, the parameters of a model are separately optimized using a selected group of properties. The development of force fields and their parameterization of a model is still an art since its reliability sensibly depends on the supposed mathematical form of the model and also on the right selection of parameters and properties used in the optimization.



In the following sections some models for the simulation of the systems here studied; noble gases, metals, and polymers are briefly described.

### 2.2.1 Potential Models of Noble Gases

London explained the strong deviations from the gas ideal behavior that some non-polar systems, as Ar atoms, show at moderate pressure. The oscillations of electrons around the nucleus of a molecule produce a temporary dipolar moment, which induces dipoles in the neighboring molecules. The result of this induction is an attractive dipole-dipole force. London demonstrated that in simple molecules with spherical symmetry the dispersion potential energy changes according to the law  $r^{-6}$ , where  $r$  is the interparticle distance. The expression of London is not valid at short distances, since the forces become repulsive as the electronic orbitals of the molecules overlap.

Theoretical considerations indicate that the repulsive contribution should be expressed as an exponential function of the distance, however, in many situations is more convenient to represent it as an inverse law  $r^{-n}$ . To consider the attractive and repulsive contributions in non-polar molecules, as noble gases, it is usually supposed that the total interaction is a sum of both terms. Additionally, the location of the minimum  $U_{\min}(r)=-\varepsilon$  in the resulting expression is used to obtain

$$U_{ij}(r) = \varepsilon \frac{(n^n m^{-m})^{\frac{1}{n-m}}}{n-m} \left[ \left( \frac{\sigma}{r} \right)^n - \left( \frac{\sigma}{r} \right)^m \right]. \quad (2.71)$$

$n$  and  $m$  are positive constants and  $n > m$ . This equation proposed by Mie was extensively investigated by Lennard Jones. Using the theoretical result of London  $m = 6$ , Lennard Jones found that values of  $n$  between 8 and 14 can well reproduce the second virial coefficient. The powers 12-6 are the most widely used values because of its simplicity for the analytic calculation of some properties and also for the computation of forces in a simulation<sup>93</sup>. Here the 12-6 Lennard Jones potential is used to represent the interactions between Ar atoms, to calculate the non-bonded interactions between CH<sub>2</sub> groups and also to approximate the interactions between different types of atoms/groups (PE-Ar, PE-Pt and Pt-Ar).

## 2.2.2 Force Fields for Polymers

The level of detail used in a simulation for the representation of a molecule is based on the time and length scales involved in the phenomenon/system of interest. Some of the potential models commonly used in the simulation of polymers are listed below.

### 2.2.2.1 Potential LJ-FENE

One of the simplest models of a polymer chain is the LJ-FENE<sup>33-40</sup> potential. It consists of a valence term between the closest neighboring units in a chain and a non-bonded contribution to describe the interaction between units in different chains or separated by more than 2 to 3 bonds in a chain

$$\mathcal{U} = U_{ij}^{\text{b}} + U_{ij}^{\text{nb}} . \quad (2.72)$$

The units represent groups of atoms, for example, monomers.

### 2.2.2.2 United Atom Method (UAM)

In the United Atom Method<sup>71,94-96</sup> additional angular valence terms are included into the LJ-FENE model which constraint consecutive segments in a chain in their more energetically favoured conformations. These terms are: a bending and a torsion contribution

$$\mathcal{U} = U_{ij}^{\text{b}} + U_{ijk}^{\theta} + U_{ijkl}^{\phi} + U_{ij}^{\text{nb}} . \quad (2.73)$$

The three-body term  $U_{ijk}^{\theta}$  maintains the angle between 3 consecutive units of a chain  $ijk$  close to the dihedral value. Four consecutive units in a chain remain preferentially in the zigzag *trans* configuration, or *gauche* at higher temperatures, due to the torsion term  $U_{ijkl}^{\phi}$ . Here, as in the LJ-FENE potential, each unit represents an atom group, for example, in polyethylene each unit represents a methyl group (CH<sub>2</sub>).

### 2.2.2.3 All-Atoms Models

In the full atomistic models all the atoms of a molecule are explicitly considered. The intramolecular parameters are obtained from quantum approximations of the energy for different configurations in short segments of a chain.

$$\mathcal{U} = U_{ij}^b + U_{ijk}^\theta + U_{ijkl}^\phi + U_{ijk}^{r\theta} + U_{ijkl}^{\theta\theta} + U_{ijkl}^{\phi\theta} + U_{ij}^{\text{nb}}. \quad (2.74)$$

Additional cross terms  $U_{ijk}^{r\theta}$ ,  $U_{ijkl}^{\theta\theta}$  and  $U_{ijkl}^{\phi\theta}$  which increase the flexibility in the model parameterization. The atomistic models can be classified according to the training set of molecules used in their parameterization. Models as AMBER<sup>97</sup>, COMPASS<sup>98</sup>, OPLS-AA<sup>99</sup> and CHARM<sup>100</sup> have been parameterized for segments of organic molecules; peptides and amino acids, others as DREIDING<sup>101</sup> and UNIVERSAL<sup>102</sup> are of general character.

### 2.2.3 Many-Body Potentials for Metals, Embedded Atom Method (EAM)

Pair potentials do not well describe metals and alloys when impurities, fractures, defects, surfaces and interfaces are included. Some important differences between metals and systems described by pair interactions are found in the dependence of the cohesive energy to the coordination index in a crystal, their elastic behavior, and the relation between their vacancy energy and the cohesive energy<sup>103,104</sup>. For systems described by pair potentials the cohesive energy of an atom in a crystal is proportional to the coordination index  $z_c$  while in metals the energy scales as  $z_c^{1/2}$ . The ratio between the vacancy energy and the cohesive energy is 1 for pair potentials while in metals normally ranges from 0.40 to 0.25 and even smaller in some cases as gold. The elastic behavior is also not well described by pair potentials since the elastic constants always satisfies the Cauchy relation  $C_{12}/C_{44}=1$  while in metals this ratio is about 3.7. Summarizing, pair potential functions, where the many-body effects does not explicitly appear, cannot reproduce the realistic potential field of metals. The angle dependence of potential is, in general, not as critical as for covalent cases such as carbon and silicon, because *d*-orbital electrons are more flexible<sup>105</sup>.

The Embedded Atom Method (EAM) developed by Daw and Baskes<sup>106-111</sup> overcomes the main problems with two-body potentials. Similar to the quasi-atom

concept of Stott and Zaremba<sup>112</sup> and the effective medium (jellium) approximation of Nørskov and Lang<sup>113</sup>, the main idea behind EAM is that the attractive energy can be viewed as the necessary energy to embed an atom into the local electron density provided by the remaining atoms.

In the quasi-atom theory of Stott and Zaremba an atom of a solid can be viewed as a defect in the system, then the embedding energy of the defect of coordination index  $z_c$  at a point  $r$  can be described by a functional of the electron density provided by the surrounding atoms. The functional has a universal character, it does not depend on the system, but its expression is unknown. Then the total cohesive energy of the system could be described by

$$U = \sum_i F_i(\rho_{h,i}). \quad (2.75)$$

$\rho_{h,i}$  is the host electron density at the position of the atom  $i$  due to the remaining atoms of the system,  $F_i$  is the energy (gain) to embed an atom of type  $i$  into the background electron density  $\rho$ . Atoms near a defect such as a surface are embedded into an electron gas of different profile than atoms in the bulk. The potential (2.75), however, is not sufficient to describe a solid, because it does not consider a core-core pair repulsive term. Daw and Baskes added an electrostatic pair potential  $\phi_{ij}$  to the Equation (2.75)

$$U = \sum_i F_i(\rho_{h,i}) + \frac{1}{2} \sum_i \sum_{j \neq i} \phi_{ij}(r_{ij}). \quad (2.76)$$

This energy contribution is defined by a Coulomb potential in terms of effective charges of the atoms of type  $i$  and  $j$

$$\phi_{ij}(r) = \frac{1}{4\pi\epsilon_0} \frac{Z_i(r)Z_j(r)}{r}. \quad (2.77)$$

Where  $\epsilon_0$  is the permittivity of free space. According to Daw and Baskes the host electron density is approximated by a linear superposition of the surrounding atoms, in other words, the sum of the atomic densities of the surrounding atoms  $j$  at the point  $i$

$$\rho_{h,i} = \sum_{j \neq i} \rho_j^{\text{at}}(r_{ij}). \quad (2.78)$$

With the approximation (2.78) for the electron density, EAM does not require more computations than pair potentials. Note that the embedding function  $F_i$  only depends on the nature of the atom  $i$ , and does not depend on the source of the background electron density. Thus the same embedding function can be used to determine the energy of an atom in an alloy or in a pure substance.

The atomic electron density is computed from Hartree-Fock wave functions calculated by Clementi and Roetti<sup>114</sup> and McLean and McLean<sup>115</sup>

$$\rho^{\text{at}}(r) = n_s |\psi_s(r)|^2 + n_d |\psi_d(r)|^2. \quad (2.79)$$

$n_s$  and  $n_d$  are the number of outer  $s$  and  $d$  electrons and are their corresponding densities.  $n_s$  is normally used as adjustable parameter while  $n_d$  satisfies  $n_v = n_s + n_d$ , where  $n_v$  is the valence number. The  $s$  and  $d$  densities are calculated from the spherically averaged wave functions

$$\psi(r) = \sum_i \frac{C_i (2\xi_i)^{(n_i+1/2)}}{(4\pi(2n_i)!)^{1/2}} r^{n_i-1} e^{-\xi_i r}. \quad (2.80)$$

The atomic electron density is truncated and shifted at a cut-off radius between the third and fourth shell of neighbors in the crystalline structure of the metal

$$\rho^{\text{at}}(r) \leftarrow \rho^{\text{at}}(r) - \rho^{\text{at}}(r_c), \text{ for } r < r_c. \quad (2.81)$$

Parameters for platinum  $n_s$ ,  $n_v$  and  $r_c$  used in this work and the constants for the calculation of the atomic electronic densities are reported in the Table 3.6.

The embedding function  $F(\rho)$  as the effective charge  $Z(r)$  are not universal. They are in general represented as simple functions or cubic splines and adjusted to experimental data such as the cohesive energy, lattice constants, vacancy energy, elastic constants and phonon frequencies. The function  $F(\rho)$  must satisfy the following conditions; a) it should have a minimum b) it shows a linear behavior at high electron

density and c) it converges to zero when the electron density vanishes. The function  $Z(r)$  a) must be monotonous and positive and b) it should vanish at large distance.

Different strategies to determine  $F(\rho)$  and the pair repulsive potential  $\phi(r)$  have been used in the development of the diverse versions of EAM. According to Foiles *et al.*<sup>108</sup>, the pair repulsive contribution is initially determined and  $F(\rho)$  is determined by the comparison with the universal energy law of Rose *et al.*<sup>116</sup> The law, Equation (2.82), relates the sublimation energy  $E_{sub}$  of a metal with its lattice constant  $a$

$$E_{sub}(a) = -E_0(1 + a^*)e^{-a^*}. \quad (2.82)$$

$E_0$  is the absolute sublimation energy at zero temperature and pressure. The quantity  $a^*$  is a measure of the deviation from the equilibrium lattice constant

$$a^* = \frac{(a/a_0 - 1)}{\sqrt{E_0/(9B\Omega)}}. \quad (2.83)$$

$B$  is the bulk modulus,  $a$  is the lattice constant,  $a_0$  is the equilibrium lattice constant and  $\Omega$  is the equilibrium volume per atom. In order to obtain  $F(\rho)$  the pair repulsive term is calculated  $\phi(r)$  in a perfect crystal from the Equation (2.77), the host density is calculated using the linear superposition of atomic densities (2.79), and then the embedding function  $F(\rho)$  is modified so that the energy matches the universal energy function

$$F(\rho) = E(a) - \frac{1}{2} \sum_i z_i \phi(a_i r) \quad (2.84)$$

$$\rho = \sum_i z_i \rho^{at}(a_i r). \quad (2.85)$$

Here  $i$  denote a shell of neighbors,  $r$  is the distance of any atom to its first neighbors,  $z_i$  the number of neighbors in the shell  $i$  and  $a_i$  the ratio between the distance to the  $i$ -th neighbors and the distance to the first neighbors.

# Chapter 3

## Results

In this Chapter simulation results and their analysis are presented. In the Section 3.1 two UAM models were compared according to their ability to predict the properties of polyethylene (PE) in condensed bulk phase. Among them: the density of crystalline phases at different temperatures, the transition between the orthorhombic and hexagonal crystalline structures, the formation of *gauche* defects in a crystal and the glass transition temperature. Next, polyethylene films are simulated and characterized through its change in the linear thermal expansion coefficient at the glass temperature. In the Sections 3.2 and 3.3 the simulation results of condensation of vapors (Ar and Pt) in contact with polyethylene substrates are presented. For each case the dynamics of nucleation and the different types of growth are elucidated.

### 3.1 Simulations of Polyethylene

In this work the United Atom Model (UAM) is used to simulate polyethylene in bulk and thin films. In comparison to full atomistic models and excluded-volume models, the used model exhibits an intermediate level of detail. It has less degrees of freedom than full atomistic models, since each carbon atom with its bonded hydrogen atoms are represented as a single methyl group. Nevertheless, in contrast to excluded-volume models, torsion and dihedral angle contributions are included.

A good indicator of the quality of a model is its ability to predict the properties of a system in condensed phase. Here, molecular dynamics simulations are performed in

order to test the reliability of two UAM models to predict the thermal behavior of polyethylene. Equilibrium properties such as the density, distribution of local conformations and the local structure are obtained at different temperatures from averages calculated in the production phase.

Experiments and full-atomistic simulations with PE reveal a transition between two crystalline phases; orthorhombic and hexagonal. In these studies the stabilization of the orthorhombic phase at low temperature has been attributed to the relative orientation of the hydrogen atoms in the PE chains and the transition between the two crystalline phases has been related to the interchange between the local conformations; *trans* and *gauche*. One goal of this study is to determine whether the stable low temperature crystalline phases of PE can be reproduced by UAM models, where the hydrogen atoms do not explicitly appear.

The UAM model was also used to characterize glasses of PE obtained from the cooling of polymer in bulk liquid phase. The glass transition temperature of these systems was detected as the point where the thermal expansion of the glass-former changes along a cooling curve at constant pressure. The dependence of the system properties to confinement is studied through simulations of thin polymer films. Later, large films of PE are equilibrated by means of simulations in  $NpT$  ensemble for the study of condensation of vapor phases on polymer surfaces.

### 3.1.1 UAM models for Polyethylene

In the United Atom model for polyethylene of Rigby and Roe<sup>71</sup> the polymer chains are linear sequences of spherical segments connected by valence bonds represented as harmonic oscillators

$$U_{ij}^b = \frac{1}{2} k_b (r_{ij} - r_0)^2. \quad (3.1)$$

Here  $r_0$  is the bond length corresponding to the lowest bond energy. Sumpter *et al.*<sup>94-96</sup> use a Morse potential to represent this contribution. The Morse function is asymmetric around the minimum energy value of the bond length, the repulsive energy at short distances is higher than the attractive energy for the same displacement from  $r=r_0$



$$U_{ij}^b = D \left[ 1 - e^{-\zeta(r_{ij} - r_0)} \right]^2. \quad (3.2)$$

The valence angle between three consecutive units of a chain are constrained close to the tetrahedral value  $\theta_0$  by means of a quadratic potential in  $\cos \theta$

$$U_j^\theta = \frac{1}{2} k_\theta (\cos \theta_j - \cos \theta_0)^2. \quad (3.3)$$

The torsion contribution of the (twist) angle formed between four consecutive units is described by a sum in  $\cos \phi$

$$U_j^\phi = k_\phi \sum_{i=0}^5 a_i \cos^i \phi_j. \quad (3.4)$$

The minimum energy torsion configurations are *trans* at  $\phi=0^\circ$ , and *gauche* at  $\phi=120^\circ$ , while the *cis* at  $\phi=180^\circ$ , is the maximal energy configuration (see Fig 3.1).



Figure 3.1. *Trans* (left) and *cis* (right) configurations in a segment of a polyethylene molecule. C atoms in the skeleton of the chain are shown in black, H atoms in grey.

Van der Waals interactions between groups that belong to different chains and between groups separated by more than three bonds along the chain backbone are represented by a truncated 12-6 Lennard Jones potential

$$U_{ij}^{nb} = 4\varepsilon \left[ \left( \frac{\sigma}{r_{ij}} \right)^{12} - \left( \frac{\sigma}{r_{ij}} \right)^6 \right] + C, \text{ for } r_{ij} < r_c. \quad (3.5)$$

The bond valence parameter  $k_b$  is calculated, to establish a comparison between the two UAM models, by means of an second-order Mac-Laurin expansion of the Morse potential used by Sumpter *et al.* around  $r_0$ ,  $k_b \approx 2D\zeta^2 = 2.650 \cdot 10^{26}$ . The most important differences between the two models are (1) the parameter is about three times

higher in the parameterization of Rigby and Roe and (2) the energy barrier of the *cis* configuration is almost three times higher than in the model of Sumpter *et al.*

Rigby and Roe <sup>71</sup>		Sumpter <i>et al.</i> <sup>94-96</sup>	
		$D$ [Jmol <sup>-1</sup> ]	$3.3472 \cdot 10^5$
		$\zeta$ [m <sup>-1</sup> ]	$19.9 \cdot 10^9$
$k_b$ [Jm <sup>-2</sup> mol <sup>-1</sup> ]	$2.422 \cdot 10^{26}$	$k_b$ [Jm <sup>-2</sup> mol <sup>-1</sup> ] (*)	$2.650 \cdot 10^{26}$
$r_0$ [m]	$0.152 \cdot 10^{-9}$	$r_0$ [m]	$0.153 \cdot 10^{-9}$
$k_\theta$ [Jmol <sup>-1</sup> ]	$5.0 \cdot 10^5$	$k_\theta$ [Jmol <sup>-1</sup> ]	$1.3 \cdot 10^5$
$\cos \theta_0$	-0.3333	$\cos \theta_0$	-0.3907
$k_\phi$ [Jmol <sup>-1</sup> ]	9000	$k_\phi$ [Jmol <sup>-1</sup> ]	8370.4
$a_0$	1.0000	$a_0$	1.0000
$a_1$	1.3100	$a_1$	2.1994
$a_2$	-1.4140	$a_2$	0.0000
$a_3$	-0.3297	$a_3$	-3.1994
$a_4$	2.8280	$a_4$	0.0000
$a_5$	-3.3943	$a_5$	0.0000
$\varepsilon$ [Jmol <sup>-1</sup> ]	500.0	$\varepsilon$ [Jmol <sup>-1</sup> ]	493.7
$\sigma$ [m]	$0.38 \cdot 10^{-9}$	$\sigma$ [m]	$0.39 \cdot 10^{-9}$
$E_{t \rightarrow g}$ [Jmol <sup>-1</sup> ]	11978.7	$E_{t \rightarrow g}$ [Jmol <sup>-1</sup> ]	14245.4
$E_{cis}$ [Jmol <sup>-1</sup> ]	43452.0	$E_{cis}$ [Jmol <sup>-1</sup> ]	16740.8

Table 3.1. Parameters of the UAM for polyethylene in SI units

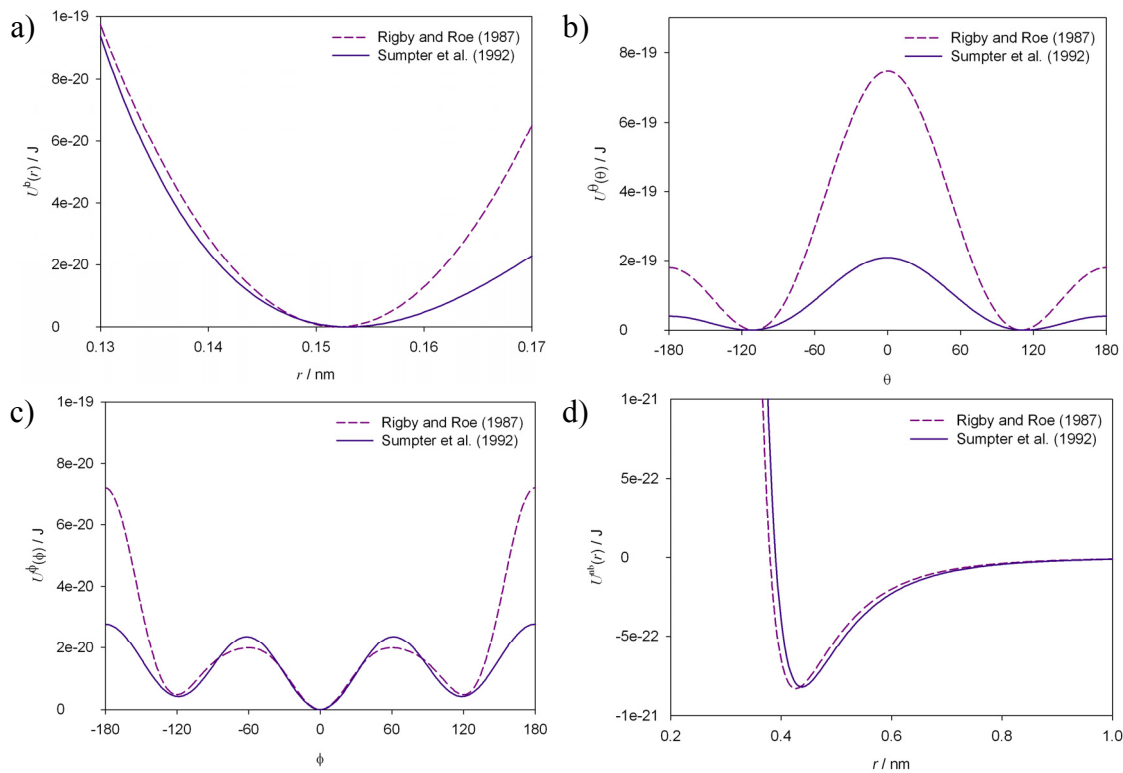


Figure 3.2. UAM functions for polyethylene a) Valence bond between consecutive CH<sub>2</sub> groups in a chain b) bending angle contribution between three consecutive units c) Torsion between four consecutive CH<sub>2</sub> groups in a chain d) Non-bonded interactions, Lennard Jones 12-6. Rigby and Roe model (solid) and Sumpter *et al.* (dashed).

### 3.1.2 Crystalline Phases of Polyethylene (UAM)

The equilibrium properties of polyethylene in crystalline solid phase at different temperatures in the range 50 to 450 K at zero external pressure are studied by  $NpT$  ensemble molecular dynamic simulations. Two different set of parameters of the United Atom Method are used (Table 3.1). The simulated system consists of 120 chains of 70  $\text{CH}_2$  groups each.

The crystallization is a slow phenomenon in comparison to the duration of a simulation, some nanoseconds, then, a trial crystalline structure is used as initial configuration. The  $\text{CH}_2$  groups are initially placed in an orthorhombic arrangement of lattice constants<sup>53</sup>  $a=0.741$  nm,  $b=0.494$  and  $c=0.256$  nm and setting angle<sup>57</sup>  $\varphi=43^\circ$ , values that correspond to the experimental data for this crystalline configuration (Fig. 3.3). The chains are infinite; the ends of each chain are connected through the periodic boundaries of the simulation box.

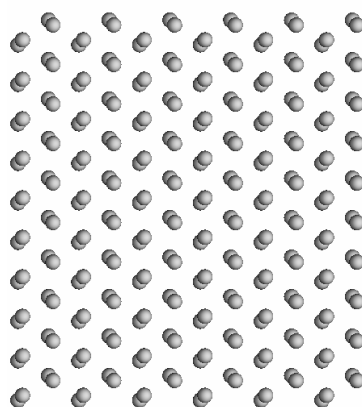


Figure 3.3. Projection  $xy$  of the initial orthorhombic configuration used for the simulations of polyethylene in crystalline phase.

The simulations are carried out at zero pressure and constant temperature, the evolution of the system is determined by means of the Equations (2.65) to (2.69), using an independent control of the pressure components  $x$ ,  $y$  and  $z$ .

The properties of the crystalline PE are determined in the range of temperature 50 to 450 K. A lapse of 1 ns is simulated at each temperature using an integration step  $\Delta t = 1$  fs. The same initial orthorhombic configuration is used for all simulations. The equilibrium properties are calculated from averages made on the last 200 ps of each simulation.

The density of the system reaches a stable value around 200 ps. Larger density fluctuations are observed at higher temperatures (Fig. 3.4).

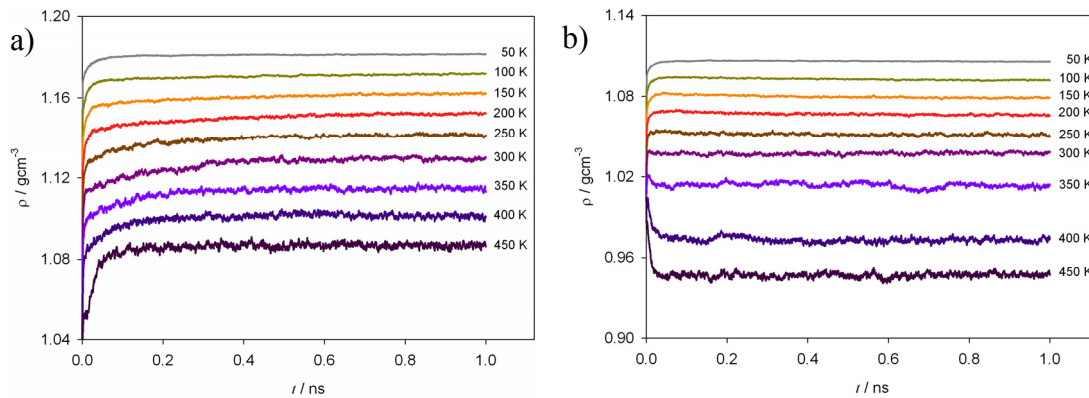


Figure 3.4. Temporal evolution of the density of PE at different temperatures for two set of parameters of the UAM model: a) Rigby and Roe and b) Sumpter *et al.*

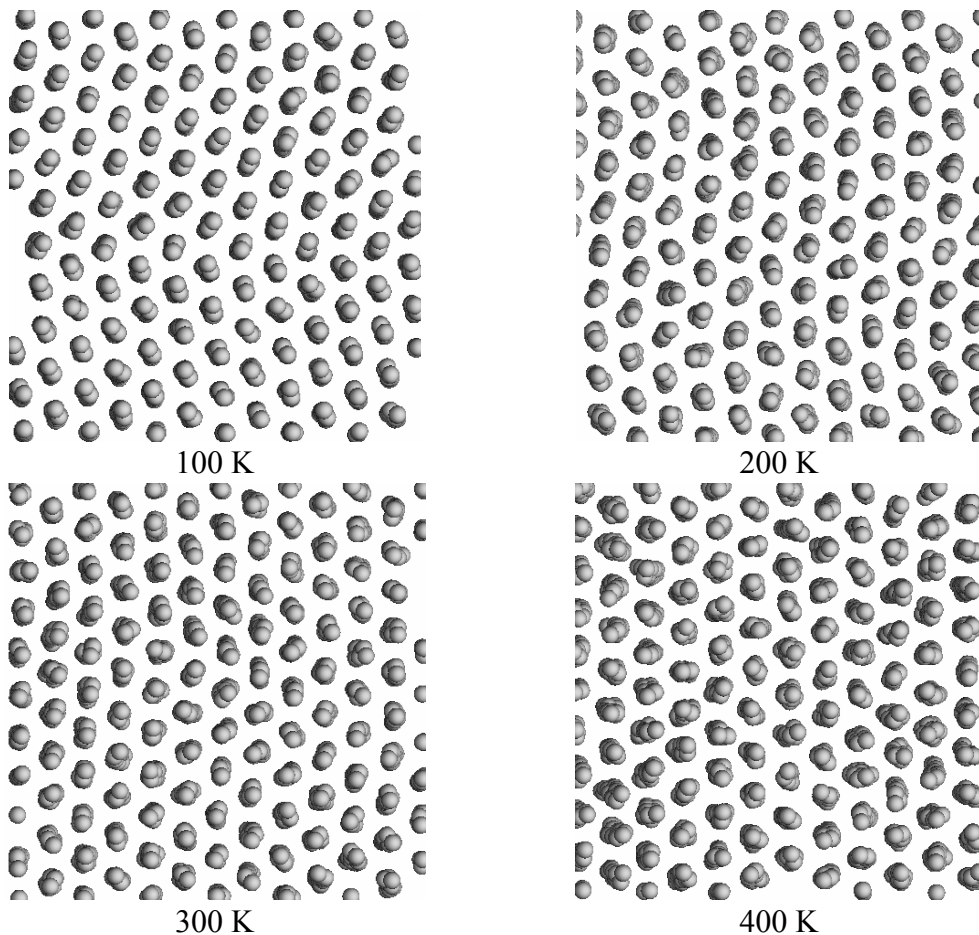


Figure 3.5. *xy* projections of PE chains in crystalline phase at equilibrium for simulations performed at different temperatures.

Transversal *xy* projections of the chains show that the system conserves the characteristic herringbone arrangement of the initial crystalline structure (Fig. 3.5). Above 300 K the chains show *gauche* defects, the amount of these defects increase

notably above this temperature. In opposition to the results obtained with a full-atom model, the CH<sub>2</sub>-CH<sub>2</sub> bonds do not exhibit a preferential orientation (setting angle).

In comparison the thermal behaviour of the density of the UAM models and of the full atom models shows similarities in the slope but a systematic discrepancy in all the range of temperature studied (see Fig. 3.6). The difference is always smaller in the case of the parameterization of Sumpter *et al.*, this indicates that the prediction of density is directly related to the parameters  $\sigma$  and  $r_0$  which controls the distances between chains and groups within the chain and consequently the volume of the CH<sub>2</sub> groups. A change in the thermal expansion coefficient is observed near 300 K.

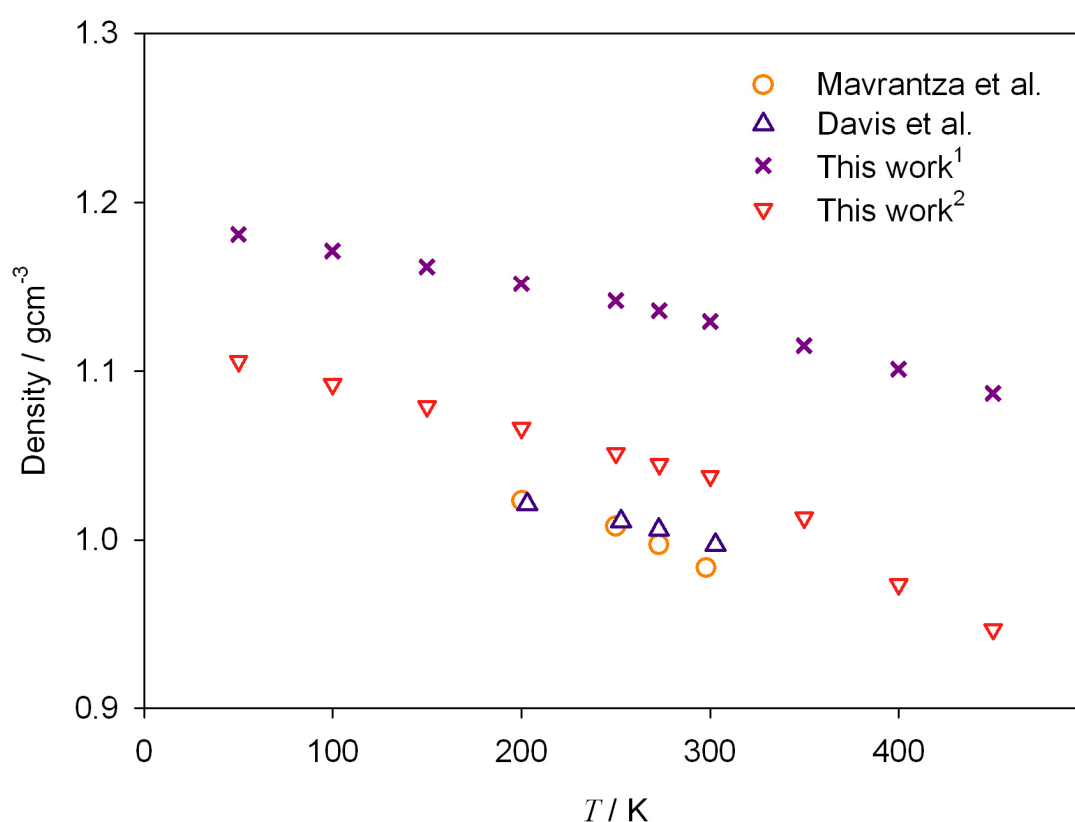


Figure 3.6. Density versus temperature of crystalline polyethylene simulated with different force fields, results are compared with experimental data<sup>117</sup> (purple triangles). Results obtained by the parameterization of (1) Rigby and Roe and (2) Sumpter *et al.*

The pronounced peaks in the radial distribution functions correspond to neighbors in a same chain (Fig. 3.7a). The RDF function is decomposed into two functions a) the radial distribution between groups which belongs to a same chain and b) the radial distribution between groups of different chains (Fig. 3.7b). The latter function is useful to discern between different crystalline structures since the lattice constants  $a$  and  $b$  are related to the closest distances between CH<sub>2</sub> groups in different

chains (see Fig. 1.6). At low temperature  $T < 200$  K the distribution b) exhibits two separated modes characteristic of an orthorhombic structure for distances lower than  $r < 1.5\sigma$ . At higher temperature these modes collapse in a single mode as in the hexagonal phase (Fig. 3.8).

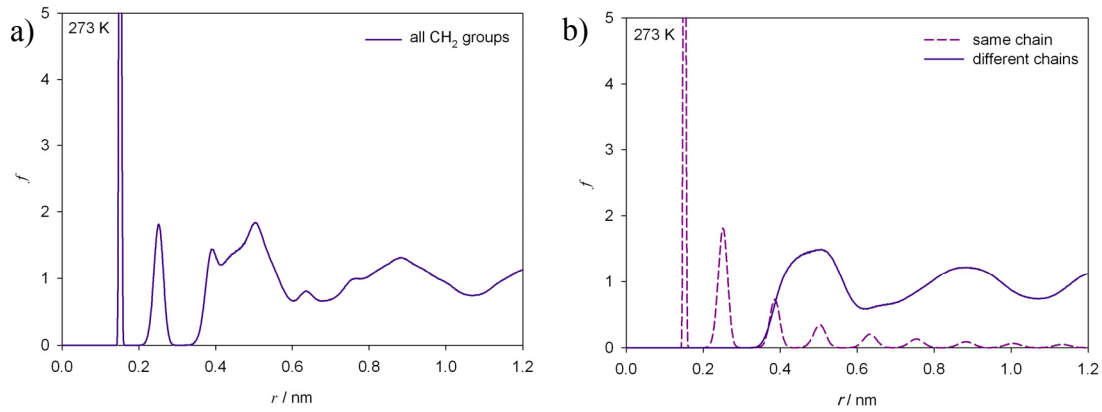


Figure 3.7. Radial distribution function of PE at 273K a) for all methyl groups b) decomposition of the function; between  $\text{CH}_2$  groups in different chains (solid) and between groups in a chain (dashed).

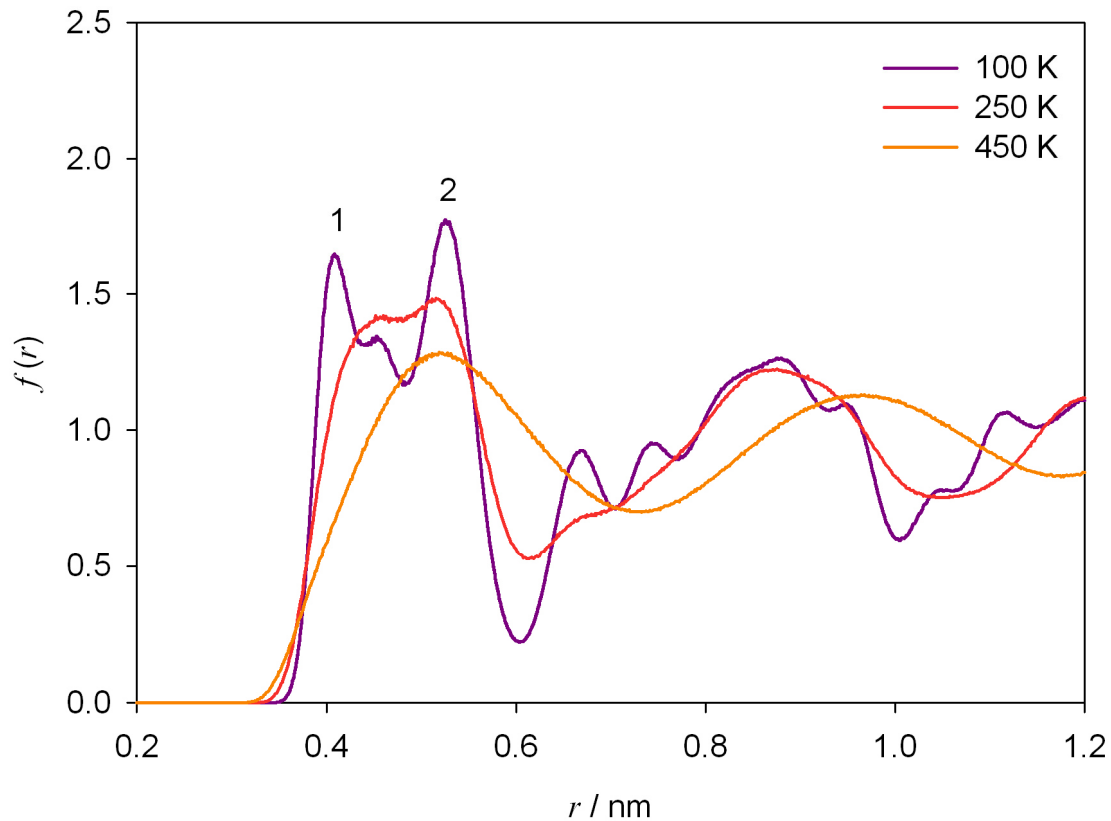


Figure 3.8. Radial distribution function of  $\text{CH}_2$  groups on different chains for different temperatures;  $T=100$  K (purple),  $T=250$  K (red) and  $T=450$  K (orange). Two modes are distinguishable at low temperatures; they collapse as the temperature increases.

The concentration of *gauche* defects in the crystal at a given temperature is determined from the distribution function of torsion angles. The concentration of *trans*

configurations in the samples, is determined by integrating the torsion angle distribution in the interval  $\phi \in [-180^\circ, -60^\circ] \cup [60^\circ, 180^\circ]$  (see Fig. 3.9a).

Below 273 K the amount of defects observed in the crystal at temperatures is very low. An exponential increase of the *gauche* defects is detected above 300 K in agreement with experiments and atomistic simulations (Fig. 3.9b).

The slight change in the thermal expansion coefficient near 300 K observed in the Figure 3.6 appears to be related to the exponential growth of the *gauche* defects above this temperature. These defects are responsible for the stabilization of the hexagonal phase at high temperatures.

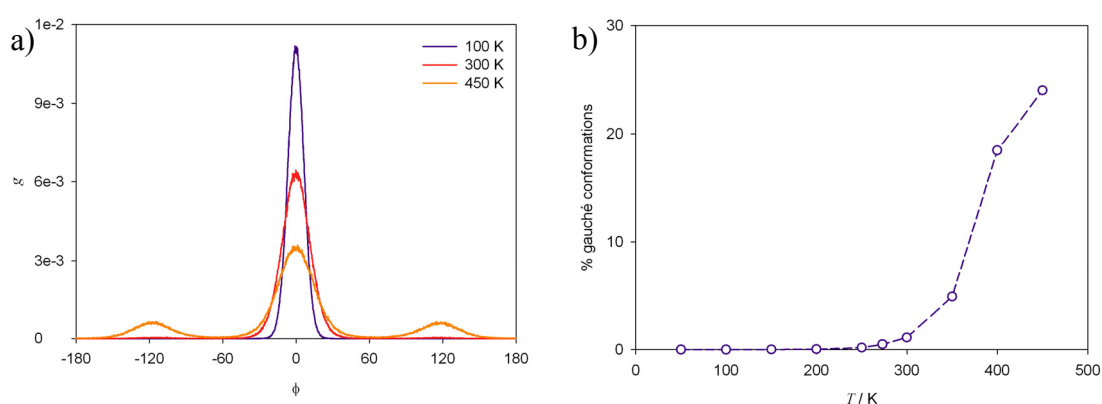


Figure 3.9. a) Distribution of torsion angles of PE at different temperatures. The conversion of *trans* configurations into *gauche* defects notably increases at temperatures higher than 300 K, b) concentration of *gauche* defects versus temperature.

### 3.1.3 Glass Transition of Polyethylene (UAM)

The glass temperature was here determined by molecular dynamics simulations of UAM polyethylene using the parameters of Sumpter *et al.*<sup>94-96</sup>

Simulations of polyethylene in bulk phase and in film geometry were performed to study possible confinement effects on the glass transition. In previous simulation studies the glass transition has been related to changes in the thermal coefficients of density and internal energy, cessation of segmental diffusion and reduction of *trans-gauche* conformational transitions<sup>71</sup>. Here the glass temperature  $T_g$  is detected by changes of the thermal expansion coefficient.

### 3.1.3.1 Glass Transition of Bulk PE (UAM)

The simulated system consists of linear chains of equal length contained in a cubic box. Runs with different chain lengths are performed;  $m=30$  to 70 using a similar amount of  $\text{CH}_2$  groups (about 25000). An initial condition of highly intertwined chains is constructed by generating a network of randomly perturbed positions of a face centered cubic lattice representing centers of  $\text{CH}_2$  groups. Next, the groups are renumbered such that physically close neighbors have numerically close indices. A previous run is performed with weakened force constants for all potentials, except for the non-bonded interactions. Force constants are gradually switched to their original values as the bond lengths and dihedral angles converge towards their equilibrium values.

Isobaric curves are obtained by cooling an equilibrated sample using the velocity scaling thermostat at a cooling rate  $v=5 \cdot 10^{10} \text{ Ks}^{-1}$ . At each point of the curves presented in the Figure 3.10 an interval of 3 ns is simulated in  $NpT$  ensemble at  $p=0$ .

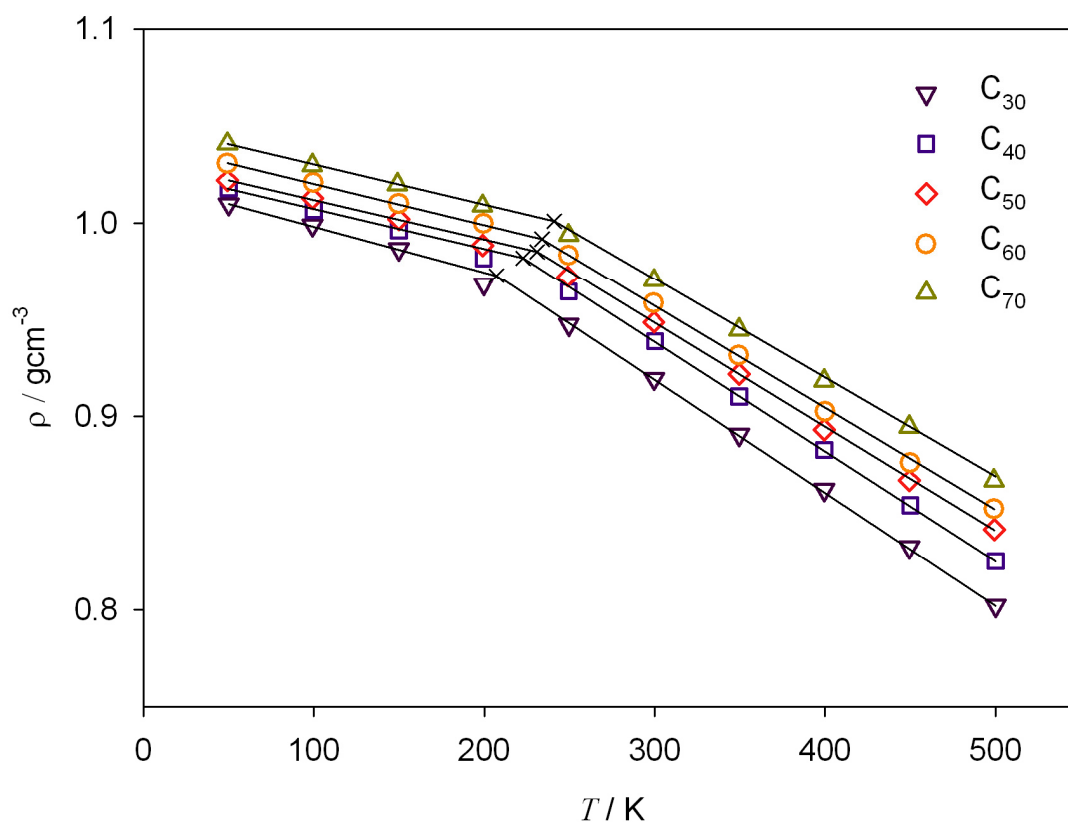


Figure 3.10. Density-temperature curves for UAM  $n$ -alkanes of different sizes. The glass transition temperature increases as the length of the chains increase.



The simulation results indicate that the glass transition temperature depends on the size of the chains used in the representation of a polymer. The glass transition temperature is higher for systems composed of longer chains (Fig. 3.10).

The kink in the curve density versus temperature for the system composed by chains of 70 CH<sub>2</sub> groups indicates a glass transition at  $T_{g\infty}=242$  K. This result agrees with reported values based on calorimetry experiments  $T_{g\infty} \sim 235$  K to 240 K and with MD simulations results obtained with the force field MSXX<sup>60,119</sup>  $T_{g\infty}=225$  K  $\pm$  10 K.

### 3.1.3.2 Glass Transition of PE (UAM) Films

The studies of Böhme and de Pablo<sup>47</sup> are here reproduced for polyethylene films composed of UAM chains. A polyethylene film composed by chains of 70 CH<sub>2</sub> groups is obtained in three stages; a) equilibration of a bulk semi-crystalline phase consisting of semi-infinite chains in  $NpT$  ensemble at  $T=400$  K, higher than the glass transition temperature  $T_g$  of the film, at  $p=0$  b) creation of two surfaces by means of a cut of the chains and expansion of the simulation box c) equilibration of the film in  $NVT$  ensemble at the final temperature of the film  $T_{PE}=290$  K. Periodic boundary conditions are applied in all stages. Films at different temperatures are obtained by cooling at  $\nu=5 \cdot 10^{10}$  Ks<sup>-1</sup> the film equilibrated at  $T_{PE}=290$  K.

The glass transition was detected by the change of the linear thermal expansion coefficient of the film. For this purpose, density profiles are calculated to determine the thickness of the film at the different temperatures simulated (see Fig. 3.11). Two average densities are computed: one calculated over the entire film  $\rho$  and another  $\rho'$  using only the inner region of the film, which is bounded by the points where the density exceeds  $\rho$ . Finally, the film thickness is calculated by assuming a uniform density  $\rho'$  across the whole film. The results are almost independent to the size of the bins used to construct the profiles.

Consistent with the results of de Pablo *et al.*<sup>47</sup> the film shows a lower glass transition temperature  $T_g=231$  K than the bulk  $T_{g\infty}=241$  K.

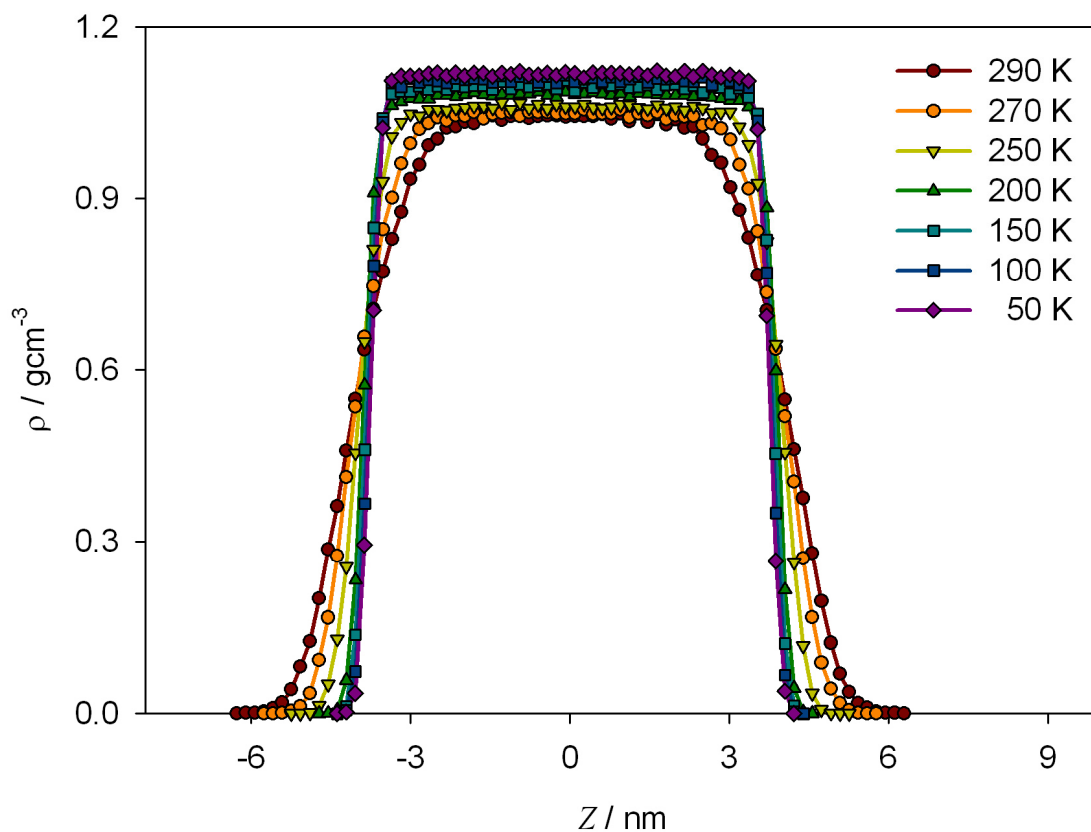


Figure 3.11. Density profiles of polyethylene films at different temperatures. The film consists of chains of 70 methyl groups.

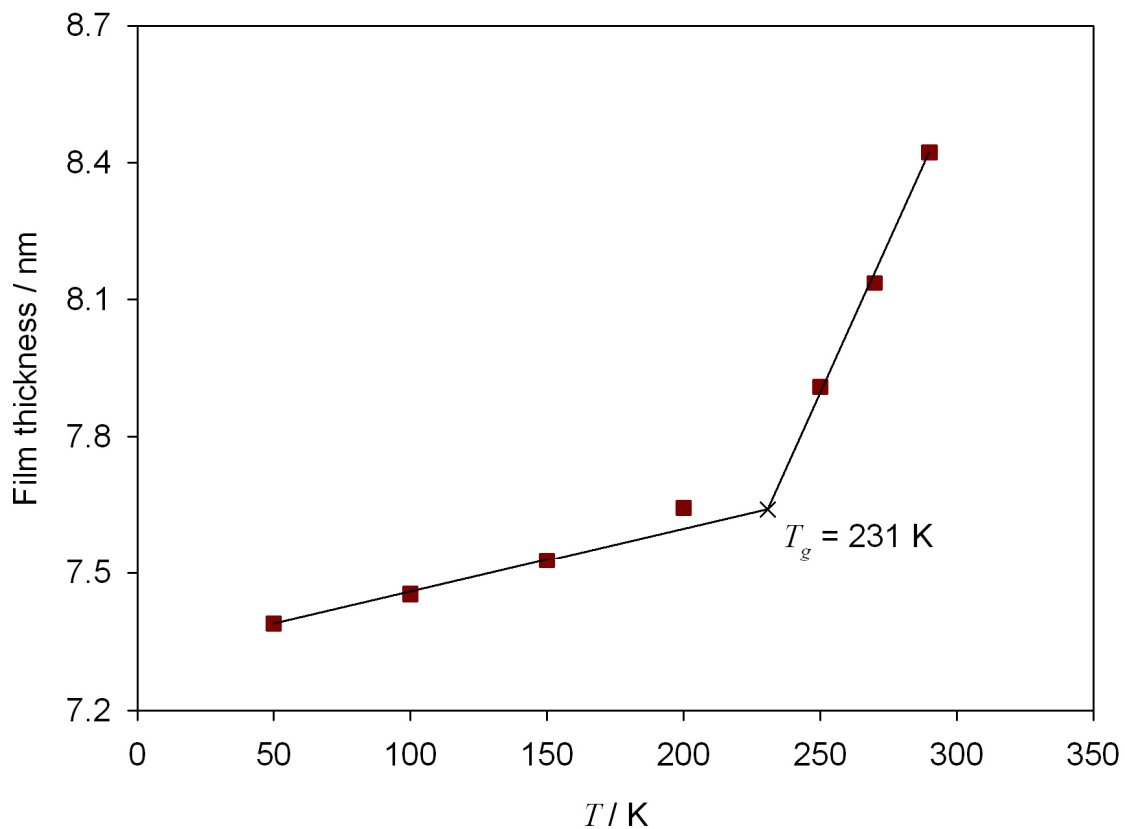


Figure 3.12. PE Film thickness, deduced from the density profiles, versus temperature. The glass transition temperature is calculated as the intersection point of the high and low temperature linear fits.

## 3.2 Condensation of Ar on PE Films

### 3.2.1 Characterization of Ar Clusters

The clusters of a condensed phase are characterized in the classic nucleation theory by their interfacial energy, density and contact angle. In the first growth stages, when the clusters have nanoscopic dimensions, these properties are size-dependent and are not easily defined. For this reason they are usually approximated by their corresponding bulk equilibrium values.

Molecular simulations provide enough information to calculate equilibrium properties: particle positions and velocities in different configurations. The properties of a thick enough film or a big enough drop converges towards their bulk values at the central region<sup>120-126</sup>. Here the properties of Ar clusters are obtained from simulations of the phase equilibrium between a liquid Ar film and its coexisting vapor at a given temperature.

To determine the properties of Ar clusters a truncated Lennard Jones potential with a cut-off  $r_c=2.5\sigma$  is used. The same potential is later used in the simulation of condensation of Ar on PE substrates.

The preparation of an equilibrated Ar film is similar to the described procedure to obtain a polymer film. The method proceeds in two stages; first a liquid bulk phase is equilibrated under periodic boundary conditions in  $NpT$  ensemble at  $p=0$ , the box is then expanded in one direction to produce two surfaces. In the second stage the obtained film is equilibrated in  $NVT$  ensemble. Some atoms evaporate in this stage until the vapor and liquid phases reach a new stationary state.

As starting configuration  $N=4913$  atoms are placed in a face centered-cubic lattice in a cubic box, the density is chosen close to the equilibrium value of the liquid phase which is available from experimental data. After a short melting and equilibration period of this homogeneous phase, two empty cubic cells of the same dimensions are added to both sides of the film in the  $z$ -direction, allowing the vapor phase to develop. The obtained film is then equilibrated in Nosé-Hoover  $NVT$  ensemble. The particle trajectories are solved using the Störmer-Verlet algorithm, Equations (2.49) and (2.50).

The densities and the interfacial tension of the coexisting phases are evaluated in the production stage. Bulk phase densities are determined from density profiles by taking the mean liquid and vapor densities excluding the interfacial region.

Periodic boundary conditions in all directions are used, because the implementation of hard reflecting walls in the  $z$ -direction introduces an additional momentum which could displace the center of mass of the film<sup>125</sup>. Additionally, the transformation of Melchionna was introduced in the Nosé-Hoover equations to ensure the conservation of momentum and to prevent the displacement of the film.

### 3.2.1.1 Interfacial Tension and LV Equilibrium Densities

As indicated in the Section 2.6.1.3 the pressure tensor in inhomogeneous systems depends on the position

$$\mathbf{p} = \mathbf{p}^K + \mathbf{p}^U. \quad (3.6)$$

The kinetic part of the pressure tensor of any system in equilibrium is always diagonal. In particular, in a film the configurational part is also diagonal, thus the pressure tensor of a film is diagonal<sup>72</sup> and can be written as

$$\mathbf{p}(z) = (\mathbf{e}_x \mathbf{e}_x + \mathbf{e}_y \mathbf{e}_y) p_T(z) + \mathbf{e}_z \mathbf{e}_z p_N(z). \quad (3.7)$$

$p_N$  and  $p_T$  are respectively the normal and tangential components of the pressure tensor

$$p_N(z) = p^z(z) \text{ and } p_T(z) = p^x(z) = p^y(z). \quad (3.8)$$

More than one definition can be found in literature for the local value of the pressure components<sup>127-129</sup>. The existing expressions differ in the definition of the configurational part. According to Irving and Kirkwood<sup>127</sup> all the pairs connected by a line which crosses a plane oriented to the  $z$ -axis contribute to the configurational part of the pressure at a given point  $z$ , thus the tangential and normal components of the pressure tensor are given by

$$p_N(z) = \rho(z)k_B T - \frac{1}{2A'} \sum_{i \neq j} |r_{ij}^z| \frac{1}{r_{ij}} \frac{\partial \mathcal{U}}{\partial r_{ij}} \Theta\left(\frac{z - r_i^z}{r_{ij}^z}\right) \Theta\left(\frac{r_j^z - z}{r_{ij}^z}\right) \quad (3.9)$$

$$p_T(z) = \rho(z)k_B T - \frac{1}{4A'} \sum_{i \neq j} \frac{r_{ij}^{x^2} + r_{ij}^{y^2}}{|r_{ij}^z|} \frac{1}{r_{ij}} \frac{\partial \mathcal{U}}{\partial r_{ij}} \Theta\left(\frac{r_i^z - z}{r_{ij}^z}\right) \Theta\left(\frac{z - r_j^z}{r_{ij}^z}\right). \quad (3.10)$$

$\Theta(x)$  is here the Heaviside function defined as;  $\Theta(x) = 1$  if  $x > 0$  and 0 in other case. The multiplication of Heaviside functions in (3.9) and (3.10) is equivalent to perform a sum where only the pairs which cross the plane  $z$  are considered.

As the Figure 3.13 shows all components of pressure tensor converge to the same value in bulk liquid and vapor phases. Though the normal component keeps a constant value, tangential pressure exhibits a drop near the liquid-vapor interface.

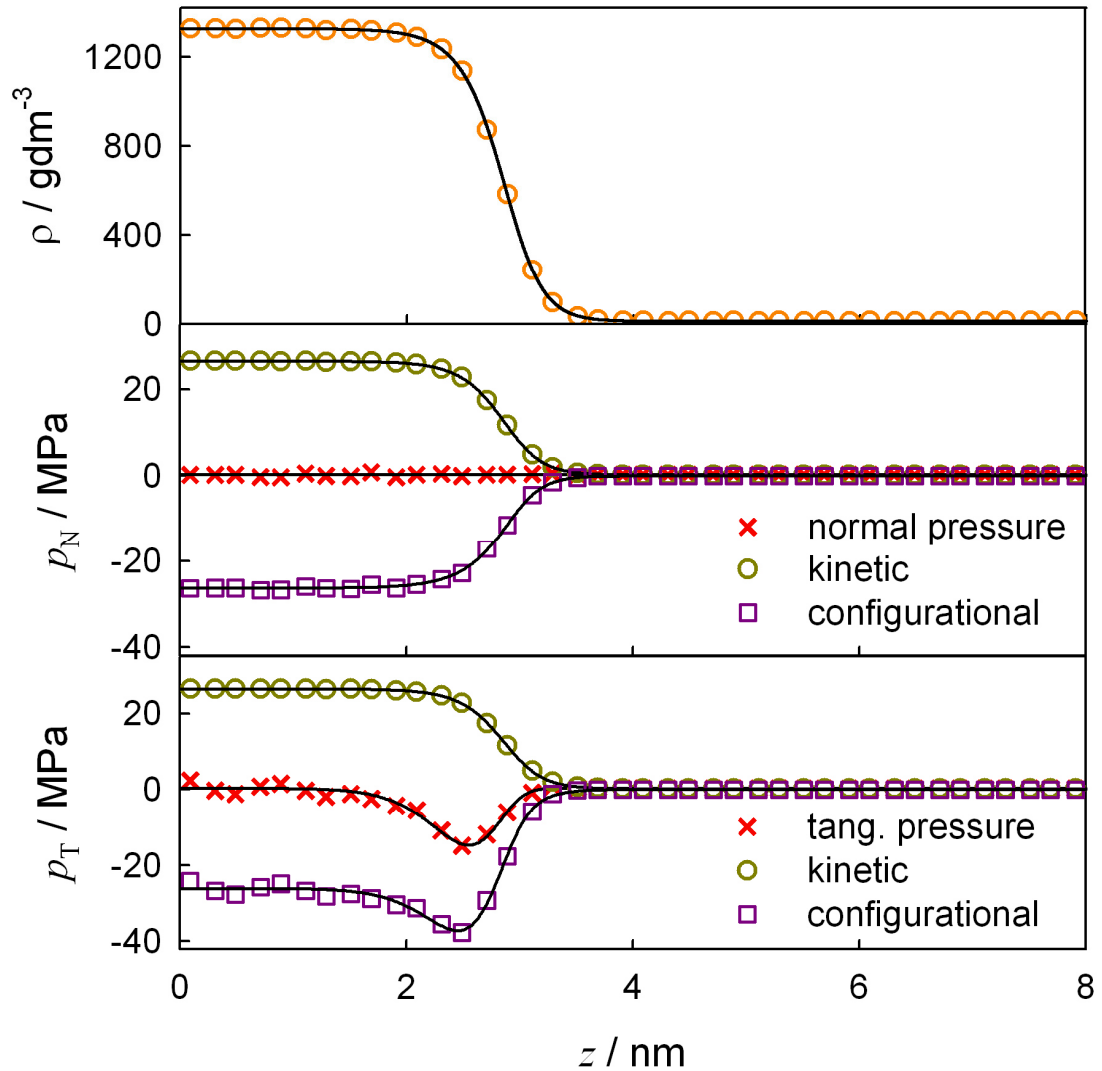


Figure 3.13. Density and pressure profiles of Ar LJ-2.5 $\sigma$  along the transversal direction of the film. The simulations were performed with 5000 Ar atoms, the film was equilibrated at  $T=96$  K.

Surface tension is computed using the definition of Kirkwood and Buff<sup>130</sup> by integrating the difference between the pressure components across the interface.

$$\gamma = \int_1^v [p_N(z) - p_T(z)] dz = \frac{1}{4A'} \left\langle \sum_{i \neq j} \frac{r_{ij}^2 - 3r_{ij}^z{}^2}{r_{ij}} \frac{\partial \mathcal{U}}{\partial r_{ij}} \right\rangle. \quad (3.11)$$

$A'$  is the total area of the film  $A' = L^x L^y$ , the brackets denote time averages made over different configurations in the production phase. This method has been extensively used to study the liquid-vapor interfacial properties of a Lennard Jones fluid under periodic boundary conditions<sup>120-126</sup>. The method was here used to calculate the interfacial tension of an Ar film at different temperatures using a truncated potential. For this purpose, only the pairs at a distance lower than the cut-off radius are included in the sum (3.11).

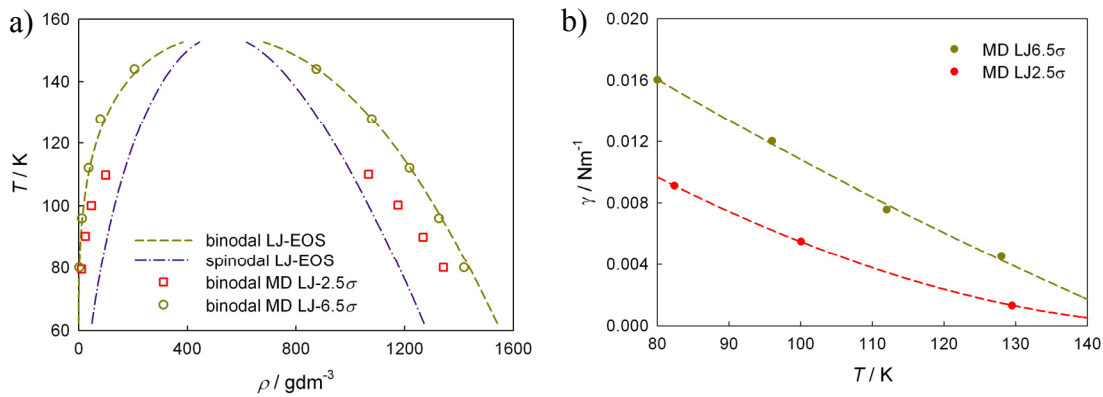


Figure 3.14. MD Simulation equilibrium results for Ar using a truncated Lennard Jones potential and different cut-off radii. a) T-p phase diagram for Ar. Simulation results are compared with a LJ-EOS<sup>131</sup>. b) interfacial tension of Ar versus temperature for;  $r_c = 2.5\sigma$  without LRC (red) and  $r_c = 6.5\sigma$  with LRC (green)<sup>125</sup>.

For the simulated system the vapor equilibrium densities are higher than the experimental values, while the liquid density exhibits an opposite behavior (see Fig. 3.14a). This result is a direct consequence of the truncation of the potential. At distances higher than the cut-off radius pair interactions are attractive, then, due to the lower cohesion of the condensed phase more atoms stabilize on the vapor phase at a given temperature. Another effect of the potential truncation on the liquid-vapor phase diagram is a reduction of the critical temperature and consequently a displacement of the binodal and spinodal curves. The interfacial energy is especially sensible to the size of the cut-off radius. In the Figure 3.14b results for the interfacial tension at different temperatures calculated using the expression (3.11) and a cut-off equal to  $2.5\sigma$  are

presented and compared with simulation results<sup>125</sup> obtained for larger cut-off radii and long range corrections (LRC). Larger cut-off radii improve the agreement of simulation results with experimental data, but the amount of pair interactions notably increases.

For the reproduction of experimental data cut-off radii higher than  $5\sigma$  in combination with long-range corrections are recommendable (see Fig. 3.14). Different long-range corrections have been proposed in literature<sup>125</sup>. No one of them are here applied since the aim of the present simulations is to determine the properties of Ar clusters which are later required for the interpretation of the simulations of condensation of Ar on polymer substrates, where the same truncated potential is used.

### 3.2.1.2 Contact Angle

The microscopic solid-liquid contact angle is a fundamental variable in the heterogeneous nucleation theory since it determines the growth mechanism of clusters on a surface.

The effect of the Lennard Jones potential parameters for the attraction in the fluid and between the liquid and the solid surface on the wetting behavior has been studied by molecular simulations of a droplet equilibrated on an atomic crystalline surface<sup>132-134</sup>. The effect of the interaction between atoms in a liquid cluster and their interactions with a solid surface of atoms on the wetting has been studied by molecular simulations<sup>132-134</sup>. Maruyama *et al.*<sup>134</sup> determined the contact angle of equilibrated droplets on solid surfaces consisting of about 5000 Ar Lennard Jones centers by MD simulations. The atoms, initially placed in a cube in contact with a substrate, tend to build a droplet on the surface. Conditions close to the equilibrium were used at the beginning of the simulation *i.e.* the density of the initial crystalline configuration was chosen similar to the corresponding liquid phase at the temperature of the surface.

The contact angle was determined from two-dimensional density profiles of an equilibrated droplet. Except for the first two layers the profiles show a semi-spherical shape (Fig. 3.15). These simulation results show that the macroscopic Young's Equation (1.7) is still valid for small droplets and that the cosine of the contact angle linearly depends on the ratio  $\epsilon_{\text{surf}}/\epsilon$ , where  $\epsilon_{\text{surf}}$  denotes the depth of the integrated potential between the surface and ad-atom and  $\epsilon$  the depth of the potential between the ad-atoms. Modifications of the energy parameter  $\epsilon_{\text{surf}}$  lead to proportional changes in the

solid-liquid surface  $\gamma_i$  energy, while the solid-gas  $\gamma_s$  and liquid-gas  $\gamma$  surface energies remain approximately constant.

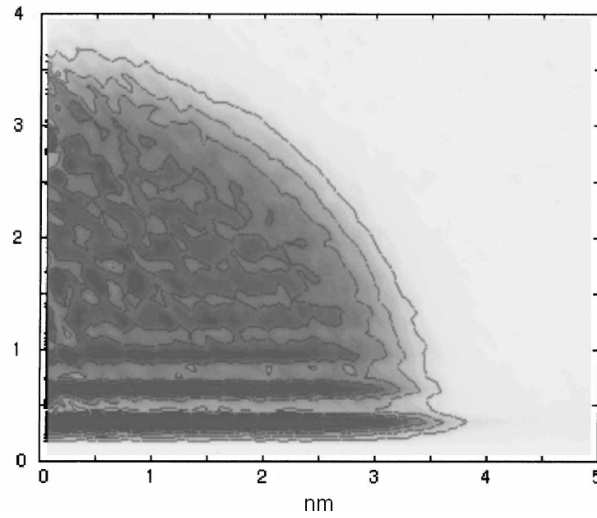


Figure 3.15. Two-dimensional density profile generated from molecular dynamics simulation of a cap of Ar atoms deposited on a smooth surface<sup>134</sup>. The cap consists of 1600 atoms. In the Figure a contact angle of  $90^\circ$  was determined at  $T_{\text{surf}}=92$  K.

Simulations performed with different surfaces shown the universal character of the relation  $\cos\theta$  vs.  $\epsilon_{\text{surf}}/\epsilon$ . The contact angle was identical for different combinations of the surface atoms LJ parameters with the same value of  $\epsilon_{\text{surf}}$ .

### 3.2.2 Simulation Methodology for the System PE-Ar

Condensation of Ar atoms on surfaces of semicrystalline polyethylene films is simulated by means of molecular dynamics method. The specific system is chosen as model for high wettable systems. The vapor phase consists of 5000 Ar atoms and the interaction between them is represented by a 12-6 Lennard Jones potential with parameters<sup>135</sup>  $\sigma_{\text{Ar}}=0.3405$  nm,  $\epsilon_{\text{Ar}}=1.013 \cdot 10^{-2}$  eV and  $r_c=2.5\sigma_{\text{Ar}}$ .

The polyethylene films consist of 374 linear chains of 70 methyl groups each (26180 sites). The UAM with the parameters reported in the Table 3.1 was used.

Non-bonded interactions between methyl groups and Ar atoms are approximated by a Lennard Jones potential with Lorentz-Berthelot cross parameters.

$$\sigma_{\text{PE-Ar}} = (\sigma_{\text{PE}} + \sigma_{\text{Ar}}) / 2 \quad (3.12)$$

$$\epsilon_{\text{PE-Ar}} = (\epsilon_{\text{PE}} \epsilon_{\text{Ar}})^{1/2}. \quad (3.13)$$



To generate initial configurations, particle positions and velocities, PE and Ar subsystems were independently equilibrated. The vapor phase is independently equilibrated at a supercritical temperature  $T_{\text{Ar}}=200$  K. PE films are obtained by the method described in Section and equilibrated at two temperatures: 60 K and 80 K. The Table 3.2 summarizes the initial condition of the simulations.

The Ar atoms are put in contact with the film with a minimum initial separation equal to  $1.5\sigma_{\text{Ar}}$ , big enough to avoid possible high repulsive pairs and little enough to reduce the expansion of the vapor.

Sim.	$T_{\text{Ar}} / \text{K}$	$T_{\text{PE}} / \text{K}$	$\rho_{\text{Ar}} / \text{gcm}^{-3}$	Sim.	$T_{\text{Ar}} / \text{K}$	$T_{\text{PE}} / \text{K}$	$\rho_{\text{Ar}} / \text{gcm}^{-3}$
A <sub>1</sub>	200	60	0.005	B <sub>1</sub>	200	80	0.010
A <sub>2</sub>	200	60	0.010	B <sub>2</sub>	200	80	0.020
A <sub>3</sub>	200	60	0.015	B <sub>3</sub>	200	80	0.030
A <sub>4</sub>	200	60	0.020	B <sub>4</sub>	200	80	0.040
A <sub>5</sub>	200	60	0.025	B <sub>5</sub>	200	80	0.050
A <sub>6</sub>	200	60	0.030	B <sub>6</sub>	200	80	0.060

Table 3.2. Initial conditions for the simulations of condensation of Ar atoms on PE films

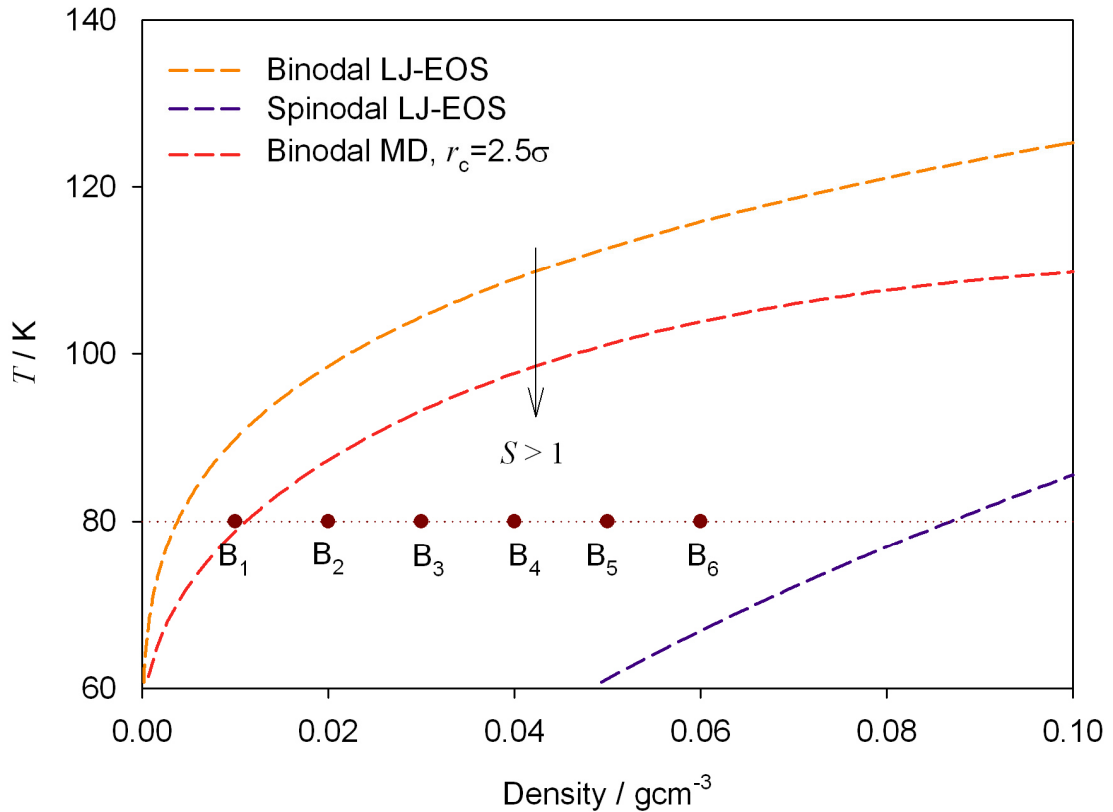


Figure 3.16. Schematic evolution of the system on the phase diagram of Ar. The temperature of Ar decreases in response to the contact with the cold polymer surface until crosses to the metastability zone.

During the simulation a Nosé-Hoover thermostat is applied to the film with a mass parameter given by

$$Q = 6N_{\text{CH}_2} k_B T_{\text{PE}} m_{\text{CH}_2} \sigma_{\text{CH}_2}^2 \varepsilon_{\text{CH}_2}^{-1}. \quad (3.14)$$

This choice of the parameter  $Q$  nearly corresponds to the resonance value between the response frequency of thermostat and the natural frequency of a pair of methyl Lennard Jones centers. Any kind of thermostat is applied to the Ar atoms. The equations of motion, Newton for the Ar atoms and Nosé-Hoover for the methyl groups, are integrated with the Störmer-Verlet method using an integration step of  $\Delta t=1$  fs.

Clustering phenomena were monitored by a cluster recognition algorithm (see Appendix A.4) based on the Stillinger's criterion<sup>136</sup>. The cluster search can be briefly described as follows; two particles are connected if the distance between them is smaller than a given cut-off distance, therefore, two particles are part of the same cluster if they are directly connected or through a path of connected particles. The cut-off distance to define whether two particles are neighbors is usually taken as the typical separation between a particle and its first shell of neighbors in condensed phase, which can be determined from the position of the first minimum in the radial distribution function. A typical value of  $1.5\sigma_{\text{Ar}}$  is used. The amount of monomers in vapor does not sensible change when this value is changed to  $1.2\sigma_{\text{Ar}}$ .

Not all the pairs instantaneously separated by a distance minor to  $1.5\sigma$  belong necessarily to a cluster, since the probability of collisions of two or more particles in a sphere of finite radius is not zero. Some particles collide and then follow different trajectories. Stillinger's criterion, which is based on the relative positions of particles in a given configuration only, can be improved by means of stability considerations: Two particles at a distance smaller than a given value form a stable cluster if the kinetic relative energy of a pair is lower than its cohesive energy<sup>137</sup>.

The recognition of the atoms deposited on the surface is performed in two steps a) the search of the methyl groups located on the film surface b) the search of Ar atoms in direct contact with the surface methyl groups, labelled 1<sup>st</sup> layer atoms. Next Ar atoms in contact with the 1<sup>st</sup> layer atoms are labelled as 2<sup>nd</sup> layer atoms and so on, until the search of deposited atoms is exhausted.

The methods here described, and detailed in the Appendix A.4, allow the recognition and characterization of the subsystems; bulk and surface of the polymer film, Ar clusters and vapor phase.

### 3.2.3 Results

Snapshots of the simulations (see Fig. 3.17) and the evolution of the vapor density and temperature (Fig. 3.18) indicate that the condensation begins as soon as the film and the Ar gas are put in contact.

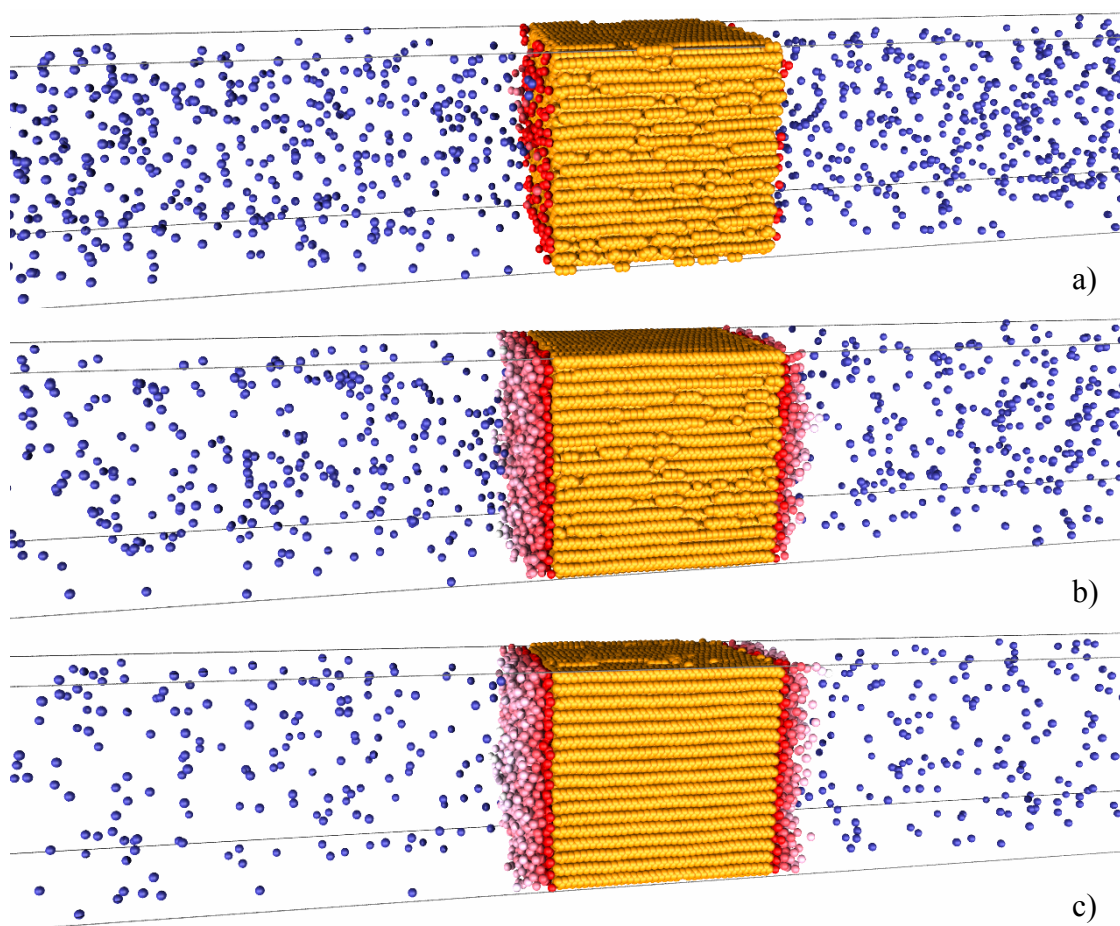


Figure 3.17. Snapshots of the simulation B<sub>3</sub> a) at  $t=100$  ps, the surface is partially wetted b)  $t=4$  ns, more than one layer are absorbed on the polymer film c)  $t=12$  ns an equilibrium between the condensed phase on the surface and the vapor phase has been reached. In orange the constituent CH<sub>2</sub> groups of the polymer film, Ar atoms in vapor are displayed in blue, atoms absorbed on the surface in shades of red; red corresponds to the atoms absorbed on the first layers and their tonalities to the atoms deposited in consecutive layers.

The initial homogeneous gas phase at 200 K cools down by means of the heat exchange with the film surface. The initial increase of about 5 K in the surface

temperature indicates that the vapor condenses close to the surface (Fig. 3.18a). A slight temperature gradient is developed in the film, but its average temperature remains approximately constant. The vapor, surface and film finally converge to the reference temperature of the applied thermostat,  $T_{PE}$ .

The series of simulations performed at a constant value of the temperature of the film, simulations A and B, indicate that the condensation rate is mainly determined by the ratio between the initial vapor density and the equilibrium density at the temperature of the surface  $\rho/\rho_{eq}(T_{PE})$ . The condensation is faster at higher initial vapor densities and lower surface temperatures.

The thermal evolution of the vapor phase is mainly determined by a) the dilution of the vapor phase b) the cooling due to the energy interchange through the atoms that reach the cold polymer surface and return to the vapor and c) the increase of temperature near the surface produced by the condensation.

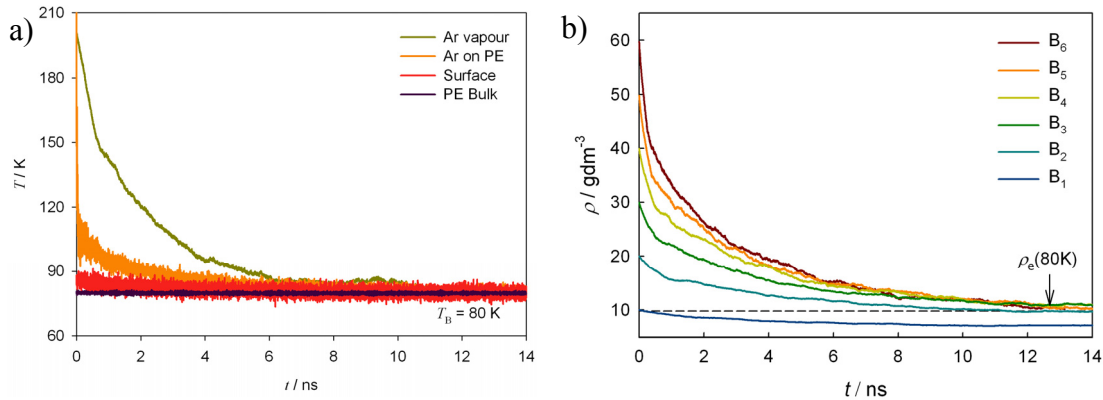


Figure 3.18. a) Evolution of the temperature of the subsystems; PE bulk, exposed surface, Ar atoms in vapor phase and Ar atoms on the surface for the simulation B<sub>3</sub>,  $T_{PE}=80$  K b) evolution of the vapor density for the simulations performed at  $T_{PE}=80$  K.

The temperature and density of the vapor exhibit a similar exponentially decreasing behavior which can be described by the function

$$x_v = x_{v\infty} + (x_{v0} - x_{v\infty})\exp(-\alpha_x t). \quad (3.15)$$

Here  $x$  represents the temperature or the density of the vapor; the initial and stationary values of  $x$  are respectively denoted with the indices 0 and  $\infty$ . The parameters of the vapor temperature and density functions are determined in the first 4 nanoseconds of the simulation Equation (3.15). The similarity between  $\alpha_\rho$  and  $\alpha_T$  indicates a strong correlation between the dilution and the cooling experienced by the vapor. At high

condensation rates the dilution effect dominates at the beginning of the simulation. The vapor experiments a quasi-adiabatic expansion.

Independent of the initial saturation, the vapor density reaches a stationary value after the thermal equilibration,  $t \sim 12$  ns. In all cases it seems to be close to the calculated equilibrium density of Ar with a cut-off  $r_c=2.5\sigma$  at the bath temperature (Fig. 3.18b).

The Figures 3.18 show for the simulation B<sub>3</sub> that the macroscopic bulk properties, such as the temperature of the system and density of the vapor, reach stationary values when only 3 layers are deposited over the film and some atoms are distributed in islands over them (see Fig. 3.19). However, the condensed Ar film is found in the regime where its properties are size-dependent because of its small thickness and the effect of the polymer substrate. Therefore, the reduction of the final vapor density with respect to the equilibrium value of pure Ar in the simulations performed near the binodal (simulation B<sub>1</sub>) can be explained as a displacement of the phase equilibrium due to the finite size of the deposited Ar film, in other words, due to the smaller density of the condensed phase respect its macroscopic bulk value.

For the simulation conditions of saturation, temperature and number of Ar atoms, no more than 5 absorbed layers are observed at the stationary state (see Figs. 3.20) while in all cases the temperature and density have been reached constant values. Snapshots of the simulation B<sub>3</sub> (Fig. 3.17) and density profiles (Fig. 3.21) indicate that at the simulated temperatures the deposited Ar atoms remain on the surface and do not diffuse into the polymer matrix. The snapshots also show that condensation of Ar takes place near the surface by a sequential formation of layers. The evolution of the number of atoms per layer (Fig. 3.20) confirms this observation. The film conserves its semicrystalline structure during the simulation because of the weak PE-Ar interactions.

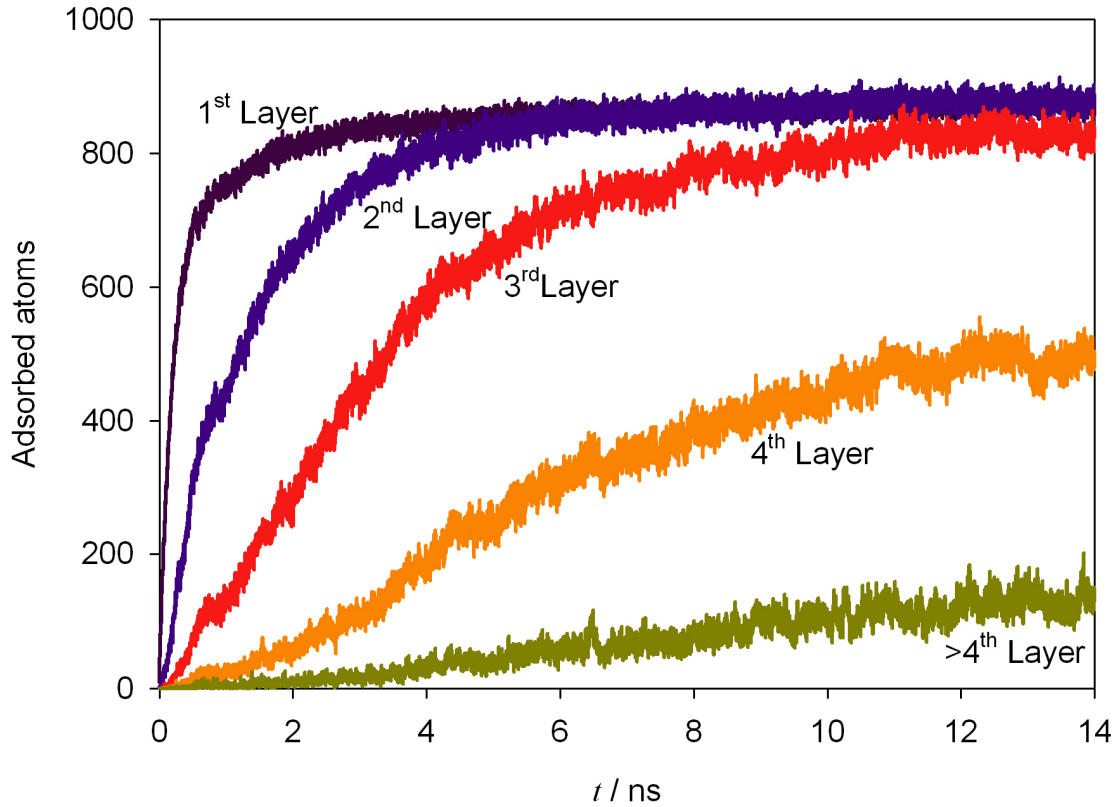


Figure 3.19. Temporal evolution of the number of Ar ad-atoms in the different adsorbed layers for the simulation B<sub>3</sub>. Ar layers consecutively saturate on the surface.

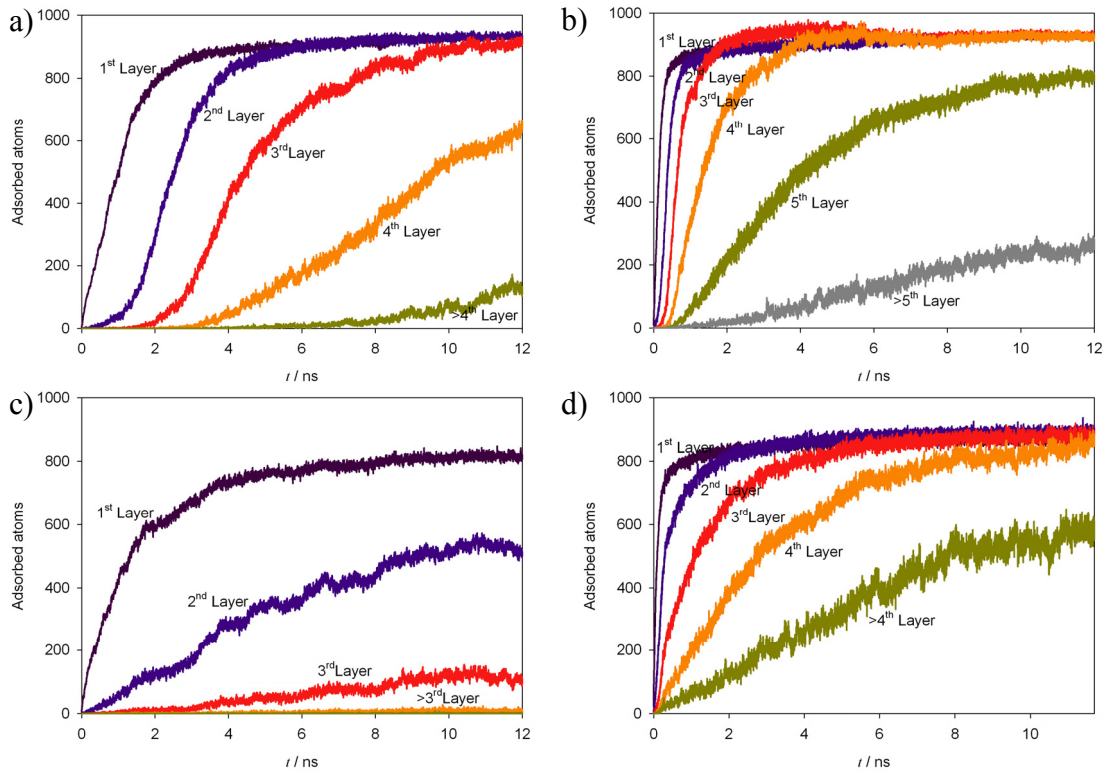


Figure 3.20. Evolution of the number of Ar ad-atoms in the different adsorbed layers at two different bath temperatures; at  $T_{PE}=60$  K a) A<sub>1</sub> low saturation b) A<sub>6</sub> high saturation and at  $T_{PE}=80$  K c) B<sub>1</sub> low saturation d) B<sub>6</sub> high saturation.

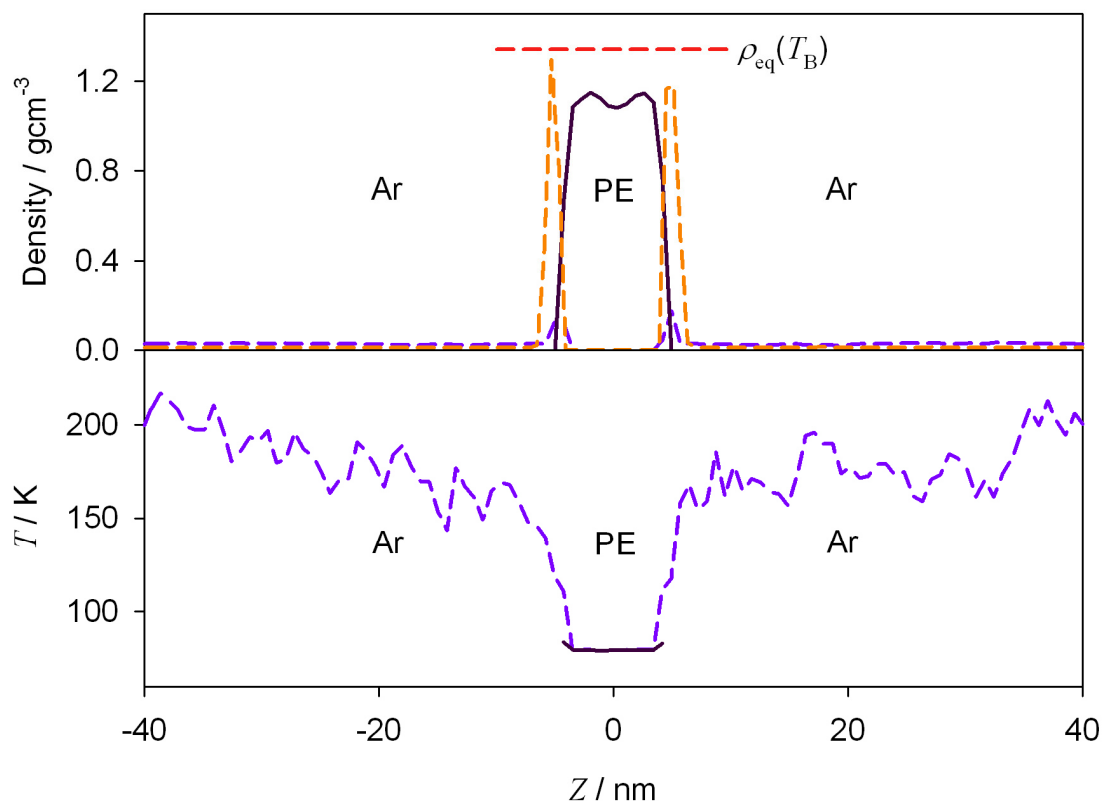


Figure 3.21. Density and temperature profiles  $T_{PE}=80$  K for the simulation B<sub>3</sub> at 1 ns.

Heterogeneous three-dimensional nucleation of a vapor is theoretically possible for saturation ratios higher than 1. According to the temperature and density profiles, presented in the Figure 3.21, the condition imposed by the HEN 3D theory defines for the vapor a narrow spatial region near the surface to condense. The number of clusters of size higher than 3 atoms in bulk of the vapor phase is very low and diminishes in course of the simulation.

The growth mechanism as the shape of the clusters on the surface is mainly determined by the ratio  $\varepsilon_{PE-Ar}/\varepsilon_{Ar}$ , other quantities as the vapor saturation have a minor effect. The ratio  $\varepsilon_{PE-Ar}/\varepsilon_{Ar}$  is about 4.5, which corresponds to a favourable wetting condition. Consistent with the studies of Maruyama *et al.*<sup>134</sup> a layers on layers growth of Ar clusters on the PE surfaces is observed.

The set of simulations B performed at  $T_{PE}=80$  K indicate that the saturation of the vapor phase has an effect on the growth mode (Fig. 3.22). In the regime of low saturation, when the surface is partially covered, the adsorbed atoms condensate preferentially on the first layer. At higher saturations the ad-atoms tend to distribute in higher levels building 3D clusters (Fig. 3.23).



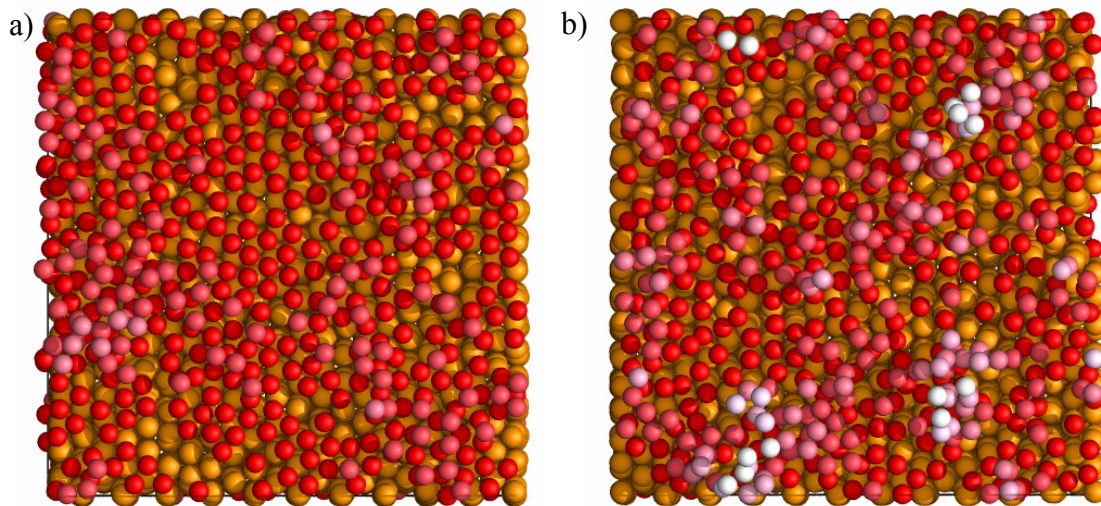


Figure 3.22. Snapshots of the simulations  $B_1$  and  $B_6$ , corresponding to the low and high saturation regimes respectively, at the same amount of absorbed atoms  $N_{\text{surf}}=1000$ . A tendency to the formation of islands on layers is observed at higher saturation.

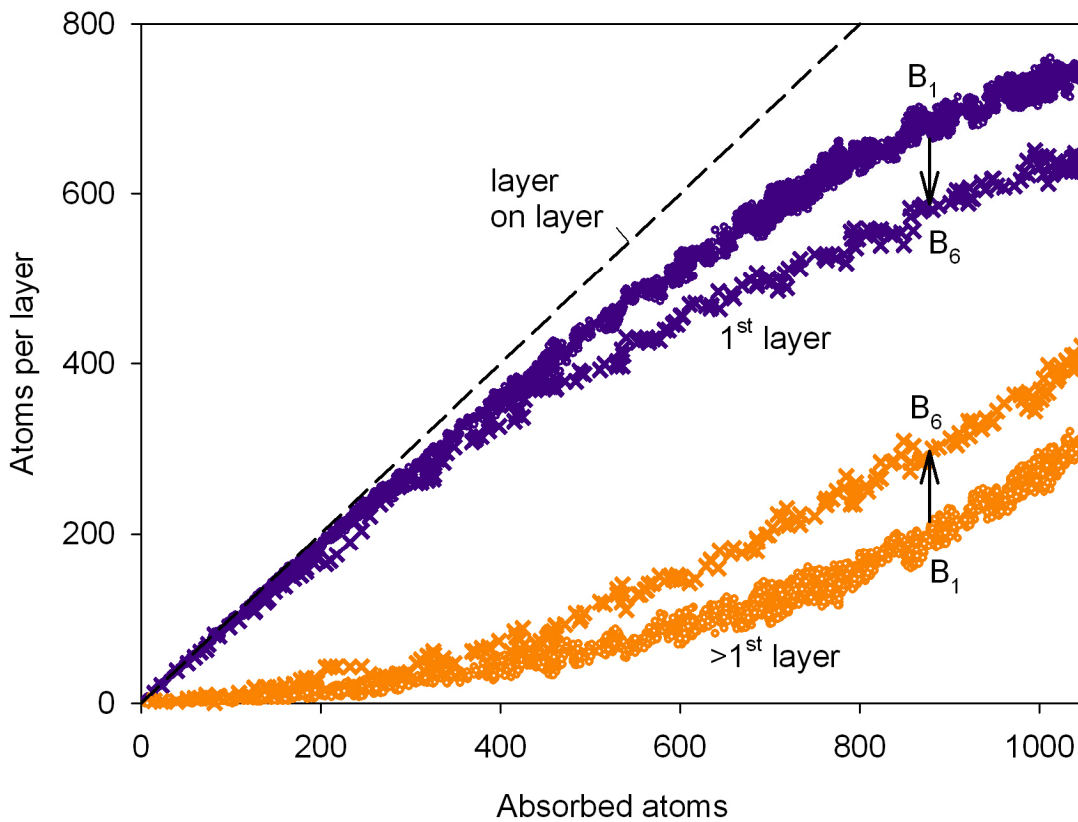


Figure 3.23. Distribution of ad-atoms on the surface for simulations at  $T_{\text{PE}}=80$  K,  $B_1$ ; low saturation and  $B_6$ ; high saturation. As the saturation of the vapor increase the growth mode deviates from the idealized layer-on-layer mechanism. Atoms deposit on higher layers before the first layer saturates.

In case of perfect layer-by-layer growth the number of atoms in the subsequent layers ( $> 1^{\text{st}}$  layer) should be zero until the first layer is completely filled, which corresponds to approximately 870 atoms at 80 K and 920 atoms at 60 K. The nominal area of the substrate surface is slightly different for the simulations at 60 K and at 80 K



( $A'=62.9$  at 60 K and  $A'=63.3$  nm<sup>2</sup> at 80K). Hence the number of atoms per unit area is more suitable for comparison. It is 7.31 atoms/nm<sup>2</sup> at 60 K and 6.87 atoms/nm<sup>2</sup> at 80 K. This difference of about 6.4 % in the two-dimensional concentration of the atoms in the first layer at different temperature is related to the thermal expansion of the liquid. The bulk liquid density  $\rho_1$  calculated here from simulations of equilibrated films for the LJ2.5 $\sigma$  argon are 1480.1 g/dm<sup>3</sup> at 60 K and 1340.8 g/dm<sup>3</sup> at 80 K. In order to compare the difference in the two-dimensional concentration of atoms on the substrate surface to that in the three-dimensional bulk liquid density  $\rho_1$  we have to scale the density as  $\rho_1^{2/3}$ . This relation is exact for a perfect crystal and an approximation for the liquid here. It gives a difference of 5.8 % in density which is comparable to that of the concentration of atoms on the surface.

Curves of density of clusters on the surface versus coverage (Fig. 3.24) indicate that the clusters on the surface coalesce into a single connected island when about 80% of the surface is covered.

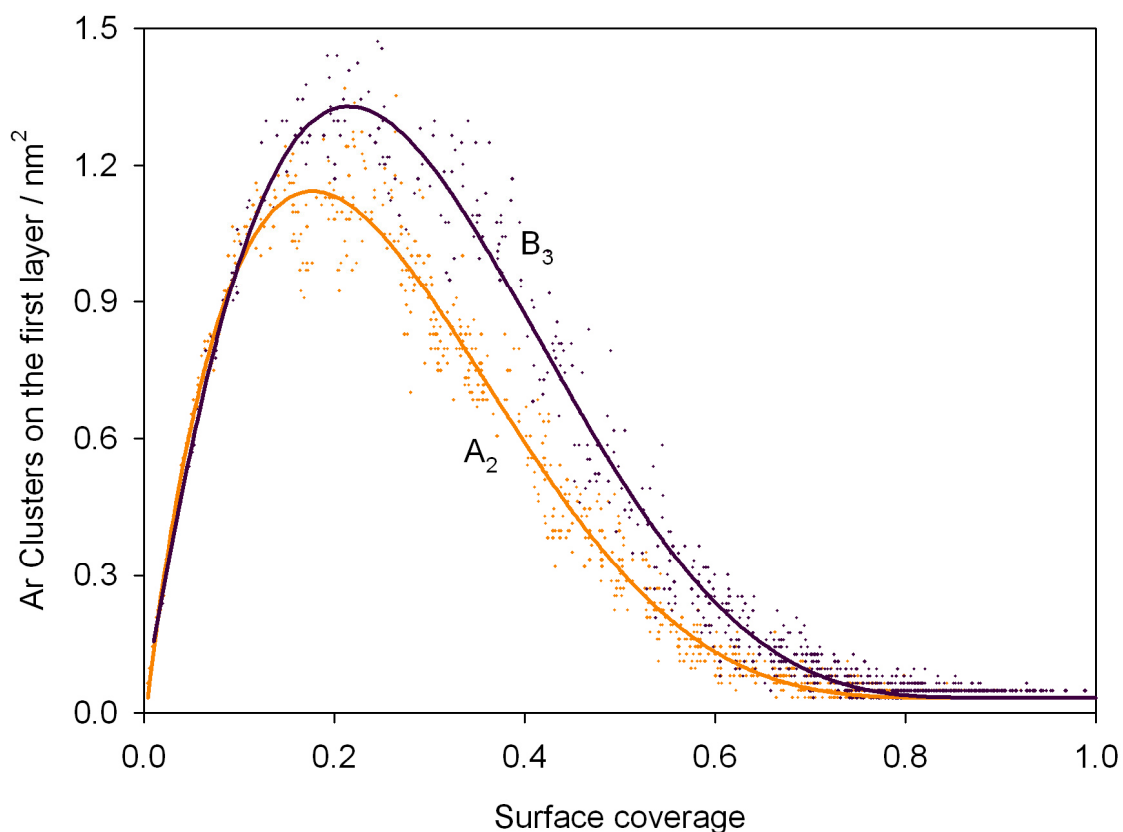


Figure 3.24. Density of clusters in the surface versus coverage for the simulations A<sub>2</sub> and B<sub>3</sub>.

The comparison of the curves for simulations performed for different surface temperatures, but similar nucleation rates (A<sub>2</sub> and B<sub>3</sub>), show a similar behavior at low

coverage, but a notable discrepancy near the zone where the cluster density on the surface reaches a maximum value. The Figure 3.24 suggests an inhibition of the coalescence events at higher surface temperatures, probably related to an increase of the disintegration frequency of smaller clusters.

According to Yasuoka and Matsumoto<sup>138,139</sup> nucleation rates can be calculated from the temporal evolution of the population of clusters larger than a given size  $n_t$ . The curves show four typical regimes; in the first there are no signals of formation of stable clusters bigger than  $n_t$ ; clusters appear and disintegrate on the surface, in the second regime; clusters of size higher than  $n_t$  present a stable growth characterized by an approximately linear behavior, in the next regime the concentration of clusters reaches a maximum value due to the competition between cluster growth and coalescence events, in the last regime the coalescence of clusters prevails over the formation of new clusters due to the dilution of the old phase. As example the cluster growth curves for different thresholds  $n_t$  obtained in the simulation B<sub>3</sub> are presented in the Figure 3.25.

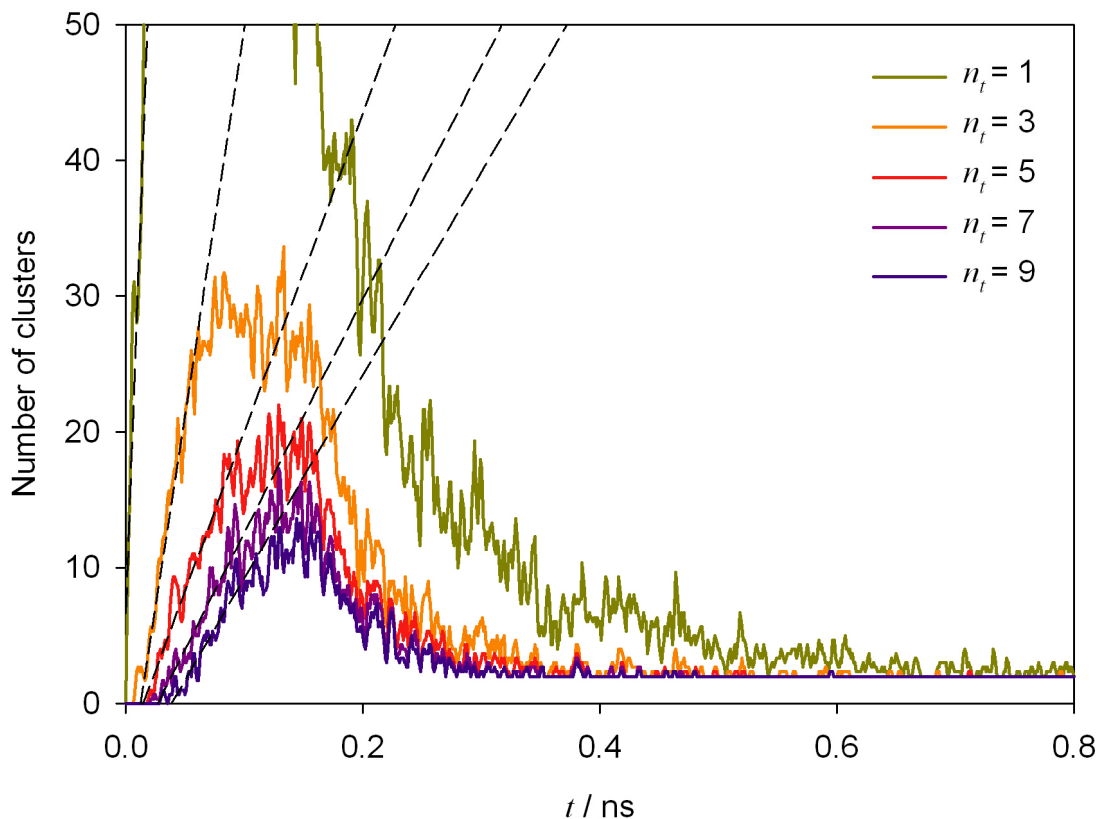


Figure 3.25. Temporal evolution of the population of clusters bigger than a given size  $n_t$  for the simulation B<sub>3</sub>.

Nucleation rates were determined from the slope  $m$  of the linear adjustment in the second growth regime, expressed by surface unit  $J=m/A$ . The slope presents a

decreasing behavior as  $n_t$  increases and converges to a constant value at a given threshold (Fig. 3.26). The application of the method of Yasuoka and Matsumoto<sup>138,139</sup> is problematic in the extremes of low and high nucleation rates when it is applied to a small finite surface. At high nucleation rate the second regime of the growth curves occurs in a short period due to the early coalescence of the clusters into a single layer. At low nucleation rates the slope  $m$  converges to a given value for a threshold  $n_t$  similar or higher than the amount of sites on the surface. Both difficulties can be avoided by increasing the size of the surface. The simulation of larger substrates requires more computations, for this reason simple force fields to model the polymer substrate are preferred.

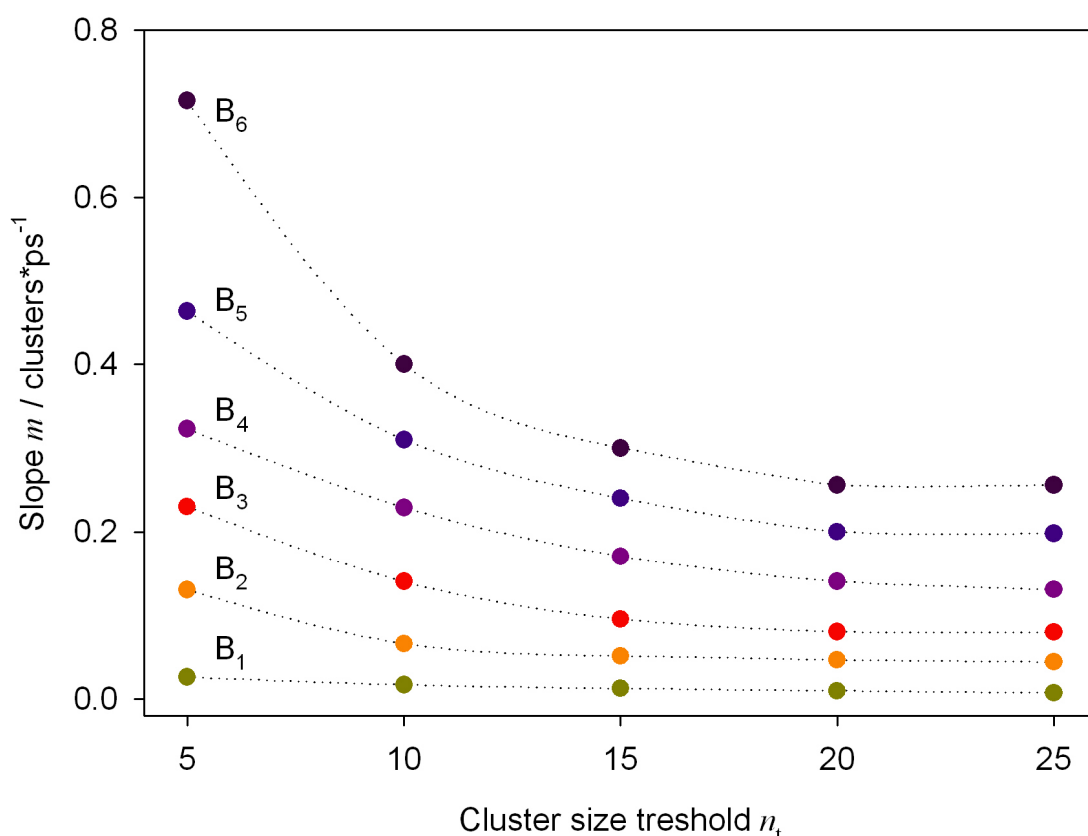


Figure 3.26. Slope values of the growth curves versus threshold  $n_t$  for the simulations at  $T_{PE}=80$  K. The slope presents a decreasing behavior and converges for a given threshold  $n_t$ .

The results of simulation are compared with the classic theory presented in the Section 1.1.5. No long-range corrections to the force are introduced in the simulations. In order to establish a consistent comparison between the theory and the simulation the equilibrium properties; densities of liquid and vapor and interfacial tension, of truncated Ar are used in the Equations (1.24) and (1.26). Furthermore, all the impinging

monomers are assumed to attach to the cluster surface. The supersaturation is approximated as  $S = \rho / \rho_e$  and the surface density of active sites as  $C_0 = \rho^{2/3}$ .

The theory was locally applied in the region close to the surface where the vapor condensates. The condensation temperature is defined as the temperature of the Ar atoms and CH<sub>2</sub> groups located at the surface of the film. In contrast to the Szilard's experiment<sup>28</sup>, the temperature of the surface as well as the density of the vapor phase change during the simulation. Time averaged values of these variables, calculated on the time interval of the linear second regime of the clusters growth curves, are used to report the  $J$ - $S$  simulation results.

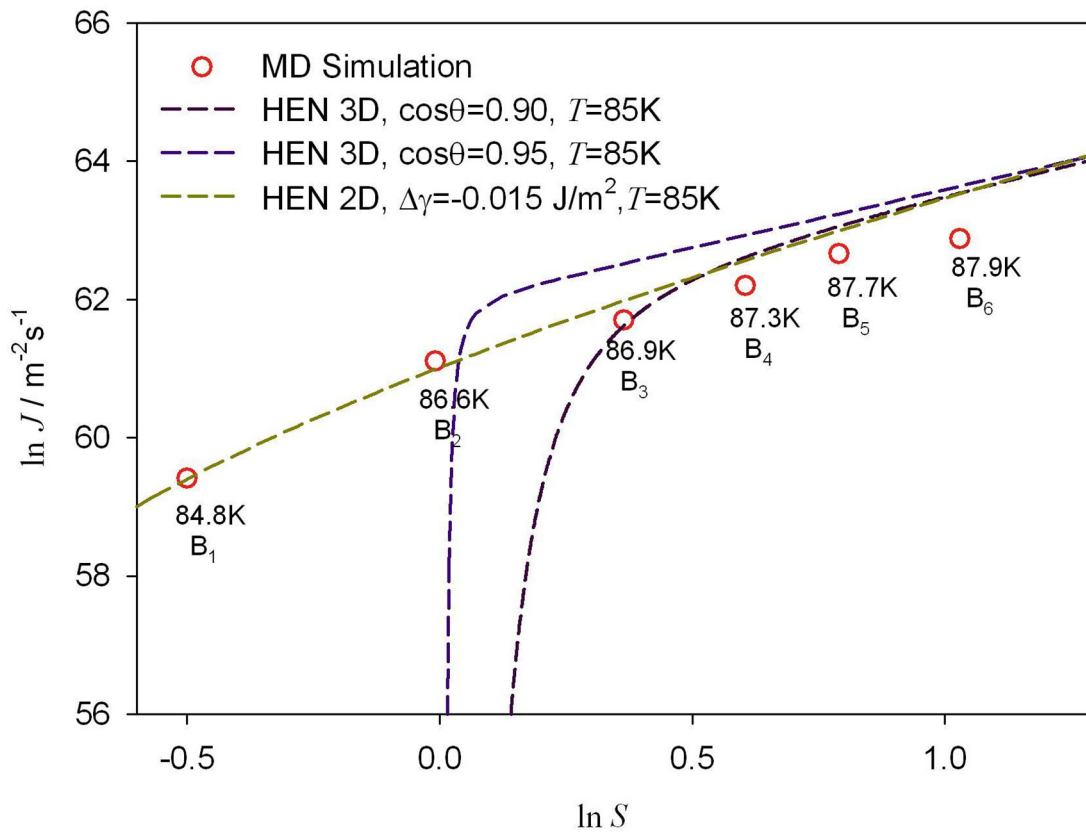


Figure 3.27. Comparison of the nucleation rates obtained from simulation at  $T_{PE}=80$  K and the HEN 3D and HEN 2D models. The HEN 3D model is applied using the contact angle as adjusting parameter, low contact angles provide a better fit at low saturation.

Simulation results at  $T_{PE}=80$  K indicate that the condensation continues for saturation ratios lower than 1. Even for an undersaturated initial vapor, B<sub>1</sub>, condensation occurs (see Fig. 3.27). According to the observed growth mode and to the spatial distribution of the Ar atoms on the surface the three-dimensional HEN model at high wettability (low contact angles) should represent the nucleation rates obtained from simulation. The results presented in the Figure 3.27 corroborate this observation, the

range of application of the HEN 3D model wide as lower contact angles are used in the Equation (1.24). The HEN 2D and the HEN 3D (for low contact angles) models show a similar behavior at high saturation. This suggests that the nucleation rate turns less sensible to the growth mechanism as the saturation increases. Nevertheless, at low saturation the three-dimensional growth model predicts a fast decay of the nucleation rate, while the simulation results maintain the trend of the high saturation regime.

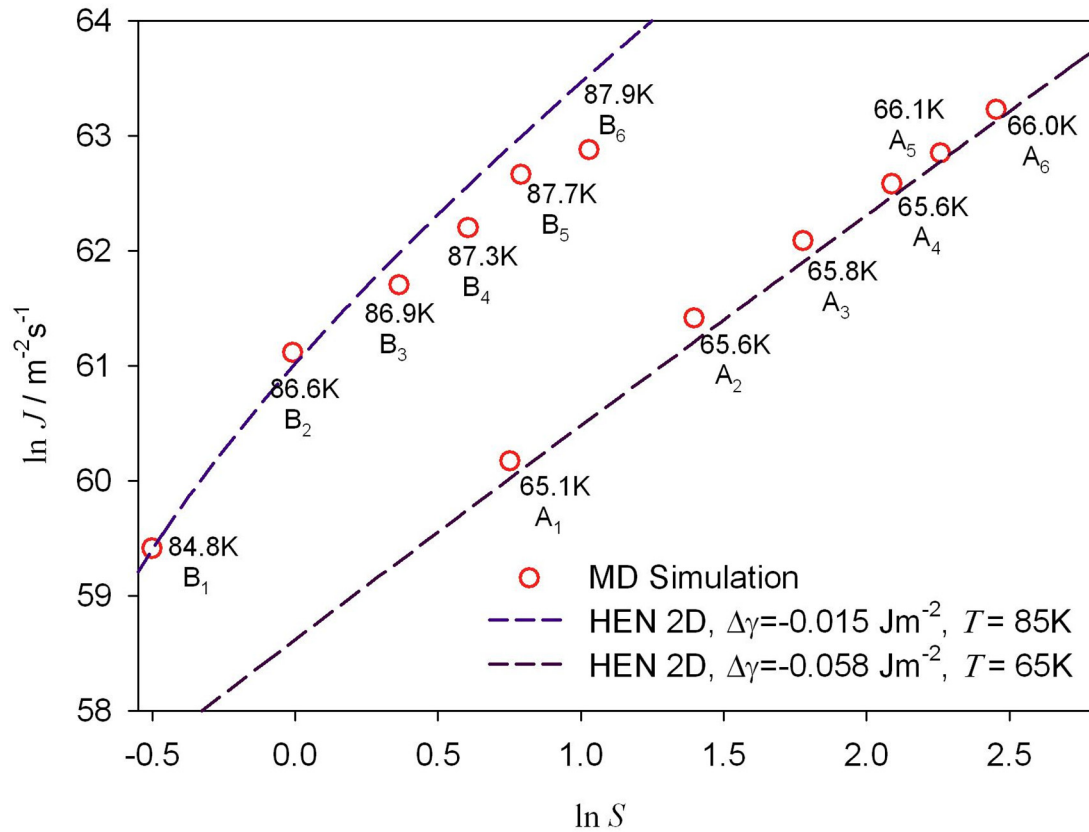


Figure 3.28.  $J$ - $S$  data at different temperatures. The model HEN 2D extends the range of application of the classical nucleation theory to the limit of low saturation and undersaturated vapors.

The HEN 2D model seems to be suitable to explain the nucleation observed outside the metastability region of the phase diagram,  $S < 1$ , where the HEN 3D model cannot be applied (Fig. 3.28).

Moreover, when the relative interaction between the surface and the ad-atoms is strong enough in comparison to the interaction between ad-atoms in a cluster, the contact angle defined in the Young relation loses its usual meaning; the surface is wetted 'better than complete'. The specific surface energy  $\Delta\gamma$  defined by (1.11) turns to be the relevant parameter to describe the trend of the  $J$ - $S$  data.

The dependence of the effective specific surface energy of clusters  $\Delta\gamma$  on the temperature (see Fig. 3.28) can be interpreted in terms of the Dupré relation<sup>9</sup>

$$\Delta\gamma = 2\gamma - \beta_a. \quad (3.16)$$

Here  $\beta_a$  denotes the specific adhesion energy of a cluster at the surface. The specific energy of the interface between liquid clusters and the vapor decreases at higher temperature, while the adhesion energy remains almost constant.

### 3.3 Condensation of Pt on PE Films

One approach for producing disperse materials and composite materials is the deposition of metal from the vapour phase on polymer substrates. In this process the metal does not only deposits on top of the substrate, it also penetrates it and forms particles inside the polymer matrix. Here the deposition of supersaturated platinum vapour on and in polyethylene films is investigated. In the Section 3.2 the growth dynamics of Ar films on polyethylene substrates was studied. The fundamental characteristic of this system is the similarity in the weak cohesive energies between the ad-atoms and between the monomer units of the polymer. The study is extended in this Section to the condensation of metal atoms in presence of a polymer films. In contrast to the system PE-Ar, the cohesive energy between atoms in a metal are about one magnitude orders higher than the ones between the monomers in a polymer. On the other hand, the interactions between polymers and metals, as platinum, are very weak in comparison to the interactions between metal atoms<sup>23</sup>.

#### 3.3.1 Simulation Methodology

Simulations of condensation of Pt atoms on a polyethylene substrate in presence of Ar, used as carrier gas, were performed by molecular dynamics. Polyethylene films, consisting of 374 linear chains of 70 methyl groups each, were first prepared by the method described in the Section 3.1.3.2. The film was previously annealed over  $T_g$  and then equilibrated at  $T_{PE}=200$  K, which is lower than its glass transition temperature. The dimensions of the film surface are  $8.4 \text{ nm} \times 7.9 \text{ nm}$  and its nominal thickness is about 8 nm. The equilibrated film is put in contact with an initial vapor phase consisting of 4950

platinum atoms and 1650 Ar atoms randomly located in the points of an orthorhombic lattice. The initial velocities of Ar and Pt atoms are independently assigned according to a Boltzmann distribution at the same temperature of the equilibrated film. Simulations at three different densities of the vapor phase were performed maintaining the ratio Pt:Ar constant at a value of 3:1. The initial conditions of the performed simulations are summarized in the Table 3.3.

Sim.	$T_{\text{Pt}} / \text{K}$	$T_{\text{Ar}} / \text{K}$	$T_{\text{PE}} / \text{K}$	$\rho_{\text{Pt}} / \text{gcm}^{-3}$	Pt:Ar
C <sub>1</sub>	200	200	200	0.010	3:1
C <sub>2</sub>	200	200	200	0.050	3:1
C <sub>3</sub>	200	200	200	0.100	3:1

Table 3.3. Initial conditions for the simulations of condensation of Pt on PE films in presence of Ar as carrier gas

The condensation heat is removed by a Nosé Hoover thermostat applied to the polymer film only. The temperature of the thermostat is higher than the critical temperature of the carrier gas and lower than the glass transition temperature of the polymer film. With this setup inspired by the experiment conditions, the temperature of the vapour phase is regulated only by collisions of the argon atoms with the polymer substrate. The Nosé-Hoover thermostat is applied to the film at  $T_{\text{PE}}=200$  K during the simulation, using a mass parameter  $Q$  given by the Equation (3.14). Newton's equations of motion for Pt and Ar atoms and Nosé-Hoover equations for the CH<sub>2</sub> groups are integrated with the Störmer-Verlet method using an integration step  $\Delta t=1$  fs. The boundaries of the box simulation are rigid, and full periodical boundary conditions are used.

Clustering phenomena and properties of the vapor phase, PE surface and bulk PE are separately monitored. For this purpose the following definitions were used: a) PE film surface are the CH<sub>2</sub> groups recognized by the cone method<sup>140</sup> described in Appendix A.4, using an angle  $\varphi_c=22.5^\circ$ , b) a cluster is on the polymer surface when least one of its atoms is in contact with a superficial CH<sub>2</sub> group, c) a cluster is in bulk when least one of its atoms contact a CH<sub>2</sub> group excluding the CH<sub>2</sub> groups on the surface, d) in other case the cluster is in the vapor. The cut-off distance to determine if an atom is in contact with a CH<sub>2</sub> group is defined as  $1.5\sigma_{ij}$ , where the index  $i$  denotes a CH<sub>2</sub> group and  $j$  a Pt or Ar atom (values of  $\sigma_{ij}$  are presented in the Table 3.7).

### 3.3.1.1 EAM Model for Platinum

The EAM parameters reported by Foiles<sup>141</sup> were used to calculate interactions between Pt atoms. The effective charge  $Z$  for Pt is represented by the function (3.17), while the embedding energy  $F(\rho)$  is reported as spline knots in the Table 3.6. The electron density is calculated by means of the Equations (2.79) and (2.80) using the parameters of the double  $\xi$ - wave functions given in the Table 3.4.

$$Z(r) = \left( a_1 (r_c - r)^3 + a_2 (r_c - r)^4 \right)^{1/2}, \text{ for } r < r_c. \quad (3.17)$$

$i$	$n_i$	$\xi_i / a_B^{-1}$	$C_i$
6s			
1	1	79.402892	-0.000488
2	1	53.779044	-0.012378
3	2	38.543151	-0.089225
4	2	36.021430	0.132152
5	3	25.026993	0.045720
6	3	20.137187	-0.143352
7	4	12.671444	0.068599
8	4	9.817353	0.114209
9	5	6.337861	-0.265424
10	5	4.198240	0.003540
11	6	2.428978	0.543558
12	6	1.324793	0.590631
5d			
1	3	30.756823	-0.021398
2	3	19.447468	-0.137188
3	4	12.546540	0.221365
4	4	8.325918	0.132240
5	5	4.760262	-0.633997
6	5	2.446933	-0.534361

Table 3.4. Parameters of the double  $\xi$ -wave functions of platinum<sup>115</sup> ( $a_B=0.5292 \text{ \AA}$ , Bohr radius).

$n_s$	$n_v$	$r_c / \text{nm}$	$a_1 / \text{e}^2 \text{nm}^{-3}$	$a_2 / \text{e}^2 \text{nm}^{-4}$
0.96	10	0.33459	65.699	1109.51

Table 3.5. Parameters  $n_s$ ,  $n_v$ ,  $r_c$ ,  $a_1$  and  $a_2$  for the calculation of the electron density and the effective charge of Pt.<sup>141</sup>

$\rho / \text{nm}^{-3}$	0.000	11.400	22.800	45.600	52.445
$F(\rho) / \text{eV}$	0.0000	-4.5793	-6.5328	-6.5328	0.0000

Table 3.6. Embedding energy as function of the electron density of Pt.<sup>141</sup>



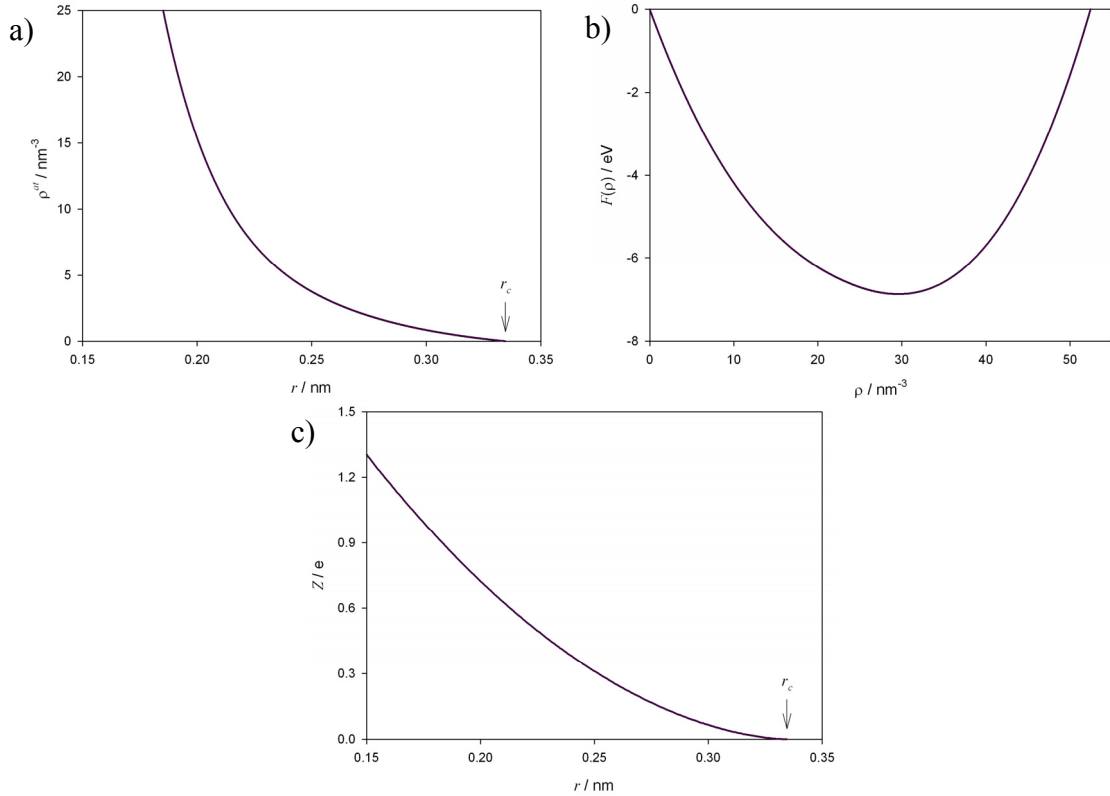


Figure 3.29. Functions of the EAM potential for Platinum: a) electron atomic density versus distance b) embedding function versus electronic density and c) effective charge versus distance.

### 3.3.1.2 Cross Interactions in the System PE-Pt-Ar

For the present simulations crossed interactions PE-Ar, Pt-Ar and PE-Pt are approximated by a Lennard Jones potential using Lorentz-Berthelot combining parameters.

The Lennard Jones parameters for platinum were determined from the lattice constants at normal temperature and the cohesive energy  $E_{\text{coh}}$  of platinum<sup>142</sup>. The cohesive energy can be computed from the Lennard Jones 12-6 potential (2.71) and the following expression

$$E_{\text{coh}} = \frac{1}{2} \left[ \sum_j U_{ij}^{\text{nb}} + U_c(r_c) \right]. \quad (3.18)$$

$U_{ij}$  denotes the LJ interactions between an arbitrarily selected atom  $k$  in the crystal and its neighbors, the sum extends over all atoms within a distance  $r_c$  from  $k$ . The crystal model used in evaluating the Equation (3.18) was enough large that no neighboring atoms within the range of  $r_c$  from atom  $k$  is missing. The tail correction to the potential

$U_c$  is the sum of interactions between the atom  $k$  and the atoms beyond the cut-off radius  $r_c$  and is expressed as

$$U_c(r_c) = \frac{16\pi}{3} \rho \varepsilon \sigma^3 \left[ \frac{1}{3} \left( \frac{\sigma}{r_c} \right)^9 - \left( \frac{\sigma}{r_c} \right)^3 \right]. \quad (3.19)$$

The resulting parameters for platinum are  $\sigma=0.2471$  nm and  $\varepsilon=0.694$  eV. The Lorentz-Betherlot cross parameters for the interactions PE-Ar, Pt-Ar and PE-Pt are given in the Table 3.7.

$i-j$	$\sigma_{ij} / \text{nm}$	$\varepsilon_{ij} / \text{eV}$
PE-Ar	0.365	$7.27 \cdot 10^{-3}$
Pt-Ar	0.294	$8.47 \cdot 10^{-2}$
PE-Pt	0.319	$5.95 \cdot 10^{-2}$

Table 3.7. Lorentz-Berthelot cross parameters for the system PE-Pt-Ar

### 3.3.2 Results

In the first picoseconds after the polymer film and the vapor are put in contact Ar and Pt atoms begin to condense on the polymer surface (see Fig. 3.30a).

No observable large clusters are present on the system in this stage. Some of the Pt atoms diffuse into the polymer (see Fig. 3.31b), while Ar atoms adsorb and remain on the surface. After this latency period,  $t > 100$  ps, the size and amount of Pt clusters in vapor phase continuously increase mainly by addition of monomers and small clusters (Figs. 3.31). Metal clusters reach the polymer and embed on it; they show a low mobility on the surface. The surface remains partially wetted during the simulations (see Figs. 3.30 and 3.31).

The size of the clusters deposited on the surface increases by the condensation of clusters in vapor phase on them. The diffusion front of Pt atoms in PE advances as the concentration of Pt on the surface increase. The morphology of the polymer surface modifies as the clusters embed on it (Figs. 3.31).

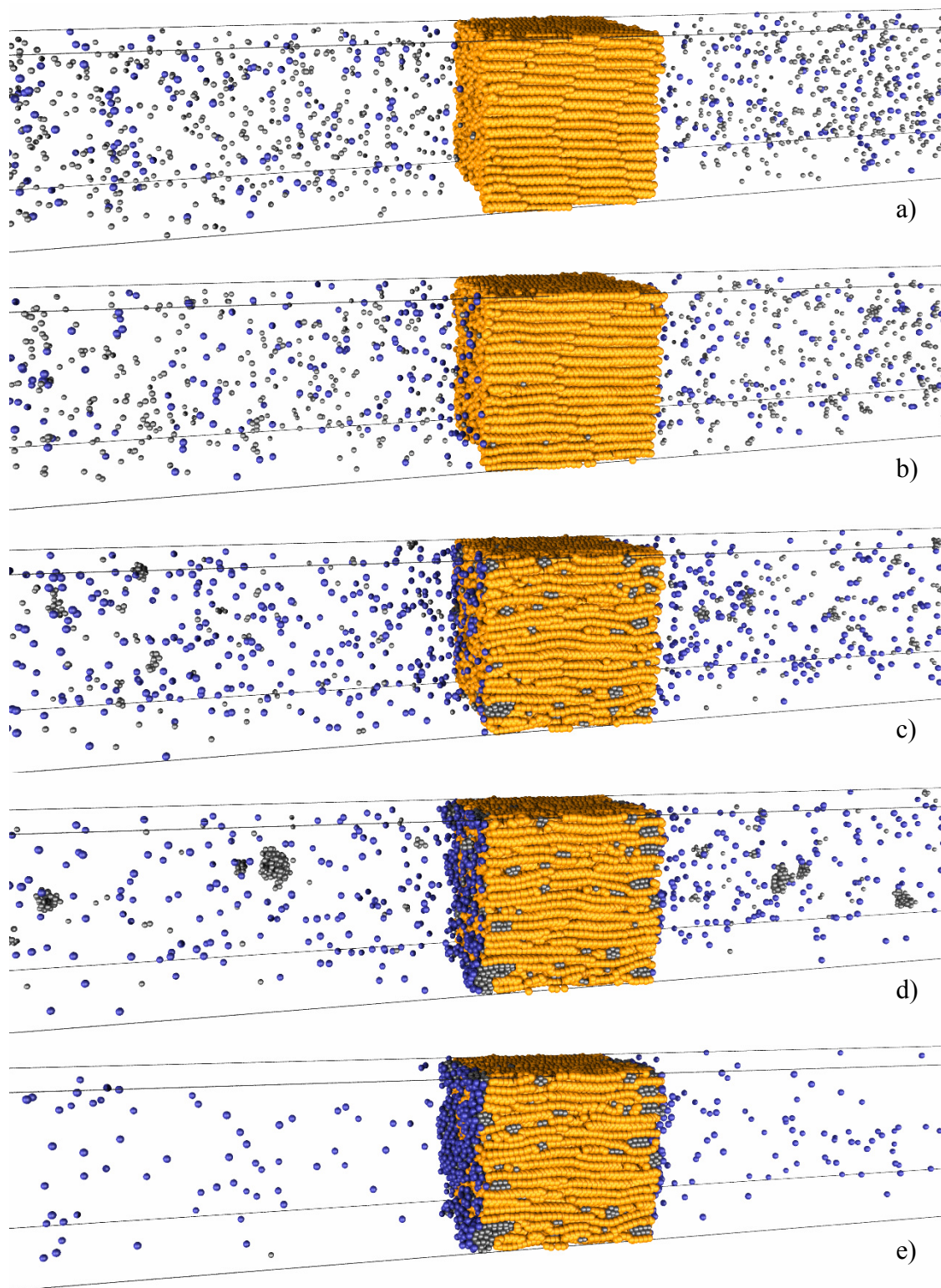


Figure 3.30. Snapshots of the simulation  $C_3$  a) at  $t=10$  ps b)  $t=100$  ps c)  $t=500$  ps d)  $t=1$  ns and e)  $t=5$  ns. The constituent  $\text{CH}_2$  groups of the polymer film are displayed in orange, Ar atoms in blue and Pt atoms are shown in grey. Diffusion of Pt atoms inside the polymer is observed, while Ar atoms tend to build a monolayer on the Pt clusters located on the polymer surface.

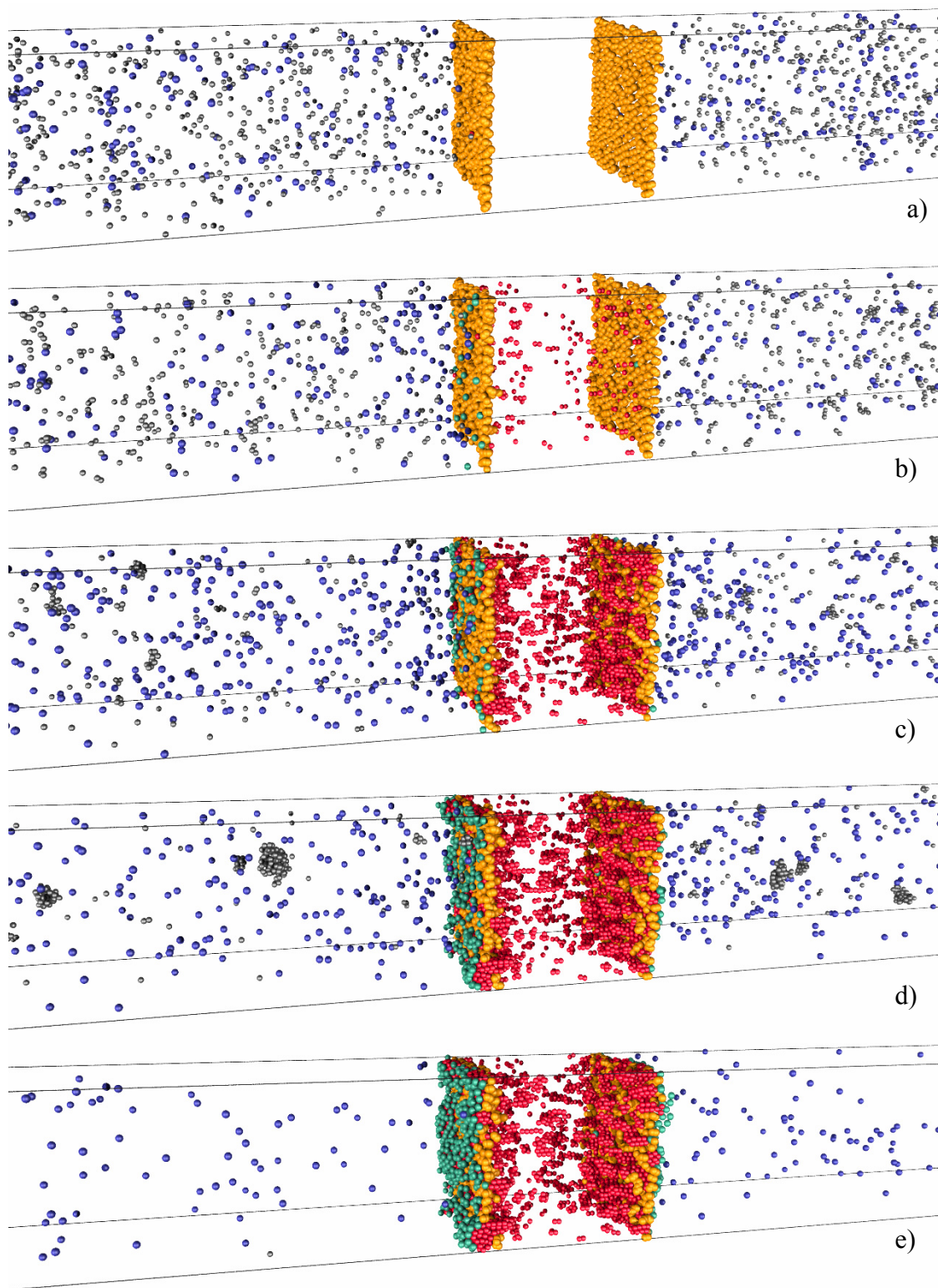


Figure 3.31. Details of the snapshots displayed in Fig 3.30, simulation C<sub>3</sub>. a) at  $t=10$  ps b)  $t=100$  ps c)  $t=500$  ps d)  $t=1$  ns and e) 5 ns. The CH<sub>2</sub> groups in bulk of PE are omitted to observe the distribution of the Pt atoms inside the polymer matrix. CH<sub>2</sub> groups on the PE surface are displayed in orange, Pt and Ar atoms in vapor phase are respectively displayed in grey and blue, Ar atoms on PE are shown in green and Pt in PE bulk and on the PE surface are displayed in red.



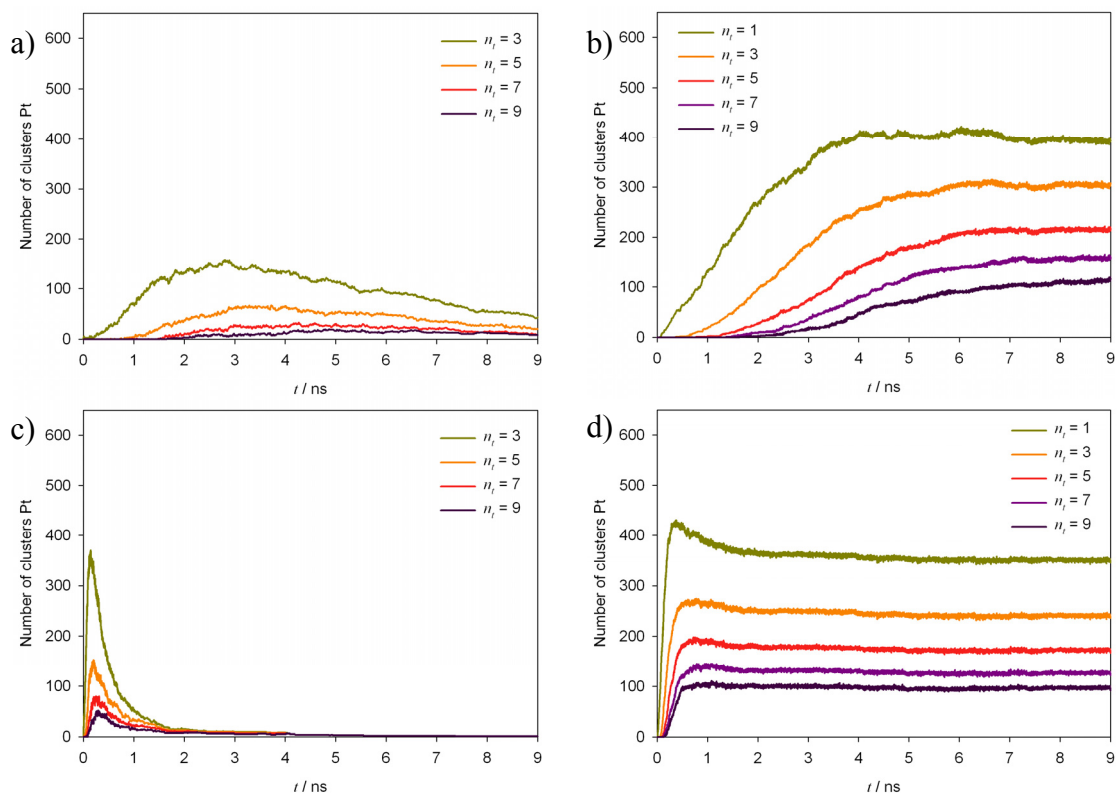


Figure 3.32. Evolution of the number of clusters larger than a given threshold  $n_t$  at low (simulation C<sub>1</sub>) and high saturation (simulation C<sub>3</sub>). For the simulation C<sub>1</sub>: a) In vapor and b) in polymer film. For the simulation C<sub>3</sub>: c) In vapor and d) in polymer film.

The cluster growth curves of clusters in vapor, presented in the Figure 3.32a for the simulation C<sub>1</sub> and in the Figure 3.32c for the simulation C<sub>3</sub>, show the typical behavior of a nucleation process: a initial latency period where clusters form and disintegrate, a stable growth phase, a plateau and finally a decrease produced by coalescence of clusters and dilution of the vapor phase. The growth curves of clusters located inside the polymer is presented in Figure 3.32b for the simulation C<sub>1</sub> and in Figure 3.32d for simulation C<sub>3</sub>. In comparison to the curves obtained for the deposition of Ar on PE they show a different behavior. They reach a maximum and then decrease until reaching a plateau. It indicates that the coalescence processes of the deposited metal clusters are inhibited in the polymer.

On the other hand, for a given threshold  $n_t$  the slopes of the curves in the regime of stable growth are higher in the polymer than in the vapor phase. The difference is higher at low saturation. These results suggest that some Pt clusters agglomerate as they diffuse into the bulk polymer. The coalescence of clusters ends as the free volume in the polymer film is filled (see Figs. 3.31).

The temperature of Pt and Ar show a similar behavior; they reach a maximum and then slowly decrease until reaching temperature of the thermostat (see Fig. 3.33).

The polyethylene film experiences a comparatively small increase of temperature as the first Pt clusters condense on it. The fast response of the film temperature obeys to the action of the thermostat.

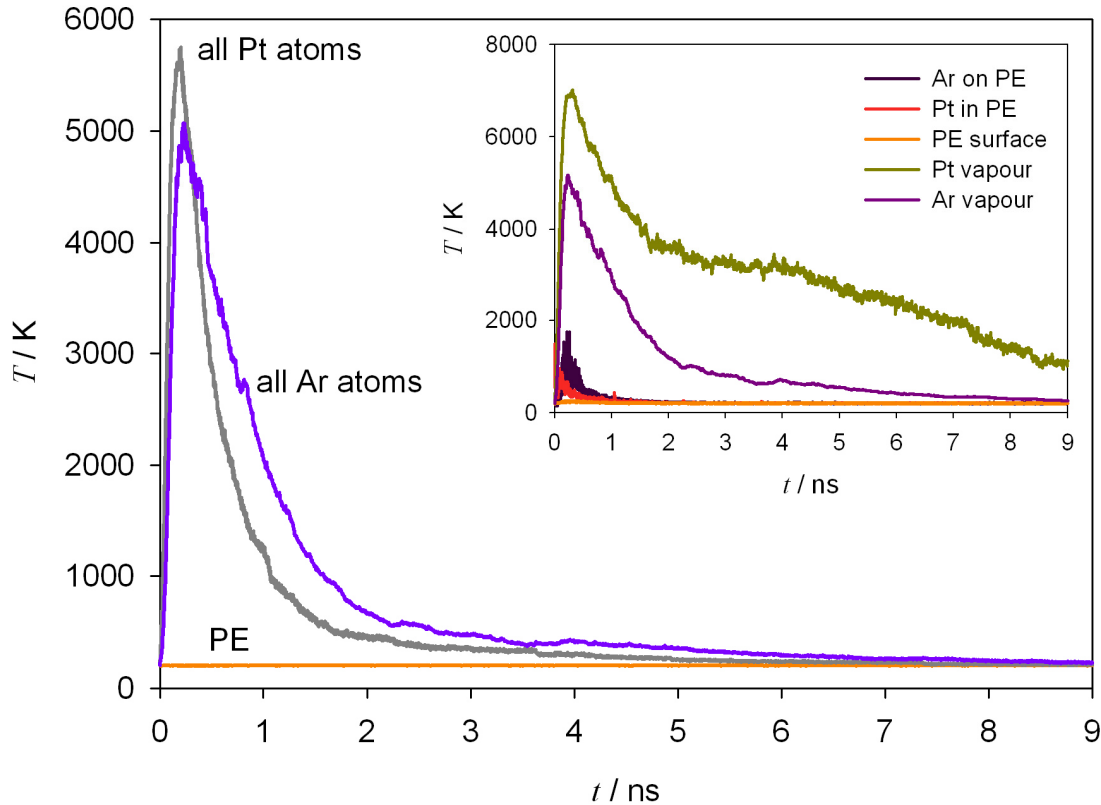


Figure 3.33. Thermal evolution of the system PE-Pt-Ar for the simulation  $C_3$ .

The maximum temperature observed in the simulations  $C_1$  to  $C_3$  is directly related to the initial density of Pt in vapor phase. This fact can be explained by a simple argument, at higher saturation the nucleation, heat generation and condensation rates increase, therefore, higher maximum values of temperature are reached in shorter time.

The maximum temperature reached during the nucleation is also related to the amount of carrier gas. The high temperatures observed in the simulations can be explained by the low ratio Ar:Pt here used<sup>88,89</sup>.

The maximum values of temperature of Pt and Ar in vapor phase are much higher than their correspondent values on the surface (Fig. 3.33). On the other hand, the thermal history of Ar and Pt in vapor seems to be strongly related to the evolution of the temperature of Ar atoms on the surface. Their temperatures reach a maximum in similar time intervals and then slowly decrease. The thermal response of the Pt atoms deposited on the PE surface is much faster, while the heat on the PE surface is quickly removed by the thermostat. These results indicate that the action of the thermostat on the atoms

deposited on the surface is fast. The effectivity of the thermostat is higher in the case of Pt as in the case of Ar. Comparatively the cohesive energy CH<sub>2</sub>-Pt is about 10 times stronger than the CH<sub>2</sub>-Ar (see Table 3.7).

The Figures 3.30 and 3.31 indicate that the Pt clusters which condense on the PE surface either remain adsorbed on it, are captured by clusters deposited on the surface or diffuse into the polymer. The Ar atoms, however, are temporarily adsorbed on the surface and return to the vapor. Then, the later cooling of the vapor phase is mainly produced possible by the exchange of Ar atoms on the surface.

The amount of Pt atoms which diffuse into the polymer appears to be related to the accessible free volume of the polymer and indirectly to the saturation of the vapor phase. Large clusters cannot diffuse deeply into the polymer. The clusters deposited on the surface do not suffer disintegration processes due to the strong cohesive forces between the metal atoms, but their shapes change as they fill the accessible volume created between chains on the PE surface.

The final density of the Pt atoms in vapor is almost independent of its initial value, it is mainly determined by its equilibrium value at the temperature of the film (Fig. 3.34). The Ar atoms tend to build a monolayer over the Pt atoms exposed on the surface (see Fig. 3.31). Thus the final density of Ar in vapor phase depends on the film surface wetted by platinum (Fig. 3.35).

The polymer matrix saturates before the condensation on the film surface reaches a stationary state. The maximum number of Pt atoms inside the polymer is very similar for the simulations C<sub>2</sub> and C<sub>3</sub>, corresponding to high saturations, but is higher for the simulation C<sub>1</sub> at low saturation (Fig. 3.36).

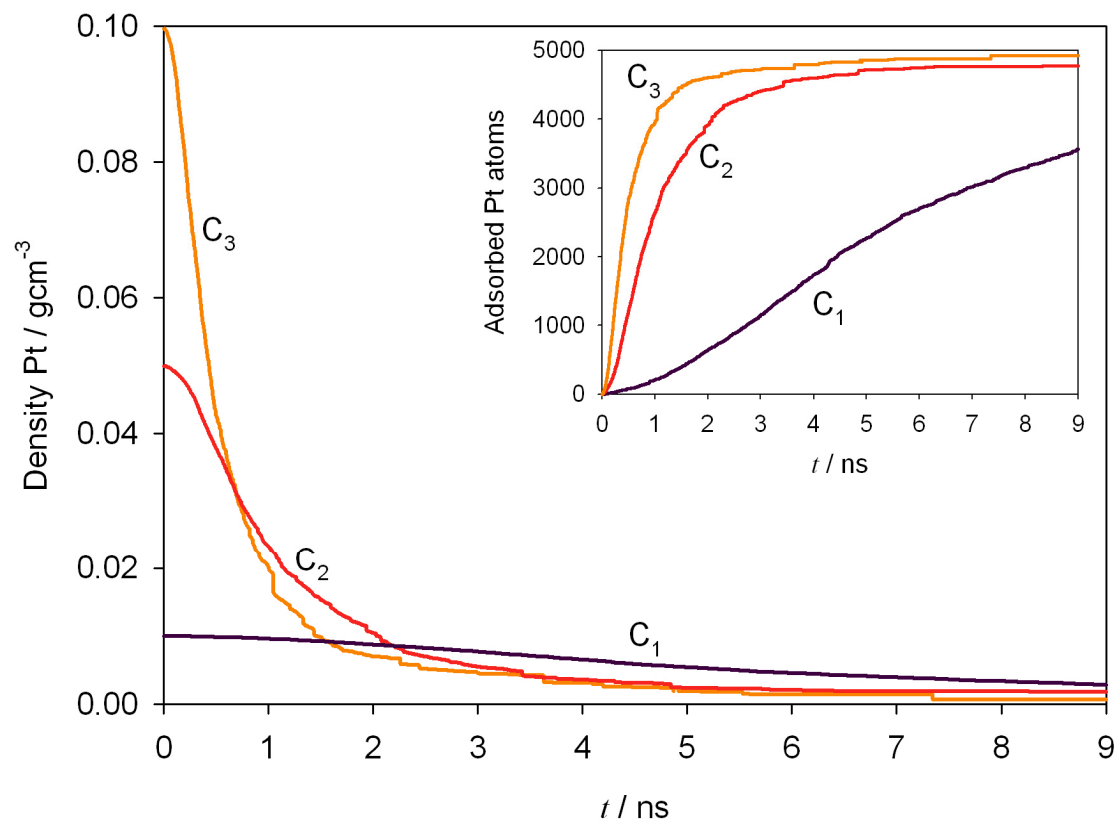


Figure 3.34. Evolution of the density of Pt in vapor phase and number of Pt atoms in PE at three different saturations; simulations  $C_1$ ,  $C_2$  and  $C_3$ .

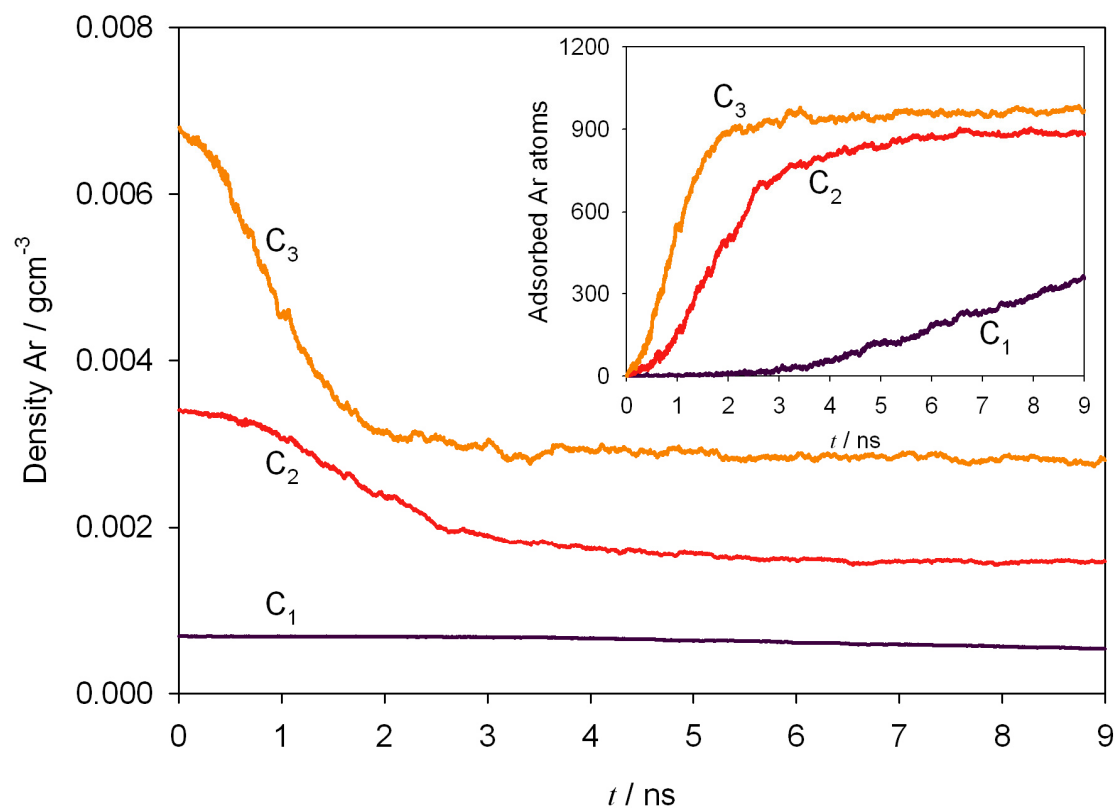


Figure 3.35. Evolution of the density of Ar in vapor phase and number of Ar atoms deposited on the PE-Pt surface.



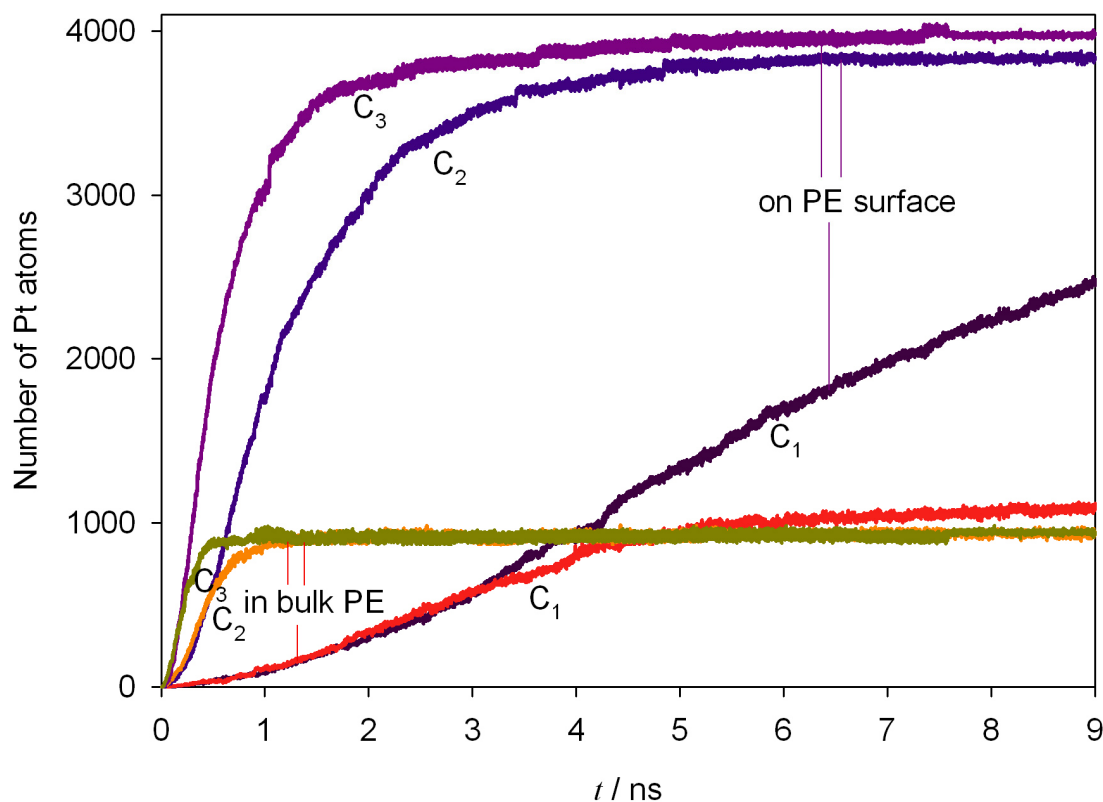


Figure 3.36. Evolution of the number of atoms deposited on the surface and the atoms in bulk polymer for the simulations  $C_1$ ,  $C_2$  and  $C_3$ .

Size distributions of the Pt clusters into the PE bulk and on the PE surface were determined for the simulation  $C_3$  at  $t > 10$  ns, where the system has reached a stationary state. The distributions (Fig. 3.37) indicate that smaller clusters,  $n < 10$ , tend to distribute preferentially in the polymer bulk. Some of clusters of size between 10 and 20 atoms are found in the polymer bulk but clusters larger than 20 atoms remain on the PE surface.

A further analysis reveals the effect of the saturation of the vapor on the distribution of the Pt atoms in the polymer. At low saturation, simulation  $C_1$ , more atoms diffuse into the polymer bulk (Fig. 3.38). This result suggests a relation between the nucleation rates of Pt in vapor and the diffusion of Pt clusters into the polymer.

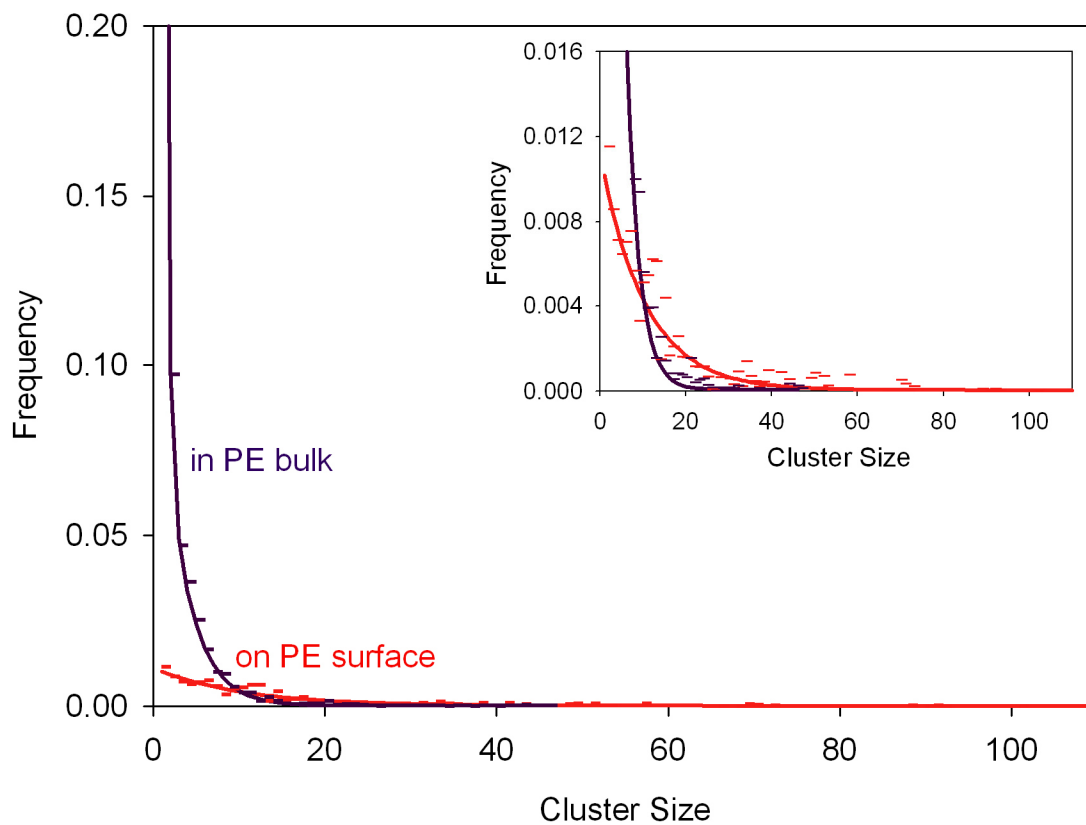


Figure 3.37. Cluster size distribution of the clusters on the PE surface and in bulk of the polymer.

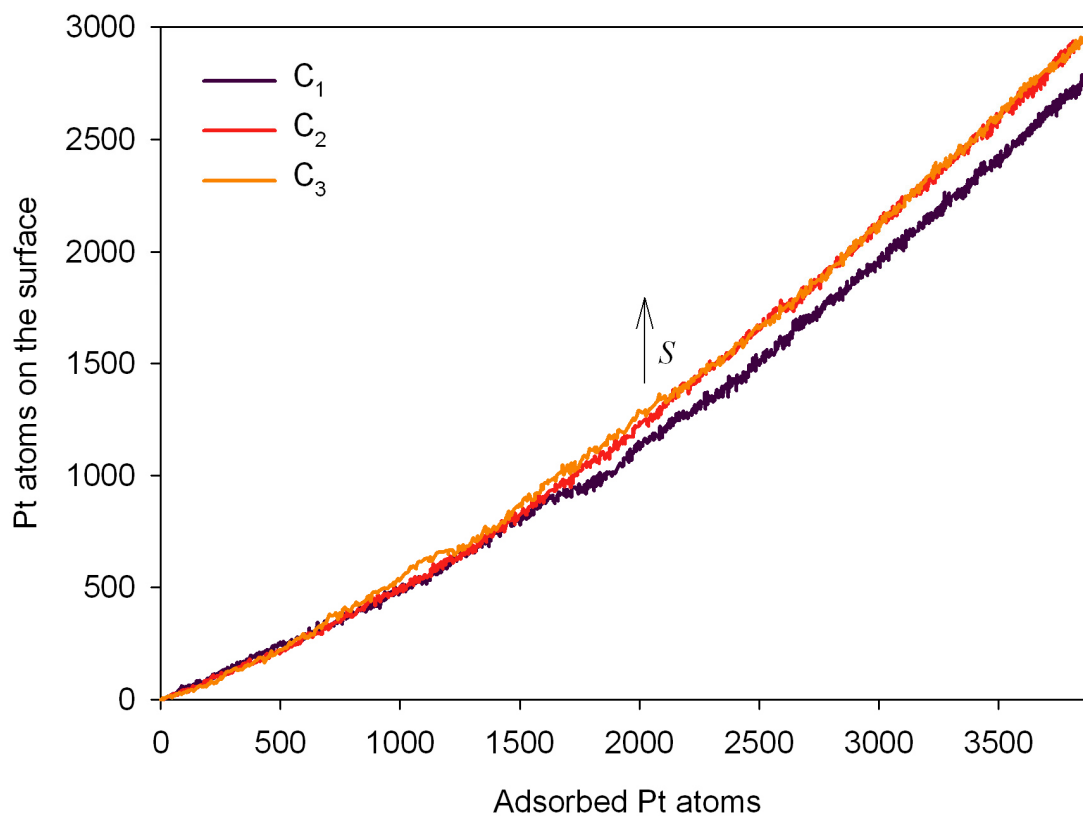


Figure 3.38. Number of Pt atoms on the surface versus the number of Pt atoms in polymer for the simulations  $C_1$  to  $C_3$ .

At higher saturations, simulations C<sub>2</sub> and C<sub>3</sub>, larger clusters are mainly formed in vapor before they condense on the surface. Many clusters have been reached stable sizes higher than the critical size which can diffuse into the polymer. At lower smaller atoms condense on atoms on the surface or diffuse into the polymer.

The limiting behavior of the content of Pt atoms in bulk observed at high saturations can be also explained by this argument. The maximal amount of atoms inside the polymer is mainly determined by the size distribution of the clusters which condense on the surface. In relation to this observation, the previous thermal treatment of the polymer substrate should have an important effect on the embedding of metal clusters since it determines the free volume in the polymer and consequently the critical size of the clusters which can diffuse into the polymer bulk.



# Chapter 4

## Summary and Outlook

The simulation results of condensation of vapors on polymer substrates show that the growth mechanism mainly depends on the relative strength of the interactions between the constituent atoms of the condensing phase and between them and the constituent groups of the polymer. The similarity between both interactions in the case of the system PE-Ar favours a sequentially formation of layers on the surface. Two dimensional islands growth, coalesce in a single cluster and finally form a layer. The condensation of vapors of Pt show a different behavior, clusters of Pt formed in the vapor phase condenses on the PE surface as three dimensional islands due to the strong cohesive forces between the metal atoms. Depending on their size the clusters are able to diffuse into the polymer film even below the glass transition temperature of the polymer.

The initial saturation of the vapor governs the dynamics of the nucleation and also affects the type of growth on the surface. It determines the nucleation rate, the evolution of temperature of the vapor and consequently the size distribution of the clusters which condense on the surface. The extent of the metallization process in the bulk of polymer is indirectly affected by the saturation of the vapor phase. The maximum size of the cluster which can embed into the polymer bulk depends on the accessible free volume of the polymer. Therefore, the higher content of metal atoms inside the polymer observed in simulations at lower vapor saturations is explained by a reduction of the mean size of the clusters deposited on the PE surface.

On the other hand, the growth mode observed in the simulations of Ar on PE changes from a layer-on-layer mechanism to a islands-on-layers one upon increasing the initial vapor saturation along a isotherm. This behavior can be interpreted in the frame of the classical nucleation theory as a crossover in the dimensions of growth at high saturation. The two and three dimensional growth modes are well differentiated at low saturation. The condensation of undersaturated vapors can only be explained by the two dimensional heterogeneous model (HEN 2D). At high saturation the two dimensional and three dimensional for low contact angle growth models converge.

The force field used to represent the interactions between the constituent groups of the polymer show to be suitable for large scale simulations. For the available computation resources<sup>†</sup> simulations in the time scale of 10 ns of a polyethylene sample of about  $10^3 \text{ nm}^3$  can be attained without code parallelization in about a month. A higher level of detail is possible by using full atomistic models. However, the relevant aspects of the behavior of polymer such as the change in their properties near the glass transition, the conformational changes in their constituent segments as the temperature increases and the modifications in their morphology during the embedding of nanoparticles can be described by the UAM models here used.

The use of a non-isothermal ensemble unveils temperature gradients in the system which would be expected in an experiment. First, a temperature gradient is developed in the vapor because of the heat transfer between the vapor and the surface at lower temperature. Second, formation of a film on the polymer substrate is accompanied by heat exchange between the vapor phase and the substrate. Both processes lead to an evolution of the temperature of the vapor, the substrate bulk and the surface, which have to be accounted for in the analysis of the simulation data, for example by classical nucleation theory. A comparison of the simulation results with classical nucleation theory shows that the heterogeneous nucleation rates can be modeled well by classical nucleation theory using the macroscopic properties of the same model fluid as used in the non-equilibrium simulations.

The simulation results here presented open a window for future investigations, e.g., the effect of the polymer substrate, the condensation of metal clusters on copolymer templates, the aging processes of polymer-metal composites over the glass temperature and the changes of the local structures in metal nanoparticles as they condense and diffuse into a polymer.

---

<sup>†</sup> Clio computing cluster provided by the RRZK Computing Center of the University of Cologne. Webpage: <http://www.uni-koeln.de/rrzk/>.

# Appendix

## A.1 Neighbor Lists

The calculation of non-bonded forces is the most time consuming step of a molecular dynamics simulation. The amount of pair interactions to be calculated scales as  $N(N-1)$  and can be reduced to the half  $N(N-1)/2$  when the third Newton law is implemented in to the code, but their computation still scales with power two. The truncation of the potential is a common practice in molecular simulations which notably reduces the computation requirements; only forces between neighbors separated by distances minor to the cut-off radius are calculated.

In each integration step the distances between all pairs must be calculated to determine if they are smaller than the cut-off radius. Verlet<sup>74-78</sup> developed a book-keeping technique; a list of neighbors separated by distances smaller than  $r_1$  is constructed, where  $r_1 > r_c$ . Only distances between Verlet neighbors is calculated at each simulation step and the interaction is calculated only when the distance is smaller than the cut-off radius.

The Verlet list is updated if the maximum displacement of the particles could modify the neighborhood of interacting pairs,  $r_{ij} < r_c$ . For the computation of particle displacements their positions are stored in a vector  $\mathbf{r}_0$  whenever the list is updated.

The actualization criterion is based on the particle displacements in each integration step. In a system of equal-sized particles, where only 1 particle  $i$  moves, the list must be updated if its displacement is higher or equal to the difference  $r_1 - r_c$ , because the particle  $i$  can approximate to another  $j$  which was at the boundary  $r_1^+$  of the Verlet sphere of  $i$  at the last update of the list. When all particles move, the list must be actualized when the maximum displacement  $\max\{\delta r_i\}$  among all the particles of the system is equal or higher than  $(r_1 - r_c)/2$ . In the critical case two particles separated by  $r_1^+$

at the last update of the list, which move one directed to the other, can simultaneously displace a distance  $\max\{\delta r_i\}$ . Additionally, the integration step is a small but finite interval of time, then one integration step before the update of the list this pair is distanced by  $(r_1 - r_c)/2 - \delta_1$  and one step later distanced by  $(r_1 - r_c)/2 + \delta_2$ , where  $\delta = \delta_1 + \delta_2 \leq 2v_{\max}\delta t$ . According to this observation the maximum displacement of the particles is limited  $(r_1 - r_c)/2 + 2v_{\max}\delta t$ . For usual integration steps and normal temperatures the update criterion  $\max\{\delta r_i\} > (r_1 - r_c)/2$  is sufficient, since  $\delta < r_1 - r_c$ .

The simulation of mixtures constitutes a more general situation where the cut-off and Verlet radii of the involved species can be different. For the calculation of interaction between particles of the same type the update criterion;  $\max\{\delta r_i\} > (r_1 - r_c)/2$ , holds for all pairs  $ii$  in mixture. The following criterion is used for the update of the Verlet list of cross interactions  $\max(\max\{\delta r_i\}, \max\{\delta r_j\}) > 0.5 \min(r_{1,i} - r_{c,i}, r_{1,j} - r_{c,j})$

In general, the update interval for the atoms of the same type,  $ii$  pairs, differs from the update interval for pairs of different type,  $ij$  pairs, then one vector  $\mathbf{r}_0$  is required to store the last positions of the particles  $i$  when the Verlet list of  $ii$  interactions is updated, and another is required to store the last positions of  $i$  when the Verlet list of  $ij$  interactions is updated. An alternative, here used, is to update the list of the  $ij$  cross interactions whenever the list of the  $ii$  interactions or the list of  $jj$  interactions is updated. Next the subroutines for the construction of Verlet lists and calculation of the forces using them are presented.

```

subroutine verlet
k=0; r12=r1*r1          ! r1: Verlet radius.
do i=1,N-1
k=k+1
nl(k)=i                ! Particle i is annexed to the list.
* do j=i+1,N           ! Search of Verlet neighbors of i, j>i.
  rxij=rx(i)-rx(j)     ! Calculation of the distance between i and j.
  ryij=ry(i)-ry(j)
  rzij=rz(i)-rz(j)
  rxij=rxij-lx*anint(rxij/lx) ! Distances are calculated within
  ryij=ryij-ly*anint(ryij/ly) ! the Minimum Image Convention.
  rzij=rzij-lz*anint(rzij/lz)
  ri2=rxij*rxij+ryij*ryij+rzij*rzij
*** if (ri2.le.r12) then
  k=k+1                ! If the distance between i and j is
  nl(k)=j              ! smaller than the Verlet radius j is
  ** end if            ! indexed to the list as neighbor of i.
end do
end do
k=k+1
nl(k)=-N               ! N is the last particle indexed to the list.
do i=1,N               ! Actual positions of particles are stored
  rx0(i)=rx(i)         ! in the vector r0 for the later calculation
  ry0(i)=ry(i)         ! of displacements.
  rz0(i)=rz(i)
end do

```



A slight modification of the routine verlet can be introduced in large systems to save computations in the search of neighbors. Two particles are potential neighbors if they are separated by a distance higher than the Verlet radius in one direction ( $x$ ,  $y$  or  $z$ ). If the distance between them, for example in the direction  $z$ , is higher than  $r_1$  they are not neighbors and there is no need to calculate the distances in the remaining directions  $x$  and  $y$  and also not the norm distance vector. The lines \* to \*\* in the subroutine verlet are replaced by

```

do j=i+1,N
  rzij=rz(i)-rz(j)
  rzij=rzij-lz*anint(rzij/lz)
  if (abs(rzij)<rl) then
    ryij=ry(i)-ry(j)
    ryij=ryij-ly*anint(ryij/ly)
    if (abs(ryij)<rl) then
      rxij=rx(i)-rx(j)
      rxij=rxij-lx*anint(rxij/lx)
      if (abs(rxij)<rl) then
        ri2=rxij*rxij+ryij*ryij+rzij*rzij
        if (ri2.le.rl2) then
          k=k+1
          nl(k)=j
        end if
      end if
    end if
  end if
end do

```

Note that the distance is first calculated in the direction  $z$  because in the simulations here performed the box length  $z$  is larger than the length in  $x$  and  $y$ .

In polymer systems the non-bonded interactions between groups in the same chain separated by less than 3 bonds are omitted. An additional condition must be included; line \*\*\* of the subroutine code for the construction of the Verlet list

```

***   if ((ch(i).ne.ch(j)).or.(abs(i-j)>3)) then

```

Where the pointer  $ch(i)$  it indicates the chain to which the group  $i$  belongs.

A particle  $i$  and its neighbors  $j$  are respectively stored in the list as the negative index of the particle  $i$  followed by the indexes of the neighboring particles. The calculation of forces proceed in three steps a) the search of neighbors starts from a negative index  $-i$  in the list b) the distance between the particle  $i$  and its neighbors  $j$  is calculated c) if the distance is lower than the cut-off radius the pair interaction  $i-j$  is calculated, the third Newton's law is applied to calculate the  $j-i$  interaction. d) the interaction between  $i$  and all its neighbors is ends when another negative index in the list is found, the steps a) to d) are repeated.

```

subroutine forces
Initialization of the forces F=0.
rc2=rc*rc           ! rc: cut-off radius
s=1
j=nl(s)
10  i=j              ! i=particle where the total force is calculated
    if (i.eq.n) goto 30 ! calculated.
    if i=N          ! no more interacting pairs are found.
20  s=s+1          ! in other case the neighbors of i are read from the
    j=nl(s)        ! list.
    if (j.lt.0) goto 10 ! if j<0 then i has no neighbors, another particle i
    rxij=rx(i)-rx(j) ! is examined.
    ryij=ry(i)-ry(j) ! else j is a neighbor of i and the distance between ij
    rzij=rz(i)-rz(j) ! is calculated using the Minimum Image Convention
    rxij=rxij-lx*anint(rxij/lx)
    ryij=ryij-ly*anint(ryij/ly)
    rzij=rzij-lz*anint(rzij/lz)
    r2=rxij*rxij+ryij*ryij+rzij*rzij
    if (r2<rc2) then
        fij=F/r      ! if the neighbor j is inside the cut-off sphere of i
                    ! the magnitude of the force F is computed
                    ! and the force that j applies on i is calculated
        fx(i)=fx(i)+fij*rxij
        fy(i)=fy(i)+fij*ryij
        fz(i)=fz(i)+fij*rzij
        fx(j)=fx(j)-fij*rxij
        fy(j)=fy(j)-fij*ryij
        fz(j)=fz(j)-fij*rzij
    end if
    goto 20
30  return
end subroutine

```

! The third Newton's law is applied to compute the  
! force that i apply on j.

## A.2 Expressions for the Calculation of the Forces

### A.2.1 Useful Formulas

Some useful formulas frequently used in the deduction of the force expressions from potential functions are presented here. The gradient of a scalar with respect to a position vector  $\mathbf{r}_u$  is given by

$$\frac{\partial A}{\partial \mathbf{r}_u} = \frac{\partial (\mathbf{A} \cdot \mathbf{A})^{1/2}}{\partial \mathbf{r}_u} = \frac{\mathbf{A}}{A} \cdot \frac{\partial \mathbf{A}}{\partial \mathbf{r}_u}. \quad (\text{A.1})$$

This formula is used, for example, to differentiate the distance between two points with respect to the position vector of one of them.

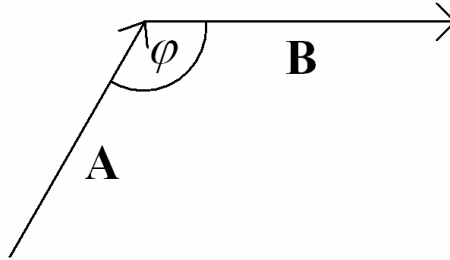


Figure A.1. Schematic representation of the angle formed between two vectors.

The cosine of the angle  $\varphi$  formed between the vectors  $-\mathbf{A}$  and  $\mathbf{B}$  is equal to minus the projection of  $\mathbf{A}$  on  $\mathbf{B}$

$$\cos \varphi = -\frac{\mathbf{A} \cdot \mathbf{B}}{AB}. \quad (\text{A.2})$$

Then, the gradient of the cosine of this angle with respect to a point is given by

$$\frac{\partial \cos \varphi}{\partial \mathbf{r}_u} = -(AB)^{-2} \left[ AB \frac{\partial (\mathbf{A} \cdot \mathbf{B})}{\partial \mathbf{r}_u} - \mathbf{A} \cdot \mathbf{B} \frac{\partial (AB)}{\partial \mathbf{r}_u} \right] = -(AB)^{-1} \left[ \frac{\partial (\mathbf{A} \cdot \mathbf{B})}{\partial \mathbf{r}_u} + \cos \varphi \frac{\partial (AB)}{\partial \mathbf{r}_u} \right] \quad (\text{A.3})$$

Using the chain rule of for the differentiation of a product

$$\frac{\partial (\mathbf{A} \cdot \mathbf{B})}{\partial \mathbf{r}_u} = \mathbf{A} \cdot \frac{\partial \mathbf{B}}{\partial \mathbf{r}_u} + \mathbf{B} \cdot \frac{\partial \mathbf{A}}{\partial \mathbf{r}_u} \quad (\text{A.4})$$

$$\frac{\partial(\mathbf{A} \cdot \mathbf{B})}{\partial \mathbf{r}_u} = \mathbf{A} \cdot \frac{\partial \mathbf{B}}{\partial \mathbf{r}_u} + \mathbf{B} \cdot \frac{\partial \mathbf{A}}{\partial \mathbf{r}_u}. \quad (\text{A.5})$$

A simplified form of (A.3) is obtained

$$\frac{\partial \cos \varphi}{\partial \mathbf{r}_u} = -(AB)^{-1} \left[ \mathbf{A} \cdot \frac{\partial \mathbf{B}}{\partial \mathbf{r}_u} + \mathbf{B} \cdot \frac{\partial \mathbf{A}}{\partial \mathbf{r}_u} \right] - \cos \varphi \left[ \frac{1}{B^2} \mathbf{B} \cdot \frac{\partial \mathbf{B}}{\partial \mathbf{r}_u} + \frac{1}{A^2} \mathbf{A} \cdot \frac{\partial \mathbf{A}}{\partial \mathbf{r}_u} \right]. \quad (\text{A.6})$$

## A.2.2 Valence terms

Intramolecular forces, interactions between neighbor atoms/groups that belong to a same molecule, are developed here.

### A.2.2.1 Valence Bond

A harmonic oscillator term describes the binding energy between two units in a molecule. It is given by a quadratic function of the difference between the distance between these units and the equilibrium distance  $r_0$

$$U_{ij}^b = \frac{1}{2} k_{ij}^b (r_{ij} - r_0)^2. \quad (\text{A.7})$$

Here  $r_{ij} = |\mathbf{r}_{ij}|$ , the distance between two units, is a scalar magnitude and is defined here as the minimal distance through the periodic boundaries of the system, in other words, calculated according to the Minimum Image Convention.

The force on a particle  $u$  is defined as the negative gradient of the potential function with respect to the position vector of  $u$ . Applying the chain rule of the derivative

$$\mathbf{F}_u^b = -\frac{\partial U_{ij}^b}{\partial \mathbf{r}_u} = -\frac{\partial U_{ij}^b}{\partial r_{ij}} \frac{\partial r_{ij}}{\partial \mathbf{r}_u}. \quad (\text{A.8})$$

The first derivative represents the magnitude of the force is given by

$$\frac{\partial U_{ij}^b}{\partial r_{ij}} = k_{ij}^b (r_{ij} - r_0). \quad (\text{A.9})$$

The derivative of the distance between the two units is obtained from the expression (A.1)

$$\frac{\partial r_{ij}}{\partial \mathbf{r}_u} = \frac{\mathbf{r}_{ij}}{r_{ij}} \cdot \frac{\partial \mathbf{r}_{ij}}{\partial \mathbf{r}_u} = \frac{\mathbf{r}_{ij}}{r_{ij}} (\delta_{iu} - \delta_{ju}). \quad (\text{A.10})$$

This derivative is equal to the unit vector oriented in the direction of maximum increase of the potential energy surface. Here  $\delta_{\mu\nu}$  is the Kronecker's delta operator defined as

$$\delta_{\mu\nu} = \begin{cases} 1, & \text{if } \mu = \nu \\ 0, & \text{if } \mu \neq \nu \end{cases}. \quad (\text{A.11})$$

The resulting expression for the force on  $u = i$  of the quadratic valence term is

$$\mathbf{F}_i^b = -\frac{k_{ij}^b}{r_{ij}} (r_{ij} - r_0) \mathbf{r}_{ij}. \quad (\text{A.12})$$

Inserting  $u = j$  in the equation (A.8) shows that these forces satisfies the third Newton's law

$$\mathbf{F}_i^b + \mathbf{F}_j^b = 0. \quad (\text{A.13})$$

For the Morse potential, the deduction proceeds in the same way as (A.8).

$$U_{ij}^b = D \left[ 1 - e^{-\zeta(r_{ij} - r_0)} \right]^2. \quad (\text{A.14})$$

The magnitude of the force is

$$\frac{\partial U_{ij}^b}{\partial r_{ij}} = 2D\zeta e^{-\zeta(r_{ij} - r_0)} \left[ 1 - e^{-\zeta(r_{ij} - r_0)} \right]. \quad (\text{A.15})$$

Then, the resulting expression for the vector forces of the Morse potential is

$$\mathbf{F}_i^b = -\frac{2D\zeta}{r_{ij}} e^{-\zeta(r_{ij} - r_0)} \left[ 1 - e^{-\zeta(r_{ij} - r_0)} \right] \mathbf{r}_{ij}. \quad (\text{A.16})$$

The Morse function presents a similar behavior as the quadratic potential for small oscillations with respect to the equilibrium distance. By means of a second order Mac-Laurin expansion of the Morse potential around  $r_0$  is possible to determine the value of the parameter  $k_b$  for this model that better fits the quadratic potential at the minimum energy point

$$U_{ij}^b(r) \approx U_{ij}^b(r_0) + U_{ij}^{b'}(r_0)(r - r_0) + \frac{1}{2}U_{ij}^{b''}(r_0)(r - r_0)^2 = \frac{1}{2}U_{ij}^{b''}(r_0)(r - r_0)^2 \quad (\text{A.17})$$

Comparing the expressions (A.14) and (A.17) yields

$$U_{ij}^{b''}(r_0) \approx k_b. \quad (\text{A.18})$$

Therefore, the relation between the parameters of the Morse potential and the quadratic potential is approximately

$$k_b \approx 2D\zeta^2. \quad (\text{A.19})$$

### A.2.2.2 Bending

The energy between three consecutive units  $ijk$  in a chain is represented as a quadratic function of  $\cos\theta_{ijk}$

$$U_{ijk}^\theta = \frac{1}{2}k_{ijk}^\theta (\cos\theta_{ijk} - \cos\theta_0)^2. \quad (\text{A.20})$$

It denotes the energy of the dihedral angle centered on the particle  $j$ . The force applied on one of the units that conform the angle  $\theta$ ,  $u=\{i, j, k\}$ , is calculated as the gradient of the energy of the set  $ijk$  respect to the position vector of the particle  $i$

$$\mathbf{F}_u^\theta = -\frac{\partial U_{ijk}^\theta}{\partial \mathbf{r}_u} = -\frac{\partial U_{ijk}^\theta}{\partial \cos\theta_{ijk}} \frac{\partial \cos\theta_{ijk}}{\partial \mathbf{r}_u}. \quad (\text{A.21})$$

The first derivative can be directly calculated

$$\frac{\partial U_{ijk}^\theta}{\partial \cos \theta_{ijk}} = k_{ijk}^\theta (\cos \theta_{ijk} - \cos \theta_0). \quad (\text{A.22})$$

The angle between three consecutive units  $ijk$  is defined according to the Equation (A.2) as

$$\cos \theta_{ijk} = -\frac{\mathbf{r}_{ij} \cdot \mathbf{r}_{jk}}{r_{ij} r_{jk}}. \quad (\text{A.23})$$

By comparison with (A.2) we note that  $\mathbf{A}=\mathbf{r}_{ij}$  and  $\mathbf{B}=\mathbf{r}_{jk}$ . Then, the expression (A.6) can be directly applied

$$\frac{\partial \cos \theta_{ijk}}{\partial \mathbf{r}_u} = -(AB)^{-1} \left[ \mathbf{A} \cdot \frac{\partial \mathbf{B}}{\partial \mathbf{r}_u} + \mathbf{B} \cdot \frac{\partial \mathbf{A}}{\partial \mathbf{r}_u} \right] - \cos \theta_{ijk} \left[ \frac{1}{B^2} \mathbf{B} \cdot \frac{\partial \mathbf{B}}{\partial \mathbf{r}_u} + \frac{1}{A^2} \mathbf{A} \cdot \frac{\partial \mathbf{A}}{\partial \mathbf{r}_u} \right]. \quad (\text{A.24})$$

Terms between parentheses in (A.24) are developed

$$\mathbf{A} \cdot \frac{\partial \mathbf{A}}{\partial \mathbf{r}_u} = \mathbf{r}_{ij} \cdot \frac{\partial \mathbf{r}_{ij}}{\partial \mathbf{r}_u} = \mathbf{r}_{ij} (\delta_{iu} - \delta_{ju}) \quad (\text{A.25})$$

$$\mathbf{A} \cdot \frac{\partial \mathbf{B}}{\partial \mathbf{r}_u} = \mathbf{r}_{ij} \cdot \frac{\partial \mathbf{r}_{jk}}{\partial \mathbf{r}_u} = \mathbf{r}_{ij} (\delta_{ju} - \delta_{ku}) \quad (\text{A.26})$$

$$\mathbf{B} \cdot \frac{\partial \mathbf{A}}{\partial \mathbf{r}_u} = \mathbf{r}_{jk} \cdot \frac{\partial \mathbf{r}_{ij}}{\partial \mathbf{r}_u} = \mathbf{r}_{jk} (\delta_{iu} - \delta_{ju}) \quad (\text{A.27})$$

$$\mathbf{B} \cdot \frac{\partial \mathbf{B}}{\partial \mathbf{r}_u} = \mathbf{r}_{jk} \cdot \frac{\partial \mathbf{r}_{jk}}{\partial \mathbf{r}_u} = \mathbf{r}_{jk} (\delta_{ju} - \delta_{ku}). \quad (\text{A.28})$$

The expressions for the gradient of  $\cos \theta_{ijk}$  with respect to the position vector of the points  $i, j$  and  $k$  are obtained by substitution of  $i, j$  or  $k$  respectively on  $u$

$$\frac{\partial \cos \theta_{ijk}}{\partial \mathbf{r}_i} = \frac{-\mathbf{r}_{jk}}{r_{ij} r_{jk}} - \cos \theta_{ijk} \frac{\mathbf{r}_{ij}}{r_{ij}^2} \quad (\text{A.29})$$

$$\frac{\partial \cos \theta_{ijk}}{\partial \mathbf{r}_j} = \frac{-\mathbf{r}_{ij} + \mathbf{r}_{jk}}{r_{ij} r_{jk}} - \cos \theta_{ijk} \left( \frac{-\mathbf{r}_{ij}}{r_{ij}^2} + \frac{\mathbf{r}_{jk}}{r_{jk}^2} \right) \quad (\text{A.30})$$

$$\frac{\partial \cos \theta_{ijk}}{\partial \mathbf{r}_k} = \frac{\mathbf{r}_{ij}}{r_{ij} r_{jk}} - \cos \theta_{ijk} \left( \frac{-\mathbf{r}_{jk}}{r_{jk}^2} \right). \quad (\text{A.31})$$

The sum of the Equations (A.29), (A.30) and (A.31) is zero

$$\sum_{u=\{i,j,k\}} \frac{\partial \cos \theta_{ijk}}{\partial \mathbf{r}_u} = 0. \quad (\text{A.32})$$

Multiplying each term of the sum (A.32) by  $\partial U / \partial \cos \theta$ , can be used to demonstrate that this angular contribution satisfies the third Newton's law. The sum of the angular forces over the particles on the set  $ijk$  that conform the angle  $\theta_j$  vanishes

$$\mathbf{F}_i^\theta + \mathbf{F}_j^\theta + \mathbf{F}_k^\theta = 0. \quad (\text{A.33})$$

This property is implemented in the code. For this three body contribution the force on  $j$  is calculated as the negative sum of the forces on  $i$  and  $k$

$$\mathbf{F}_j^\theta = -\mathbf{F}_i^\theta - \mathbf{F}_k^\theta. \quad (\text{A.34})$$

### A.2.2.3 Torsion

The energy between four consecutive units of a chain is represented like a series of the cosine of the torsion angle

$$U_{ijkl}^\phi = k_{ijkl}^\phi \sum_{n=0}^5 a_n \cos^n \phi_{ijkl}. \quad (\text{A.35})$$

The torsion angle, formed by four consecutive units of a chain, is equal to the angle formed between the directive vectors  $\mathbf{A}$  and  $\mathbf{B}$  of the planes  $ijk$  and  $jkl$

$$\cos \phi_{ijkl} = -\frac{\mathbf{r}_{ij} \times \mathbf{r}_{jk}}{|\mathbf{r}_{ij} \times \mathbf{r}_{jk}|} \cdot \frac{\mathbf{r}_{jk} \times \mathbf{r}_{kl}}{|\mathbf{r}_{jk} \times \mathbf{r}_{kl}|} = -\frac{\mathbf{A} \cdot \mathbf{B}}{AB}. \quad (\text{A.36})$$



By comparison with (A.2) we define  $\mathbf{A}=\mathbf{r}_{ij}\times\mathbf{r}_{jk}$  and  $\mathbf{B}=\mathbf{r}_{jk}\times\mathbf{r}_{kl}$ . The particle set  $ijkl$  exerts a force on  $u$  equal to

$$\mathbf{F}_u^\phi = -\frac{\partial U_{ijkl}^\phi}{\partial \cos \phi_{ijkl}} \frac{\partial \cos \phi_{ijkl}}{\partial \mathbf{r}_u}. \quad (\text{A.37})$$

The derivative of the first factor is directly calculated

$$\frac{\partial U_{ijkl}^\phi}{\partial \cos \phi_{ijkl}} = k_{ijkl}^\phi \sum_{n=1}^5 n a_n \cos^{n-1} \phi_{ijkl}. \quad (\text{A.38})$$

Using the Equation (A.6) the derivative of the cosines of the torsion angle is given by

$$\frac{\partial \cos \phi_{ijkl}}{\partial \mathbf{r}_u} = -(AB)^{-1} \left[ \mathbf{A} \cdot \frac{\partial \mathbf{B}}{\partial \mathbf{r}_u} + \mathbf{B} \cdot \frac{\partial \mathbf{A}}{\partial \mathbf{r}_u} \right] - \cos \phi_{ijkl} \left[ \frac{1}{B^2} \mathbf{B} \cdot \frac{\partial \mathbf{B}}{\partial \mathbf{r}_u} + \frac{1}{A^2} \mathbf{A} \cdot \frac{\partial \mathbf{A}}{\partial \mathbf{r}_u} \right]. \quad (\text{A.39})$$

Terms between parentheses in (A.39) are developed

$$\frac{\partial \mathbf{A}}{\partial \mathbf{r}_u^\alpha} = \frac{\partial (\mathbf{r}_{ij} \times \mathbf{r}_{jk})}{\partial \mathbf{r}_u^\alpha} = \frac{\partial (\varepsilon_{\eta\mu\nu} \mathbf{r}_{ij}^\mu \mathbf{r}_{jk}^\nu)}{\partial \mathbf{r}_u^\alpha} = \varepsilon_{\eta\mu\alpha} \mathbf{r}_{ij}^\mu (\delta_{ju} - \delta_{ku}) + \varepsilon_{\eta\alpha\nu} \mathbf{r}_{jk}^\nu (\delta_{iu} - \delta_{ju}) \quad (\text{A.40})$$

$$\frac{\partial \mathbf{B}}{\partial \mathbf{r}_u^\alpha} = \frac{\partial (\mathbf{r}_{jk} \times \mathbf{r}_{kl})}{\partial \mathbf{r}_u^\alpha} = \frac{\partial (\varepsilon_{\eta\mu\nu} \mathbf{r}_{jk}^\mu \mathbf{r}_{kl}^\nu)}{\partial \mathbf{r}_u^\alpha} = \varepsilon_{\eta\mu\alpha} \mathbf{r}_{jk}^\mu (\delta_{ku} - \delta_{lu}) + \varepsilon_{\eta\alpha\nu} \mathbf{r}_{kl}^\nu (\delta_{ju} - \delta_{ku}) \quad (\text{A.41})$$

$$\mathbf{A} \cdot \frac{\partial \mathbf{A}}{\partial \mathbf{r}_u} = \varepsilon_{\eta\mu\alpha} \mathbf{A}^\eta \mathbf{r}_{ij}^\mu (\delta_{ju} - \delta_{ku}) + \varepsilon_{\eta\alpha\nu} \mathbf{A}^\eta \mathbf{r}_{jk}^\nu (\delta_{iu} - \delta_{ju}) = \mathbf{A} \times \mathbf{r}_{ij} (\delta_{ju} - \delta_{ku}) - \mathbf{A} \times \mathbf{r}_{jk} (\delta_{iu} - \delta_{ju}) \quad (\text{A.42})$$

$$\mathbf{B} \cdot \frac{\partial \mathbf{A}}{\partial \mathbf{r}_u} = \varepsilon_{\eta\mu\alpha} \mathbf{B}^\eta \mathbf{r}_{ij}^\mu (\delta_{ju} - \delta_{ku}) + \varepsilon_{\eta\alpha\nu} \mathbf{B}^\eta \mathbf{r}_{jk}^\nu (\delta_{iu} - \delta_{ju}) = \mathbf{B} \times \mathbf{r}_{ij} (\delta_{ju} - \delta_{ku}) - \mathbf{B} \times \mathbf{r}_{jk} (\delta_{iu} - \delta_{ju}) \quad (\text{A.43})$$

$$\mathbf{A} \cdot \frac{\partial \mathbf{B}}{\partial \mathbf{r}_u} = \varepsilon_{\eta\mu\alpha} \mathbf{A}^\eta \mathbf{r}_{jk}^\mu (\delta_{ku} - \delta_{lu}) + \varepsilon_{\eta\alpha\nu} \mathbf{A}^\eta \mathbf{r}_{kl}^\nu (\delta_{ju} - \delta_{ku}) = \mathbf{A} \times \mathbf{r}_{jk} (\delta_{ku} - \delta_{lu}) - \mathbf{A} \times \mathbf{r}_{kl} (\delta_{ju} - \delta_{ku}) \quad (\text{A.44})$$

$$\mathbf{B} \cdot \frac{\partial \mathbf{B}}{\partial \mathbf{r}_u} = \varepsilon_{\eta\mu\alpha} \mathbf{B}^\eta \mathbf{r}_{jk}^\mu (\delta_{ku} - \delta_{lu}) + \varepsilon_{\eta\alpha\nu} \mathbf{B}^\eta \mathbf{r}_{kl}^\nu (\delta_{ju} - \delta_{ku}) = \mathbf{B} \times \mathbf{r}_{jk} (\delta_{ku} - \delta_{lu}) - \mathbf{B} \times \mathbf{r}_{kl} (\delta_{ju} - \delta_{ku}). \quad (\text{A.45})$$

Using the definition of the Kronecker's delta the expressions for the gradient of in the nodes  $i, j, k$  and  $l$  are deduced.

For  $u = i$

$$\mathbf{A} \cdot \frac{\partial \mathbf{A}}{\partial \mathbf{r}_i} = -\mathbf{A} \times \mathbf{r}_{jk} \quad (\text{A.46})$$

$$\mathbf{B} \cdot \frac{\partial \mathbf{A}}{\partial \mathbf{r}_i} = -\mathbf{B} \times \mathbf{r}_{jk} \quad (\text{A.47})$$

$$\mathbf{A} \cdot \frac{\partial \mathbf{B}}{\partial \mathbf{r}_i} = 0 \quad (\text{A.48})$$

$$\mathbf{B} \cdot \frac{\partial \mathbf{B}}{\partial \mathbf{r}_i} = 0. \quad (\text{A.49})$$

For  $u = j$

$$\mathbf{A} \cdot \frac{\partial \mathbf{A}}{\partial \mathbf{r}_j} = \mathbf{A} \times \mathbf{r}_{ij} + \mathbf{A} \times \mathbf{r}_{jk} \quad (\text{A.50})$$

$$\mathbf{B} \cdot \frac{\partial \mathbf{A}}{\partial \mathbf{r}_j} = \mathbf{B} \times \mathbf{r}_{ij} + \mathbf{B} \times \mathbf{r}_{jk} \quad (\text{A.51})$$

$$\mathbf{A} \cdot \frac{\partial \mathbf{B}}{\partial \mathbf{r}_j} = -\mathbf{A} \times \mathbf{r}_{kl} \quad (\text{A.52})$$

$$\mathbf{B} \cdot \frac{\partial \mathbf{B}}{\partial \mathbf{r}_j} = -\mathbf{B} \times \mathbf{r}_{kl}. \quad (\text{A.53})$$

For  $u = k$

$$\mathbf{A} \cdot \frac{\partial \mathbf{A}}{\partial \mathbf{r}_k} = -\mathbf{A} \times \mathbf{r}_{ij} \quad (\text{A.54})$$

$$\mathbf{B} \cdot \frac{\partial \mathbf{A}}{\partial \mathbf{r}_u} = -\mathbf{B} \times \mathbf{r}_{ij} \quad (\text{A.55})$$

$$\mathbf{A} \cdot \frac{\partial \mathbf{B}}{\partial \mathbf{r}_u} = \mathbf{A} \times \mathbf{r}_{jk} + \mathbf{A} \times \mathbf{r}_{kl} \quad (\text{A.56})$$

$$\mathbf{B} \cdot \frac{\partial \mathbf{B}}{\partial \mathbf{r}_u} = \mathbf{B} \times \mathbf{r}_{jk} + \mathbf{B} \times \mathbf{r}_{kl}. \quad (\text{A.57})$$

For  $u = l$

$$\mathbf{A} \cdot \frac{\partial \mathbf{A}}{\partial \mathbf{r}_u} = 0 \quad (\text{A.58})$$

$$\mathbf{B} \cdot \frac{\partial \mathbf{A}}{\partial \mathbf{r}_u} = 0 \quad (\text{A.59})$$

$$\mathbf{A} \cdot \frac{\partial \mathbf{B}}{\partial \mathbf{r}_u} = -\mathbf{A} \times \mathbf{r}_{jk} \quad (\text{A.60})$$

$$\mathbf{B} \cdot \frac{\partial \mathbf{B}}{\partial \mathbf{r}_u} = -\mathbf{B} \times \mathbf{r}_{jk}. \quad (\text{A.61})$$

Inserting the Equations (A.46) to (A.61) in the expression (A.39)

$$\frac{\partial \cos \phi_{ijkl}}{\partial \mathbf{r}_i} = \frac{\mathbf{B} \times \mathbf{r}_{jk}}{AB} - \cos \phi_{ijkl} \left[ \frac{-\mathbf{A} \times \mathbf{r}_{jk}}{A^2} \right] \quad (\text{A.62})$$

$$\frac{\partial \cos \phi_{ijkl}}{\partial \mathbf{r}_j} = \frac{\mathbf{A} \times \mathbf{r}_{kl} - \mathbf{B} \times \mathbf{r}_{ij} - \mathbf{B} \times \mathbf{r}_{jk}}{AB} - \cos \phi_{ijkl} \left[ \frac{\mathbf{A} \times \mathbf{r}_{ij} + \mathbf{A} \times \mathbf{r}_{jk}}{A^2} + \frac{-\mathbf{B} \times \mathbf{r}_{kl}}{B^2} \right] \quad (\text{A.63})$$

$$\frac{\partial \cos \phi_{ijkl}}{\partial \mathbf{r}_k} = \frac{-\mathbf{A} \times \mathbf{r}_{jk} - \mathbf{A} \times \mathbf{r}_{kl} + \mathbf{B} \times \mathbf{r}_{ij}}{AB} - \cos \phi_{ijkl} \left[ \frac{-\mathbf{A} \times \mathbf{r}_{ij}}{A^2} + \frac{\mathbf{B} \times \mathbf{r}_{jk} + \mathbf{B} \times \mathbf{r}_{kl}}{B^2} \right] \quad (\text{A.64})$$

$$\frac{\partial \cos \phi_{ijkl}}{\partial \mathbf{r}_l} = \frac{\mathbf{A} \times \mathbf{r}_{jk}}{AB} - \cos \phi_{ijkl} \left[ \frac{-\mathbf{B} \times \mathbf{r}_{jk}}{B^2} \right]. \quad (\text{A.65})$$

The sum of the Equations (A.62) to (A.65) is zero:

$$\sum_{u=\{i,j,k,l\}} \frac{\partial \cos \phi_{ijkl}}{\partial \mathbf{r}_u} = 0. \quad (\text{A.66})$$

By multiplying each term of the sum (A.66) by  $\partial U / \partial \cos \phi$  it can be demonstrated that the sum of the torsion forces over the particles  $ijkl$ , which conform the angle  $\phi_{ijkl}$ , vanishes

$$\mathbf{F}_i^\phi + \mathbf{F}_j^\phi + \mathbf{F}_k^\phi + \mathbf{F}_l^\phi = 0. \quad (\text{A.67})$$

Here, the force on each node  $ijkl$  has been developed to verify the consistency with the third Newton's law. In the code implementation this property is used. The forces on  $i, j, l$  are respectively calculated with the expressions (A.62), (A.63) and (A.65), while the force on  $k$  is obtained from (A.67).

## A.2.3 Non-bonded Interactions

### A.2.3.1 Lennard Jones Potential

A truncated 6-12 Lennard Jones potential is used to describe the non-bonded interactions between Ar atoms, between methyl groups in the polyethylene and the crossed interactions Ar-CH<sub>2</sub>, Ar-Pt and CH<sub>2</sub>-Pt:

$$U_{ij}^{\text{nb}} = 4\varepsilon_{ij} \left[ \left( \frac{\sigma_{ij}}{r_{ij}} \right)^{12} - \left( \frac{\sigma_{ij}}{r_{ij}} \right)^6 \right]. \quad (\text{A.68})$$

In the UAM model for polyethylene non-bonded interactions between methyl groups in the same chain separated by distances minor as three valence bonds are omitted.

Applying the differentiation chain rule the force that a particle  $j$  exerts on another  $i$  is

$$\mathbf{F}_i^{\text{nb}} = -\frac{\partial U_{ij}^{\text{nb}}}{\partial \mathbf{r}_i} = -\frac{\partial U_{ij}^{\text{nb}}}{\partial r_{ij}} \frac{\partial r_{ij}}{\partial \mathbf{r}_i}. \quad (\text{A.69})$$

The magnitude of this force is

$$\frac{\partial U_{ij}^{\text{nb}}}{\partial r_{ij}} = -\frac{48\varepsilon_{ij}}{r_{ij}} \left[ \left( \frac{\sigma_{ij}}{r_{ij}} \right)^{12} - \frac{1}{2} \left( \frac{\sigma_{ij}}{r_{ij}} \right)^6 \right]. \quad (\text{A.70})$$

The directive vector of the force is given by the Equation (A.10). Thus, the expression of the force between two units  $i$  and  $j$  is

$$\mathbf{F}_{ij}^{\text{nb}} = \frac{48\varepsilon_{ij}}{r_{ij}^2} \left[ \left( \frac{\sigma_{ij}}{r_{ij}} \right)^{12} - \frac{1}{2} \left( \frac{\sigma_{ij}}{r_{ij}} \right)^6 \right] \mathbf{r}_{ij}. \quad (\text{A.71})$$

Interactions between two different types of particles are calculated with Lorentz-Berthelot combining rules for the cross parameters:

$$\sigma_{ij} = \frac{\sigma_i + \sigma_j}{2} \quad (\text{A.72})$$

$$\varepsilon_{ij} = (\varepsilon_i \varepsilon_j)^{1/2}. \quad (\text{A.73})$$

### A.2.3.2 Embedded Atom Method (EAM)

In the Embedded Atom Method the potential energy of the system is given a sum of an embedding function  $F$  and a Coulomb potential  $\phi$

$$U = \sum_i F_i(\rho_{\text{h},i}) + \frac{1}{2} \sum_i \sum_{j \neq i} \phi_{ij}(r_{ij}) \quad (\text{A.74})$$

$$\rho_{\text{h},i} = \sum_{j \neq i} \rho_{\text{at},j}(r_{ij}). \quad (\text{A.75})$$

In order to facilitate the differentiation of the Expression (A.74) it is expanded as

$$U = \sum_{i \neq k} [F_i(\rho_{\text{h},i})] + F_k(\rho_{\text{h},k}) + \frac{1}{2} \sum_{i \neq k} \sum_{j \neq i,k} \phi_{ij}(r_{ij}) + \frac{1}{2} \sum_{j \neq k} \phi_{kj}(r_{kj}) + \frac{1}{2} \sum_{i \neq k} \phi_{ik}(r_{ik}). \quad (\text{A.76})$$

Since the electrostatic pair potential is symmetric and  $r_{kj} = r_{jk}$  it follows

$$\phi_{kj}(r_{kj}) = \phi_{jk}(r_{jk}). \quad (\text{A.77})$$

The sum is not affected by exchange of indices

$$\sum_{j \neq k} \phi_{jk}(r_{jk}) = \sum_{i \neq k} \phi_{ik}(r_{ik}). \quad (\text{A.78})$$

Inserting the Equation (A.78) in (A.76) an equivalent form of (A.74) is obtained

$$U = \sum_{i \neq k} [F_i(\rho_{h,i})] + F_k(\rho_{h,k}) + \frac{1}{2} \sum_{i \neq k} \sum_{j \neq i,k} \phi_{ij}(r_{ij}) + \sum_{i \neq k} \phi_{ik}(r_{ik}). \quad (\text{A.79})$$

Therefore, the total force on a particle  $k$  of the system is

$$\mathbf{F}_k = -\frac{\partial U}{\partial \mathbf{r}_k} = -\frac{\partial}{\partial \mathbf{r}_k} \left[ \sum_{i \neq k} [F_i(\rho_{h,i})] + F_k(\rho_{h,k}) + \frac{1}{2} \sum_{i \neq k} \sum_{j \neq i,k} \phi_{ij}(r_{ij}) + \sum_{i \neq k} \phi_{ik}(r_{ik}) \right]. \quad (\text{A.80})$$

The following notations are introduced

$$\text{a) } F' = \frac{\partial F}{\partial \rho_h}, \quad \text{b) } \rho^{at} = \frac{\partial \rho^{at}}{\partial \mathbf{r}} \quad \text{and} \quad \text{c) } \phi' = \frac{\partial \phi}{\partial \mathbf{r}}. \quad (\text{A.81})$$

Next, each of the terms in parentheses is derived

$$\frac{\partial}{\partial \mathbf{r}_k} \sum_{i \neq k} F_i(\rho_{h,i}) = \sum_{i \neq k} \frac{\partial F_i}{\partial \rho_{h,i}} \sum_{j \neq i} \frac{\partial \rho_j^{at}}{\partial r_{ij}} \frac{\partial r_{ij}}{\partial \mathbf{r}_k} = \sum_{i \neq k} \frac{\partial F_i}{\partial \rho_{h,i}} \frac{\partial \rho_k^{at}}{\partial r_{ik}} \frac{\partial r_{ik}}{\partial \mathbf{r}_k} = \sum_{i \neq k} F'_i \rho_k^{at} \frac{\mathbf{r}_{ki}}{r_{ki}}. \quad (\text{A.82})$$

The derivative of the second term is given by

$$\frac{\partial F_k(\rho_{h,k})}{\partial \mathbf{r}_k} = \frac{\partial F_k}{\partial \rho_{h,k}} \sum_{j \neq k} \frac{\partial \rho_j^{at}}{\partial r_{kj}} \frac{\partial r_{kj}}{\partial \mathbf{r}_k} = F'_k \sum_{j \neq k} \rho_j^{at} \frac{\mathbf{r}_{kj}}{r_{kj}} = \sum_{i \neq k} F'_k \rho_i^{at} \frac{\mathbf{r}_{ki}}{r_{ki}}. \quad (\text{A.83})$$

The derivative of the third term vanishes since the sum is defined by indices where  $\delta_{ik}$  and  $\delta_{jk}$  are always zero:

$$\frac{\partial}{\partial \mathbf{r}_k} \sum_{i \neq k} \sum_{j \neq i, k} \phi_{ij}(r_{ij}) = \sum_{i \neq k} \sum_{j \neq i, k} \phi'_{ij} \frac{\mathbf{r}_{ij}}{r_{ij}} (\delta_{ik} - \delta_{jk}) = 0. \quad (\text{A.84})$$

The derivative of the last term is given by

$$\frac{\partial}{\partial \mathbf{r}_k} \sum_{i \neq k} \phi_{ik}(r_{ik}) = \sum_{i \neq k} \phi'_{ik} \frac{\mathbf{r}_{ki}}{r_{ki}}. \quad (\text{A.85})$$

Inserting the expressions (A.83) to (A.85) in (A.80) the total force on  $k$  results

$$\mathbf{F}_k = - \sum_{i \neq k} \left( F'_i \rho_k^{\text{at}} + F'_k \rho_i^{\text{at}} + \phi'_{ik} \right) \frac{\mathbf{r}_{ki}}{r_{ki}}. \quad (\text{A.86})$$

Then, the pair force for the EAM potential is

$$\mathbf{F}_{ij} = \left( F'_i \rho_j^{\text{at}} + F'_j \rho_i^{\text{at}} + \phi'_{ij} \right) \frac{\mathbf{r}_{ij}}{r_{ij}}. \quad (\text{A.87})$$

The interaction of a pair depends on the surrounding medium since the derivative of the embedding energy is evaluated at the local host electron density.

The EAM forces are evaluated by interpolation from tabulated values of the functions  $F'$ ,  $\rho^{\text{at}}$ ,  $\phi'$  and their derivatives.

### A.3 Virial Contributions to the Pressure

The pressure can be decomposed in a kinetic and a configurational part. The first part is defined from the momentum of the particles and independent of the interaction model, the second is computed from the virial:

$$P = \frac{1}{dV} \left( \sum_i \frac{\mathbf{p}_i^2}{m_i} + W \right). \quad (\text{A.88})$$

The virial  $W$  is the sum over all particles in the system of the internal product between the position vector and the net applied force on each particle.

The total force on a particle is the sum of all valence terms; bond, harmonic cosine, torsion, etc. and non-bonded terms: Van der Waals interactions, electrostatic interactions, etc.:

$$W = \sum_i \mathbf{r}_i \cdot \mathbf{F}_{i,t}. \quad (\text{A.89})$$

The Expression (A.88) is extended to define the components of the pressure tensor as follows

$$P^{\alpha\beta} = \frac{1}{dV} \left( \sum_i \frac{\mathbf{p}_i^\alpha \cdot \mathbf{p}_i^\beta}{m_i} + W^{\alpha\beta} \right). \quad (\text{A.90})$$

The  $\alpha\beta$  component of the virial term is the sum over all particles of the internal product between the  $\alpha$  component of the position vector of a particle  $i$  and the  $\beta$  component of the total force on  $i$

$$W^{\alpha\beta} = \sum_i \mathbf{r}_i^\alpha \cdot \mathbf{F}_{i,t}^\beta. \quad (\text{A.91})$$

As the interaction energy can be decomposed in the sum of different contributions, also the interaction force and the virial term associated to these contributions can be decomposed. For example, in the UAM model it is



$$W = \sum_{\{\text{confs}\}} W_{ij}^b + W_{ijk}^\theta + W_{ijkl}^\phi + W_{ij}^{nb} . \quad (\text{A.92})$$

The sum (A.92) applies over all the possible set of non-bonded pairs, bonds, dihedral and torsion angles. The components of the virial term are computed in this work to perform simulations of polymer at a given pressure. Next, the expressions of the components of the virial term for each contribution of the UAM models in a linear chain are deduced.

### A.3.1 Valence Contributions

#### A.3.1.1 Valence Bond

The contribution of the valence bond term on the  $\alpha\beta$  component of the virial term is given by

$$W_{\text{chain}}^{\text{b},\alpha\beta} = \sum_{i=1}^m \mathbf{r}_i^\alpha \cdot \mathbf{F}_i^{\text{b},\beta} . \quad (\text{A.93})$$

In a linear chain the total bond valence force on a unit  $i$  is equal to the sum of the forces with his neighbors  $i-1$  and  $i+1$

$$\mathbf{F}_i^{\text{b},\beta} = \mathbf{F}_{i,i-1}^{\text{b},\beta} + \mathbf{F}_{i,i+1}^{\text{b},\beta} . \quad (\text{A.94})$$

Inserting the expressions for the force on each group of a finite chain (A.94) in the expression (A.93)

$$W_{\text{chain}}^{\text{b},\alpha\beta} = \sum_{i=1}^m \mathbf{r}_i^\alpha \cdot \mathbf{F}_{i,i-1}^{\text{b},\beta} + \sum_{i=1}^m \mathbf{r}_i^\alpha \cdot \mathbf{F}_{i,i+1}^{\text{b},\beta} . \quad (\text{A.95})$$

Both terms are grouped in a common sum. The second term of the expression (A.96) can be rewritten by means of an interchange of indices and the third law of Newton is applied

$$\sum_{i=1}^m \mathbf{r}_i^\alpha \cdot \mathbf{F}_{i,i-1}^{\text{b},\beta} = \sum_{i=0}^{m-1} \mathbf{r}_{i+1}^\alpha \cdot \mathbf{F}_{i+1,i}^{\text{b},\beta} = \sum_{i=0}^{m-1} \mathbf{r}_{i+1}^\alpha \cdot (-\mathbf{F}_{i,i+1}^{\text{b},\beta}) . \quad (\text{A.96})$$

An expression for the bond contribution to the virial term in a chain is obtained

$$W_{\text{chain}}^{\text{b},\alpha\beta} = \mathbf{r}_1^\alpha \cdot \mathbf{F}_{0,1}^{\text{b},\beta} + \mathbf{r}_m^\alpha \cdot \mathbf{F}_{m,m+1}^{\text{b},\beta} + \sum_{i=1}^{m-1} \mathbf{r}_{i,i+1}^\alpha \cdot \mathbf{F}_{i,i+1}^{\text{b},\beta} . \quad (\text{A.97})$$

The end groups of a finite linear chain represent an exception, because they have only one neighbor, then

$$\mathbf{F}_{0,1}^{\text{b},\beta} = 0 \text{ and } \mathbf{F}_{m,m+1}^{\text{b},\beta} = 0 . \quad (\text{A.98})$$

In the end groups the virial reduces to

$$W_{\text{chain}}^{\text{b},\alpha\beta} = \sum_{i=1}^{m-1} \mathbf{r}_{i,i+1}^\alpha \cdot \mathbf{F}_{i,i+1}^{\text{b},\beta} \quad (\text{A.99})$$

while in a semi-infinite chains the end groups are connected

$$\mathbf{F}_{0,1}^{\text{b},\beta} = -\mathbf{F}_{m,m+1}^{\text{b},\beta} . \quad (\text{A.100})$$

The virial in a semi-infinite chain results

$$W_{\text{chain}}^{\text{b},\alpha\beta} = \mathbf{r}_{m,1}^\alpha \cdot \mathbf{F}_{m,1}^{\text{b},\beta} + \sum_{i=1}^{m-1} \mathbf{r}_{i,i+}^\alpha \cdot \mathbf{F}_{i,i+}^{\text{b},\beta} = \sum_{i=1}^m \mathbf{r}_{i,i+}^\alpha \cdot \mathbf{F}_{i,i+}^{\text{b},\beta} . \quad (\text{A.101})$$

The notation  $i_+$  is used to denote the first neighbor of  $i$  in the direction of ascending indices in the chain. The total contribution of the valence term is equal to the sum over all the chains of the system

$$W^{\text{b},\alpha\beta} = \sum_{j=1}^{\text{ch}} W_j^{\text{b},\alpha\beta} . \quad (\text{A.102})$$

Distances are calculated according to the Minimum Image Convention (2.27). This criterion must also be used for the calculation of the force, which depends on the relative distance of particles.

### A.3.1.2 Bending

The bending contribution on the  $\alpha\beta$  component of the virial is obtained summing over all the possible angles formed by three consecutive units in the linear chain

$$W_{\text{chain}}^{\theta,\alpha\beta} = \sum_{i=1}^m \left( \mathbf{r}_{i-1}^{\alpha} \cdot \mathbf{F}_{i-1,i}^{\theta,\beta} + \mathbf{r}_i^{\alpha} \cdot \mathbf{F}_{i,i}^{\theta,\beta} + \mathbf{r}_{i+1}^{\alpha} \cdot \mathbf{F}_{i+1,i}^{\theta,\beta} \right). \quad (\text{A.103})$$

Here denotes the force on  $i$  of the angle centered on  $j$ . The virial contribution is written in terms of relative distance vectors applying the third Newton's law:

$$\mathbf{F}_{i-1,i}^{\theta,\beta} + \mathbf{F}_{i,i}^{\theta,\beta} + \mathbf{F}_{i+1,i}^{\theta,\beta} = 0 \quad (\text{A.104})$$

$$\mathbf{F}_{i,i}^{\theta,\beta} = -\mathbf{F}_{i-1,i}^{\theta,\beta} - \mathbf{F}_{i+1,i}^{\theta,\beta} \quad (\text{A.105})$$

$$\mathbf{r}_{i-1}^{\alpha} \cdot \mathbf{F}_{i-1,i}^{\theta,\beta} + \mathbf{r}_i^{\alpha} \cdot \mathbf{F}_{i,i}^{\theta,\beta} + \mathbf{r}_{i+1}^{\alpha} \cdot \mathbf{F}_{i+1,i}^{\theta,\beta} = (\mathbf{r}_{i-1}^{\alpha} - \mathbf{r}_i^{\alpha}) \cdot \mathbf{F}_{i-1,i}^{\theta,\beta} + (\mathbf{r}_{i+1}^{\alpha} - \mathbf{r}_i^{\alpha}) \cdot \mathbf{F}_{i+1,i}^{\theta,\beta} \quad (\text{A.106})$$

$$W_{\text{chain}}^{\theta,\alpha\beta} = \sum_{i=1}^m \left( \mathbf{r}_{i-1}^{\alpha} \cdot \mathbf{F}_{i-1,i}^{\theta,\beta} + \mathbf{r}_{i+1}^{\alpha} \cdot \mathbf{F}_{i+1,i}^{\theta,\beta} \right). \quad (\text{A.107})$$

The angle in a finite chain of  $m$  groups is defined in the range  $[2, m-1]$  then the sum (A.107) reduces for this case to

$$W_{\text{chain}}^{\theta,\alpha\beta} = \sum_{i=2}^{m-1} \left( \mathbf{r}_{i-1}^{\alpha} \cdot \mathbf{F}_{i-1,i}^{\theta,\beta} + \mathbf{r}_{i+1}^{\alpha} \cdot \mathbf{F}_{i+1,i}^{\theta,\beta} \right). \quad (\text{A.108})$$

This relation holds for semi-infinite chains, but the notation introduced in (A.101) requires to use

$$W_{\text{chain}}^{\theta,\alpha\beta} = \sum_{i=1}^m \left( \mathbf{r}_{i-}^{\alpha} \cdot \mathbf{F}_{i-}^{\theta,\beta} + \mathbf{r}_{i+}^{\alpha} \cdot \mathbf{F}_{i+}^{\theta,\beta} \right). \quad (\text{A.109})$$

As in (A.101)  $i_+$  denotes the first neighbor of  $i$  in the chain in the direction of ascending indices, while  $i_-$  denotes the first neighbor of  $i$  in the opposite direction of the chain. The total contribution of the dihedral angle term is equal to the sum over all the chains of the

system. This three-body term does not contribute to the pressure at all since the trace of the corresponding terms in virial tensor is zero.

$$\sum_{\alpha} W_{\text{chain}}^{\theta, \alpha\alpha} = 0. \quad (\text{A.110})$$

### A.3.1.3 Torsion

The torsion contribution on the  $\alpha\beta$  component of the virial is obtained summing over all the possible angles formed by four consecutive units in the linear chain is

$$W_{\text{chain}}^{\phi, \alpha\beta} = \sum_{i=1}^m (\mathbf{r}_{i-1}^{\alpha} \cdot \mathbf{F}_{i-1,i}^{\phi, \beta} + \mathbf{r}_i^{\alpha} \cdot \mathbf{F}_{i,i}^{\phi, \beta} + \mathbf{r}_{i+1}^{\alpha} \cdot \mathbf{F}_{i+1,i}^{\phi, \beta} + \mathbf{r}_{i+2}^{\alpha} \cdot \mathbf{F}_{i+2,i}^{\phi, \beta}). \quad (\text{A.111})$$

Here  $\mathbf{F}_{i,i}^{\phi, \beta}$  denotes the component  $\beta$  of the force on  $i$  of the angle formed by the planes  $i-1, i, i+1$  and  $i, i+1, i+2$ . The virial contribution is written in terms of relative distance vectors applying the third Newton's law

$$\mathbf{F}_{i-1,i}^{\phi, \beta} + \mathbf{F}_{i,i}^{\phi, \beta} + \mathbf{F}_{i+1,i}^{\phi, \beta} + \mathbf{F}_{i+2,i}^{\phi, \beta} = 0 \quad (\text{A.112})$$

$$\mathbf{F}_{i,i}^{\phi, \beta} = -\mathbf{F}_{i-1,i}^{\phi, \beta} - \mathbf{F}_{i+1,i}^{\phi, \beta} - \mathbf{F}_{i+2,i}^{\phi, \beta} \quad (\text{A.113})$$

$$\mathbf{r}_{i-1}^{\alpha} \cdot \mathbf{F}_{i-1,i}^{\phi, \beta} + \mathbf{r}_i^{\alpha} \cdot \mathbf{F}_{i,i}^{\phi, \beta} + \mathbf{r}_{i+1}^{\alpha} \cdot \mathbf{F}_{i+1,i}^{\phi, \beta} + \mathbf{r}_{i+2}^{\alpha} \cdot \mathbf{F}_{i+2,i}^{\phi, \beta} = \mathbf{r}_{i-1,i}^{\alpha} \cdot \mathbf{F}_{i-1,i}^{\phi, \beta} + \mathbf{r}_{i+1,i}^{\alpha} \cdot \mathbf{F}_{i+1,i}^{\phi, \beta} + (\mathbf{r}_{i+2}^{\alpha} - \mathbf{r}_i^{\alpha}) \cdot \mathbf{F}_{i+2,i}^{\phi, \beta} \quad (\text{A.114})$$

In the code implementation all the valence forces are written in terms of distances between bonded groups, to avoid new calculations in the implementation the distance between  $i$  and his second neighbor is written in terms of first neighbor distances as follows

$$\mathbf{r}_{i+2}^{\alpha} - \mathbf{r}_i^{\alpha} = \mathbf{r}_{i+2}^{\alpha} - \mathbf{r}_{i+1}^{\alpha} + \mathbf{r}_{i+1}^{\alpha} - \mathbf{r}_i^{\alpha} = \mathbf{r}_{i+2,i+1}^{\alpha} + \mathbf{r}_{i+1,i}^{\alpha}. \quad (\text{A.115})$$

The angle in a finite chain is defined for the indices  $[2, m-2]$ , then the torsion contribution to the virial is given by

$$W_{\text{chain}}^{\phi,\alpha\beta} = \sum_{i=2}^{m-2} \left( \mathbf{r}_{i-1,i}^{\alpha} \cdot \mathbf{F}_{i-1,i}^{\phi,\beta} + \mathbf{r}_{i+1,i}^{\alpha} \cdot \mathbf{F}_{i+1,i}^{\phi,\beta} + \left( \mathbf{r}_{i+2,i+1}^{\alpha} + \mathbf{r}_{i+1,i}^{\alpha} \right) \cdot \mathbf{F}_{i+2,i}^{\phi,\beta} \right) \quad (\text{A.116})$$

while in a semi-infinite chain it is

$$W_{\text{chain}}^{\phi,\alpha\beta} = \sum_{i=1}^m \left( \mathbf{r}_{i-,i}^{\alpha} \cdot \mathbf{F}_{i-,i}^{\phi,\beta} + \mathbf{r}_{i+,i}^{\alpha} \cdot \mathbf{F}_{i+,i}^{\phi,\beta} + \left( \mathbf{r}_{i++,i+}^{\alpha} + \mathbf{r}_{i+,i}^{\alpha} \right) \cdot \mathbf{F}_{i++,i}^{\phi,\beta} \right). \quad (\text{A.117})$$

As in the case of bending the torsion term does not contribute to the pressure.

### A.3.2 Non-bonded Interactions

The contribution of non-bonded terms to the  $\alpha\beta$  component of the virial term is

$$W^{\text{nb},\alpha\beta} = \sum_{i=1}^N \mathbf{r}_i^{\alpha} \cdot \mathbf{F}_i^{\text{nb},\beta}. \quad (\text{A.118})$$

The total force on a particle  $i$  due to the non-bonded forces is the sum over all the possible pairs in the system. 1-2 and 1-3 interactions as pairs separated by a distance larger than the cut-off radius are excluded in the sum

$$\sum_{i=1}^N \mathbf{r}_i^{\alpha} \cdot \mathbf{F}_i^{\text{nb},\beta} = \sum_{i=1}^N \sum_{j=1, j \neq i}^N \mathbf{r}_i^{\alpha} \cdot \mathbf{F}_{ij}^{\text{nb},\beta} = \frac{1}{2} \left( \sum_{i=1}^N \sum_{j=1, j \neq i}^N \mathbf{r}_i^{\alpha} \cdot \mathbf{F}_{ij}^{\text{nb},\beta} + \sum_{i=1}^N \sum_{j=1, j \neq i}^N \mathbf{r}_j^{\alpha} \cdot \mathbf{F}_{ji}^{\text{nb},\beta} \right). \quad (\text{A.119})$$

Applying the third Newton's law on the right expression of (A.119) and considering that the sum over all pairs is twice the sum over non-repeating pairs leads to

$$\sum_{i=1}^N \sum_{j=1}^N \mathbf{r}_i^{\alpha} \cdot \mathbf{F}_{ij}^{\text{nb},\beta} + \sum_{i=1}^N \sum_{j=1}^N \mathbf{r}_j^{\alpha} \cdot \mathbf{F}_{ji}^{\text{nb},\beta} = \sum_{i=1}^N \sum_{j=1}^N \mathbf{r}_{ij}^{\alpha} \cdot \mathbf{F}_{ij}^{\text{nb},\beta} = 2 \sum_{i=1}^N \sum_{j>i}^N \mathbf{r}_{ij}^{\alpha} \cdot \mathbf{F}_{ij}^{\text{nb},\beta}. \quad (\text{A.120})$$

The total contribution of non-bonded forces on the virial component is

$$W^{\text{nb},\alpha\beta} = \sum_{i=1}^N \sum_{j>i}^N \mathbf{r}_{ij}^{\alpha} \cdot \mathbf{F}_{ij}^{\text{nb},\beta}. \quad (\text{A.121})$$

## A.4 Cluster Recognition Algorithm

A modification of the Stoddard algorithm<sup>143</sup> is developed to perform the recognition of clusters in a subset of particles. In the method, identical labels are assigned to the particles which belong to the same cluster. The following definition of cluster is adopted; two particles are direct neighbors if they are separated by a distance lower than a given radius  $r_{cl}$ , two particles belongs to a same cluster if they are directly connected or through a chain of direct neighbors. The implemented algorithm is based on the ramified search of neighbors starting from a randomly selected particle.

The inputs of the algorithm are; the labels of the particles where the search is made, the positions of these particles at a given time  $t$  and the box lengths  $L_x$ ,  $L_y$  and  $L_z$ , the last two inputs are necessary to the calculation of the pair distances using the Minimum Image Convention. The search can be made on the whole system or in a part of it, for example, for the recognition of the clusters of atoms of the same type on a surface or to find clusters in vapor phase.

The output of the algorithm are; a vector which contains the labels of each particle  $i$  of the subsystem where the search was made  $et(i)$ , where the element  $i$  of  $et$  indicates the cluster to which  $i$  belongs, and a vector  $num$  where the population of each cluster (the cluster size) is stored. The maximum number of possible clusters in a subsystem of  $N$  particles is  $N$  and corresponds to the case where no neighbors are present.

### Description of the variables

$et$ : vector of particle labels

$lst$ : vector to store the index of labelled particles

$num$ : vector which contains the population (number of atoms/molecules) of each cluster

$ti$ : pointer of the position in the list  $lst$  of the first particle where neighbors are searched in a cycle of the algorithm

$tf$ : pointer of the position in the list  $lst$  of the last particle where neighbors are searched in a cycle of the algorithm.

$e$ : actual label, it starts from 1 and increases by 1 when the search in a cluster is exhausted

```

subroutine clusters
Initialization ** rcl2=rcl*rcl
do while(ti.le.n) ! Cluster are searched until all particles are indexed in lst
u=u+1 ! the next candidate u to begin the search is defined
if (et(u).eq.0) then ! if the particle u is not labeled
ac=tf
ti=tf+1
tf=ti
lst(ti)=u ! then is indexed to the list lst
e=e+1 ! the label e is actualized
et(u)=e ! and the particle u is labelled as e
num(e)=1 ! the population of the cluster e is initialized as 1
do while (tf.ge.ti) ! neighbors of elements in lst between ti and tf are searched
do i=ti,tf
s=lst(i)
do j=1,n
if (et(j).eq.0) then
drz=rz(s)-rz(j)
drz=drz-lz*anint(drz/lz)
if (abs(drz).le.rcl) then
drx=rx(s)-rx(j)
drx=drx-lx*anint(drx/lx)
if (abs(drx).le.rcl) then
dry=ry(s)-ry(j)
dry=dry-ly*anint(dry/ly)
if (abs(dry).le.rcl) then
dr2=drx*drx+dry*dry+drz*drz
if (dr2.le.rcl2) then ! when a neighbor j of u is found
lst(num(e)+ac)=j ! it is added to the list lst
et(j)=e ! and it is labelled as e
num(e)=num(e)+1 ! the population of the cluster e increases
end if
end if
end if
end if
end do
end do
ti=tf+1 ! ti and tf are pointed to the first and last element added to the
tf=num(e)+ac ! list lst in the last search
end do
end if
end do ! and the process is repeated until the search is exhausted
end subroutine

```

At the beginning of the algorithm all labels are defined as 0. The search starts from any particle of the system, for example on the particle  $u = 1$ , the index of this particle is annexed to the list `lst` and adopts the first label different as 0,  $et(1)=e=1$ . Then, all the neighbors of  $u = 1$  are searched, labelled with the same label and annexed to the list `lst`. In the next cycle the neighbors of the particles indexed on `lst` in the last step are searched and the process is repeated; the new neighbors adopt the actual label and are annexed to the list `lst`. The cycle of search and indexing to `lst` is repeated until no new neighbors are found. At this point the label increase by 1  $e \leftarrow e+1$  and the process starts from a non-labelled particle (a particle labelled as 0  $et(u)=0$ ). The algorithm ends when all particles have been labelled, *i.e.* when the number of elements indexed to `lst` is equal to the number of particles of the subsystem where the search was made.

### Surface atoms recognition

An algorithm to recognize the atoms on the surface of a film is implemented in order to analyze separately the properties of atoms: in vapor phase, condensed on the PE surface and in PE bulk, during the simulation.

The properties of argon in the vapor phase and on the polymer surface are calculated separately. The argon atoms adsorbed on the polyethylene surface are recognized with a three-step algorithm: a) first the CH<sub>2</sub> groups in the film surface are localized, b) the argon atoms in the first adsorbed layer are determined, and c) step b) is repeated until no more adsorbed atoms are found.

The recognition of the atoms on the surface of the film here implemented is based on ideas of the cone algorithm<sup>140</sup>, originally proposed to recognize atoms/molecules in the surface of a cluster. The film surfaces here considered is oriented in the  $z$ -axis, the film is centered on the plane  $z=0$ . The recognition of atoms in the positive surface, oriented to the  $+z$ -axis, is as follows; a cone of angle  $\varphi_c$  and axis parallel to the  $z$ -axis is placed at each CH<sub>2</sub> group, located on the region  $z > 0$ . A CH<sub>2</sub> group belongs to the surface if any other CH<sub>2</sub> group is found in the internal region of the cone. The recognition of CH<sub>2</sub> groups on the surface oriented to the  $-z$ -axis is analogue. The amount of groups found on the surface remain almost constant when for small values of the angle  $\varphi_c$ , here a value of  $22.5^\circ$  is used. This step is illustrated in the Figures A.2a and A.2b.

The first layer of adsorbed argon atoms is recognized by a search of all the atoms separated by a distance smaller than a certain cut-off from each surface CH<sub>2</sub> group, which is the cluster definition by the Stillinger's criterion<sup>136</sup>. A cut-off distance equal to  $1.5\sigma_{ij}$  is used to determine if an atom is in contact with a CH<sub>2</sub> group, where the index  $i$  denotes a CH<sub>2</sub> group and  $j$  a Pt or Ar atom (values of  $\sigma_{ij}$  are reported in the Table 3.7). The search is repeated for the atoms deposited on higher layers. This step is illustrated in the Figures A.2c and A.2d. Finally, in order to recognize the clusters atoms adsorbed on the Stoddard algorithm<sup>143</sup> is applied on the atoms located on the surface.



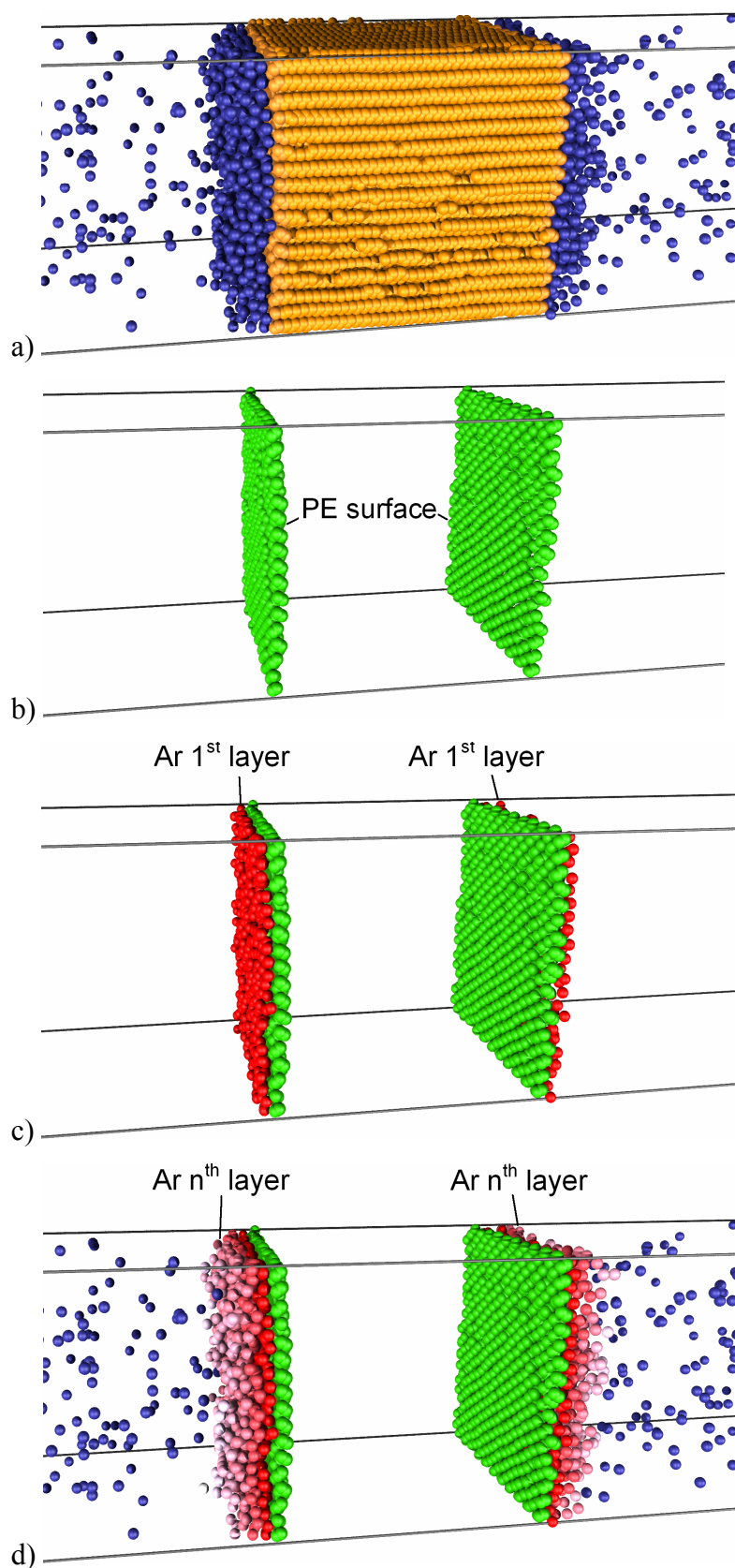


Figure A.2. Snapshots of a condensation simulation at  $T_{PE}=80$  K and  $\rho=50$  g/dm<sup>3</sup> after 5 ns. a) Complete polymer film with condensed argon and a part of the argon vapor phase. b) Surface layers of polyethylene. c) Polyethylene surface layer and first argon layer. d) Polyethylene surface layer with first and all subsequent argon layers. Different layers of ad-atoms are displayed in shades of red.

# References

- [1] Biswas A., Marton Z., Kanzow J., Kruse J., Zaporojtchenko V. and Faupel F., *Nano Lett.* **3**(1), 69 (2003).
- [2] Thran A., Kiene M., Zaporojtchenko V. and Faupel F., *Phys. Rev. Lett.* **82**(9), 1903 (1999).
- [3] Zaporojtchenko V., Behnke K., Thran A., Strunskus T. and Faupel F., *Appl. Surf. Sci.* **144**, 355 (1999).
- [4] Zaporojtchenko V., Strunskus T., Behnke K., Bechtolsheim C. v., Thran A. and Faupel F., *Microelectron. Eng.* **50**, 465 (2000).
- [5] Zaporojtchenko V., Behnke K., Strunskus T. and Faupel F., *Surf. Sci.* **454**, 412 (2000).
- [6] Brune H., Röder H., Boragno C. and Kern K., *Phys. Rev. Lett.* **73**(14), 1955 (1994).
- [7] Venables J. A., Spiller G. D. T. and Hanbücken M., *Rep. Prog. Phys.* **47**, 399 (1984).
- [8] Stroschio J. A., Pierce D. T. and Dragoset R. A., *Phys. Rev. Lett.* **70**, 3615 (1993).
- [9] Kashchiev D., Nucleation, Butterworth-Heinemann, Oxford (2000).
- [10] Ratsch C. and Venables J. A., *J. Vac. Sci. Technol. A* **21**(5), 96 (2003).
- [11] Zhang Z. and Lagally M. G., *Science* **276**, 377 (1997).
- [12] Wadley H. N. G., Zhou X., Johnson R. A. and Neurock M., *Prog. Mater. Sci.* **46**, 329 (2001).
- [13] Toxvaerd S., *J. Chem. Phys.* **117**(22), 10303 (2002).
- [14] Toxvaerd S., *Molecular Simulation* **30**(2), 179 (2004).
- [15] Kimura T. and Maruyama S., *Microscale Thermophys. Eng.* **6**(3), 3 (2002).
- [16] Huang Shi-Ping and Balbuena P. B., *Mol. Phys.* **100**, 2165 (2002).
- [17] Toxvaerd S., *Physica A* **314**, 442 (2002).
- [18] Restagno F., Bocquet and Biben T., *Phys. Rev. Lett.* **84**, 2433 (2000).
- [19] Yasuoka K., Gao G. T. and Zeng X. C., *J. Chem. Phys.* **112**(9), 4279 (2000).
- [20] Gopinathan A., *Phys. Rev. E* **71**, 041601 (2005).
- [21] Lopes W. A. and Jaeger H. M., *Nature* **414**, 735 (2001).
- [22] Lopes W. A. *Phys. Rev. E* **65**, 031606 (2002).
- [23] Faupel F., Willecke R. and Thran A., *Mater. Sci. Eng. R* **22**, 1 (1998).

- [24] Bechtolsheim C. V., Zaporojtchenko V. and Faupel F., *Appl. Surf. Sci.* **151**, 119 (1999).
- [25] Teichoeb J. H. and Forrest J. A., *Phys. Rev. Lett.* **91**, 016104 (2003).
- [26] Zaporojtchenko V., Strunskus T., Erichsen J., Faupel F., *Macromolecules* **34**(5), 1125 (2001).
- [27] Ochoa J. D., Binder K., and Paul W., *J. Phys.: Condens. Matter* **18**, 2777 (2006).
- [28] Schmelzer J., Röpke G. and Mahnke R., *Aggregation Phenomena in Complex Systems*, Wiley-VCH Verlag, Weinheim (1999).
- [29] Zettlemoyer A. C., *Nucleation*, Marcel Dekker, New York (1969).
- [30] Kashchiev D. and van Rosmalen G. M., *Cryst. Res. Technol.* **38**(7), 555 (2003).
- [31] Kashchiev D., *J. Chem. Phys.* **76**, 5098 (1982).
- [32] Sperling L., *Introduction to Physical Polymer Science*, John Wiley & Sons, New York (2001).
- [33] Paul W. and Smith G. D., *Rep. Prog. Phys.* **67**, 1117 (2004).
- [34] Milchev A., Paul W. and Binder K., *Macromol. Theory Simul.* **3**, 305 (1994).
- [35] Binder K., Baschnagel J., Bennemann C. and Paul W., *J. Phys.: Condens. Matter* **11**, A47 (1999).
- [36] Baschnagel J., Bennemann C., Paul W. and Binder K., *J. Phys.: Condens. Matter* **12**, 6365 (2000).
- [37] Varnik F., Bachnagel J. and Binder K., *Phys. Rev. E* **65**, 021507 (2002).
- [38] Izumisawa S. and Jhon M.S., *J. Chem. Phys.* **117**(8), 3972 (2002).
- [39] Starr F. W., Schröder T. B. and Glotzer S. C., *Macromolecules* **35**, 4481 (2002).
- [40] Paul W., *Polymer* **45**, 3901 (2004).
- [41] Car R. and Parrinello M., *Phys. Rev. Lett.* **22**, 2471 (1985).
- [42] Glotzer S. C. and Paul W., *Annu. Rev. Mater. Res.* **32**, 401 (2002).
- [43] Hageman J. C. L., de Groot R. A. and Meier R. J., *Comput. Mater. Sci.* **10**, 180 (1998).
- [44] Martoňák R., Paul W. and Binder K., *Phys. Rev. E* **57**(2), 2425 (1998).
- [45] Rapaport D. C., *J. Phys. A: Math. Gen.* **11**(8), 213 (1978).
- [46] Torres J. A., Nealey P. F. and de Pablo J. J., *Phys. Rev. Lett.* **85**(15), 3221 (2000).
- [47] Böhme T. R. and de Pablo J. J., *J. Chem. Phys.* **116**(22), 9939 (2002).
- [48] Doucet J., Denicolo I., Craievich A. and Collet A., *J. Chem. Phys.* **75**, 5125 (1981).
- [49] Denicolo I., Doucet J., and Craievich A. F., *J. Chem. Phys.* **78**, 1465 (1983).
- [50] Taylor M. G., Kelusky E. C. and Smith I. C. P., *J. Chem. Phys.* **78**, 5108 (1983).

- [51] Doucet J. and Dianoux A. J., *J. Chem. Phys.* **81**, 5043 (1984).
- [52] Maroncelli M., Strauss H. L. and Snyder R. G., *J. Chem. Phys.* **82**, 2811 (1985).
- [53] Tadokoro H., *Structure of Crystalline Polymers*, Wiley Interscience, New York (1979).
- [54] Natta G. and Corradini P., *Rubber Chem. Technol.* **33**, 703 (1960).
- [55] Tieke B., *Makromolekulare Chemie: eine Einführung*, VCH, Weinheim (1997).
- [56] Bassett D. C., Block S. and Piermarini G. J., *J. Appl. Phys.* **45**(10), 4146 (1974).
- [57] Mavrantza I. E., Prentzas D., Mavrantzas V. G. and Galiotis C., *J. Chem. Phys.* **115**(8), 3937 (2001).
- [58] Martoňák R., Paul W. and Binder K., *J. Chem. Phys.* **106**(21), 8918 (1997).
- [59] Rutledge G. C., Lacks D. J., Martoňák R. and Binder K., *J. Chem. Phys.* **108**, 10274 (1998).
- [60] Karasawa N., Dasgupta S. and Goddard III W.A., *J. Phys. Chem.* **95**, 2260 (1991).
- [61] Sorensen R. A., Liao W. B., Kesner L. and Boyd R. H., *Macromolecules* **21**, 200 (1988).
- [62] Ryckaert J. P. and Klein M. L., *J. Chem. Phys.* **85**(3), 1613 (1986).
- [63] Ryckaert J. P., McDonald I. R. and Klein M. L., *Mol. Phys.* **67**(5), 957 (1989).
- [64] Ryckaert J. P., Klein M. L. and McDonald I. R., *Phys. Rev. Lett.* **58**, 698 (1987).
- [65] Parrinello M. and Rahman A., *J. Chem. Phys.* **76**, 2662 (1982).
- [66] Strobl G., *Physik kondensierter Materie. Kristallen, Flüssigkristalle und Polymere*. Springer-Verlag, Berlin (2002).
- [67] Boyd R. H., Gee R. H., Han J. and Jin Y., *J. Chem. Phys.* **101**, 788 (1994).
- [68] Buchholz J., Paul W., Varnik F. and Binder K., *J. Chem. Phys.* **117**, 7364 (2002).
- [69] Han H., Gee R. H. and Boyd R. H., *Macromolecules* **27**, 7781 (1994).
- [70] Lyulin A. V., Bavaev N. K. and Michels M. A. J., *Macromolecules* **36**, 8574 (2003).
- [71] Rigby D. and Roe R.-J., *J. Chem. Phys.* **87**, 7285 (1987).
- [72] Varnik F., *Molekulardynamik Simulationen zum Glasübergang in Makromolekularen Filmen*, Ph.D. Thesis, Universität Mainz (2000).
- [73] de Gennes P. G., *Eur. Phys. J. E* **2**, 201 (2000).
- [74] Frenkel D. and Smit B., *Understanding Molecular Simulation*. Acad. Press (1996).
- [75] Allen M. and Tildesley D. J., *Computer Simulation of Liquids*. Oxford University Press (1987).

- [76] Griebel M., Knapek S., Zumbusch G. and Caglar A., Numerische Simulation in der Moleküldynamik. Numerik, Algorithmen, Parallelisierung, Anwendungen. Springer-Verlag, Berlin (2004).
- [77] Hentschke R., Aydt E. M., Fodi B. and Stöckelmann, Molekulares Modellieren mit Kraftfeldern. Einführung in die Theorie und Praxis der Computersimulation molekularer Systeme, Universität Wuppertal (2004).
- [78] Ercolessi F., A Molecular Dynamics Primer. International School for Advanced Studies, Trieste (1997).
- [79] Deuffhard P., Computational Molecular Dynamics: Challenges, Methods, Ideas. Springer-Verlag (1999).
- [80] Heermann D. W., Computer Simulation Methods in Theoretical Physics. Springer-Verlag (1990).
- [81] Hoover W. G., Computational Statistical Mechanics, Elsevier (1991).
- [82] Berendsen H. J. C., Postma J. P. M, van Gunsteren W. F. and DiNola A., *J. Chem. Phys.* **81**, 3684 (1984).
- [83] Nosé S., *Mol. Phys.* **52**, 255 (1984).
- [84] Nosé S., *J. Chem. Phys.* **81**, 511 (1984).
- [85] Hoover W. G., *Phys. Rev. A* **31**, 1695 (1985).
- [86] Andersen H., *J. Chem. Phys.* **72**, 2384 (1980).
- [87] Westergren J., Grönbeck H., Kim S. G., Tománek D., *J. Chem. Phys.* **107**, 3071 (1997).
- [88] Toxvaerd S., *J. Chem. Phys.* **119**(20), 10764 (2003).
- [89] Lümmer N. and Kraska T., *Nanotechnology* **15**, 525 (2004)
- [90] Lümmer N. and Kraska T., *Comput. Mater. Sci.* **35**, 210 (2006).
- [91] Mülders T., Molekular-Dynamik-Simulationen semiflexibler Makromoleküle bei konstanten Druck und konstanter Temperatur. Logos Verlag (2000).
- [92] Melchionna S., Ciccotti G. and Holian B., *Mol. Phys.* **78**, 533 (1993).
- [93] Prausnitz J. M. *et al.*, Molecular Thermodynamics of Fluid-Phase Equilibria, Prentice Hall PTR (1985).
- [94] Sumpter B. G., Noid D. W., Liang G. L. and Wunderlich B., *Adv. Polym. Sci.* **116**, 29 (1994).
- [95] Noid D. W., Sumpter B. G. and Wunderlich B., *Macromolecules* **24**, 4148 (1991).
- [96] Sumpter B. G., Noid D. W. and Wunderlich B., *Macromolecules* **25**, 7247 (1992).

- [97] Cornell W. D., Cieplak P., Bayly C. I., Gould I. R., Merz K. M. J., Ferguson D. M., Spellmeyer D. C., Fox T., Caldwell J. W. and Kollman P. A., *J. Am. Chem. Soc.* **117**, 5179 (1995).
- [98] Sun H., *J. Phys. Chem. B* **102**, 7338 (1998).
- [99] Jorgensen W. L., Maxwell D. S. and Tirado-Rives J., *J. Am. Chem. Soc.* **118**, 11225 (1996).
- [100] MacKerell Jr. A. D., Bashford D., Bellott M., Dunbrack Jr. R. L., Evanseck J., Field M. J., Fischer S., Gao J. Guo, H., Ha S., Joseph D., Kuchnir L., Kuczera K., Lau F. T. K., Mattos C., Michnick S., Ngo T., Nguyen D. T., Prodhom B., Reiher III W. E., Roux B., Schlenkrich M., Smith J., Stote R., Straub J., Watanabe M., Wiorkiewicz-Kuczera J., Yin D., and Karplus M., *J. Phys. Chem. B* **102**, 3586 (1998).
- [101] Mayo S. L., Olafson B. D., Goddard III W. A., *J. Phys. Chem.* **94**, 8897 (1990).
- [102] Rappé A. K., Casewitt C. J., Colwell K. S., Goddard III W. A. and Skiff W. M., *J. Am. Chem. Soc.* **114**, 10024 (1992).
- [103] Johnson R. A., *J. Phys. F: Metal Phys.* **3**, 295 (1973).
- [104] Ercolessi F., Parrinello M. and Tosatti E., *Phil. Mag. A* **58**, 213 (1988).
- [105] Maruyama S., *Molecular Dynamics Methods in Microscale Heat Transfer. Heat Transfer and Fluid Flow in Microchannel*, Gian Piero Celata, 161 (2004).
- [106] Daw M. S. and Baskes M. I., *Phys. Rev. Lett.* **50**, 1285 (1983).
- [107] Daw M. S. and Baskes M. I., *Phys. Rev. B* **29**(12), 6443 (1984).
- [108] Foiles S. M., Baskes M. I. and Daw M. S., *Phys. Rev. B* **33**, 7983 (1986).
- [109] Baskes M. I., *Phys. Rev. Lett.* **59**, 2666 (1987).
- [110] Daw M. S., *Phys. Rev. B* **39**, 7441 (1989).
- [111] Baskes M. I., *Phys. Rev. Lett.* **83**(13), 2592 (1999).
- [112] Stott M. J. and Zaremba E., *Phys. Rev. B* **22**, 1564 (1980).
- [113] Nørskov J. K. and Lang N. D., *Phys. Rev. B* **21**, 2131(1980).
- [114] Clementi E. and Roetti C., *At. Data Nucl. Data Tables* **14**, 177 (1974).
- [115] McLean A. D. and McLean R. S., *At. Data Nucl. Data Tables* **26**, 197 (1981).
- [116] Rose J. H., Smith J. R. and Ferrante J., *Phys. Rev. B* **28**(4), 1835 (1983).
- [117] Davis G. T., Eby R. K. and Colson J. P., *J. Appl. Phys.* **41**, 4316(1970).
- [118] Alberola N., Cavaille J. Y. and Perez. J., *Eur. Polym. J.* **28**(8), 935 (1992).
- [119] Gao G., *Large Scale Molecular Simulations with Application to Polymers and Nano-scale Materials*, Ph.D. Thesis, California Institute of Technology (1998).

- [120] Thompson S. M., Gubbins K. E., Walton J. P., Chantry R. A. and Rowlinson J. S., *J. Chem. Phys.* **81**(1), 530 (1984).
- [121] Neijmeijer M. J. P., Bakker A. F., Bruin C. and Sikkenk J. H., *J. Chem. Phys.* **89**(6), 3789 (1988).
- [122] Nijmeijer M. J. P., Bruin C., van Woerkom A. B. and Bakker A. F., *J. Chem. Phys.* **96**(1), 565 (1992).
- [123] Holcomb C. D., Clancy P. and Zollweg J. A., *Mol. Phys.* **78**(2), 437 (1993).
- [124] Blokhuis E. M., Bedeaux D., Holcomb C. D. and Zollweg J. A., *Mol. Phys.* **85**(3), 665 (1995).
- [125] Mecke M., Winkelmann, J. and Fischer J., *J. Chem. Phys.* **107**(21), 9264 (1997).
- [126] Trokhymchuk A. and Alexandre J., *J. Chem. Phys.* **111**(18), 8510 (1999).
- [127] Irving J. H. and Kirkwood J. G., *J. Chem. Phys.* **18**, 817 (1950).
- [128] Todd B., Evans D. J. and Daivis P. J., *Phys. Rev. E* **52**, 1627 (1995).
- [129] Harasima A., *Adv. Chem. Phys.* **1**, 203 (1958).
- [130] Kirkwood J. G. and Buff F. P., *J. Chem. Phys.* **17**(3), 338 (1949).
- [131] IUPAC, International Thermodynamic Tables of the Fluid State - Argon, Butterworths (1972).
- [132] Zhu S. B. and Philpott M. R., *J. Chem. Phys.* **100**(9), 6961 (1994).
- [133] Maruyama S., Matsumoto S. and Ogita A., *Thermal Sci. Eng.* **2**(1), 77 (1994).
- [134] Maruyama S., Kurashige T., Matsumoto S., Yamaguchi Y. and Kimura T., *Microscale Thermophys. Eng.* **2**, 49 (1998).
- [135] Rumminger M. D., Reinelt D., Babushok V. and Linteris G. T., *Combust. Flame* **116**, 207 (1999).
- [136] Stillinger F. H., *J. Chem. Phys.* **38**, 1486 (1963).
- [137] Petsche I. B. and Debenedetti P. G., *J. Chem. Phys.* **91**(11), 7075 (1989).
- [138] Yasuoka K. and Matsumoto M., *J. Chem. Phys.* **109**(19), 8451 (1998).
- [139] Yasuoka K. and Matsumoto M., *J. Chem. Phys.* **109**(19), 8463 (1998).
- [140] <http://www.pas.rochester.edu/~wangyt/algorithms/cone/>.
- [141] Foiles S. M., *Phys. Rev. B* **32**(6), 3409 (1985).
- [142] Agrawal P. M., Rice B. M. and Thompson D. L., *Surf. Sci.* **515**, 21 (2002).
- [143] Stoddard S. D., *J. Comput. Phys.* **27**, 291 (1978).

# Acknowledgments

It is tempting to establish an analogy between the stages of the elaboration of thesis and a nucleation phenomenon. Like little clusters in the first stages of growth, new ideas are welcome, some of them are discarded and others are developed until they reach a critical degree of evolution. Many are the factors which affects the dynamics of an investigation; mostly human interactions, sometimes technical aspects, last but not least an average of stochastic fluctuations usually called factor luck.

This work begins with the thesis proposal of PD. Dr. Kraska. I do not only want to thank him for that but also for his scientific guidance and support in many ways during these four years. His patience and generous help were a driving force to hold on and continue in my latency phases.

No less important was the stimulating interaction with the group of people who worked in my closest neighborhood at the Institute of Physical Chemistry of the University of Cologne: Prof. Dr. Deiters, Dr. Norbert Lümmer, Dipl. Björn Fischer, Frank Römer, Dr. Leonid Yelash and Dr. Sergio Quiñones. Their works were a source of inspiration in the course of my study. I particularly would like to thank Norbert for his valuable help in the implementation of the simulations of metals, Björn and Frank for their interesting questions and remarks in relation to the simulation methods.

Without the computation resources facilitated by the RRZK Computation Center of the University of Cologne long wait time periods would be necessary to accomplish this investigation.

Studying in Germany would have not been possible for me without the financing and facilities given by DAAD. My tutor there, Frau Hartmann, was always available to attend my preoccupations.

My thanks are also extended to the Wilhelm-und-Else-Heraeus-Stiftung to allow my participation in the Ferienkurs für Physik in TU Chemnitz (2004) and in the Annual Conference of the Deutsche Physikalische Gessellschaft in Dresden (2005).

I specially would like to thank the faith and support of persons who followed the course of this story from far away - my dear family Roberto, Patricia, Carolina and Paloma and my ex-tutor and friend Dr. Pedro Toledo. And here in Cologne my good Dragon Dijana.



# Erklärung

Ich versichere, dass ich die von mir vorgelegte Dissertation selbständig angefertigt, die benutzten Quellen und Hilfsmittel vollständig angegeben und die Stellen der Arbeit einschließlich Tabellen, Karten und Abbildungen, die anderen Werken im Wortlaut oder dem Sinn nach entnommen sind, in jedem Einzelfall als Entlehnung kenntlich gemacht habe; dass diese Dissertation noch keiner anderen Fakultät oder Universität zur Prüfung vorgelegen hat; dass sie - abgesehen von unten angegebenen Teil-publicationen – noch nicht veröffentlicht worden ist sowie, dass ich eine solche Veröffentlichung vor Abschluss des Promotionsverfahrens nicht vornehmen werde. Die Bestimmungen dieser Promotionsordnung sind mir bekannt. Die von mir vorgelegte Dissertation ist von Priv.-Doz. Dr. Thomas Kraska betreut worden.

Köln im Oktober 2006, Roberto Rozas

# Curriculum Vitae

## Lebenslauf

Name : Rozas  
 Vorname : Roberto  
 Geschlecht : Männlich  
 Geburtsdatum: 17 . 02. 1975  
 Geburtsort : Concepción, Chile  
 Familienstand : Ledig  
 Anschrift : Institut für Physikalische Chemie  
 Luxemburger Str. 116, D-50939 Köln  
 e-mail : rrozaz955@hotmail.com

## Ausbildung

Promotion : von 04/2003 bis 12/2006  
 Institut für Physikalische Chemie  
 Universität zu Köln, Deutschland  
 Betreuer : PD. Dr. Thomas Kraska  
 Dissertation : “Molekulardynamische Untersuchungen  
 heterogener Keimbildung”

M. Sc. : von 04/2000 bis 12/2002  
 Institut für Chemie-Ingenieurwesen  
 Universität von Concepción, Chile  
 Betreuer : Prof. Dr. Pedro G. Toledo  
 Magisterarbeit: “Permeabilität poröser Mittel:  
 numerische Experimente und Theorie“

Diplom : von 1993 bis 2000  
 Institut für Chemie-Ingenieurwesen  
 Universität von Concepción, Chile  
 Betreuer : Prof. Dr. Pedro G. Toledo  
 Diplomarbeit : “Bestimmung der Transporteigenschaften bei porösen  
 Materialien von variabler Porosität mittels Mean-Field-  
 Theorie“

Schulbesuch : von 1980 bis 1992  
 Instituto de Humanidades A.S.S.